

ACTUAL PROBLEMS OF RADIOPHYSICS

Proceedings of the VI International Conference “APR-2015”
October, 5–10, 2015, Tomsk, Russia

Edited by S.A. Maksimenko



Published in 2016 by Red Square Scientific
20-22 Wenlock Road, London, N1 7GU, UK
www.redsquaresci.com

Copyright © The Authors, 2016
This is an open access publication of the Creative Commons Attribution-NonCommercial-NoDerivs License, which permits use and distribution in any medium, provided the original work is properly cited, the use is non commercial and no modifications or adaptations are made.

A CIP record for this book is available from the British Library.
ISBN 978-0-9928299-4-0

First edition
1 2 3 4 5 6 7 8 9 10

Printed in Russia

Table of Contents

Foreword	5
LOW FREQUENCY TRANSDUCER TO MEASURE CONDUCTIVITY OF AQUEOUS SOLUTIONS <i>R.V. Baldov, V.A. Zhuravlev, V.I. Suslyayev, A.S. Tretyakov</i>	6
CALCULATION OF PARAMETERS OF DETECTORS OF TERAHERTZ RANGE BASED ON THE SYSTEM IMMERSION LENS-PLANAR ANTENNA-SEMICONDUCTOR SENSING UNIT <i>A.V. Barko, A.V. Voitsekhovskii, A.G. Levashkin, A.P. Kokhanenko</i>	9
ANALYTICAL MODELING OF THE LASER GUIDE STAR APPLICATIONS <i>L.A. Bolbasova, V.P. Lukin</i>	12
EFFECT OF ULTRASONIC TREATMENT ON ELECTROPHYSICAL PROPERTIES OF CARBON NANOTUBES – LAQUER COMPOSITES AT MICROWAVE FREQUENCIES <i>O.A. Dotsenko, A.O. Kachusova</i>	16
THE THEORETICAL RESEARCH OF IMPATT DIODE, WHICH IS IN THE MODE OF DETECTING SHF-AMPLITUDE-MODULATED OPTICAL OSCILLATIONS <i>A.V. Gevorkyan</i>	20
MODELING OF ELECTRIC FIELD OF ATMOSPHERE DURING WINTER THUNDERSTORMS <i>A.A. Kobranova, V.N. Morozov, P.M. Nagorskiy, K.N. Pustovalov, O.V. Kharapudchenko</i>	25
HIDING CAPACITY OF ABSORBING MEDIUM <i>Yu.L. Lomukhin, B.V. Basanov, E.B. Atutov</i>	29
INVESTIGATIONS OF SOME NEW FOCUSING PROPERTIES OF CUBOID-AIDED PHOTONIC JET <i>I.V. Minin, O.V. Minin, V.I. Suslyayev, I.O. Dorofeev, V.P. Yakubov, V. Pacheco-Pena, M. Beruete</i>	32

ACTUAL PROBLEMS OF RADIOPHYSICS

Proceedings of the VI International Conference "APR-2015"

SPECIAL FEATURES OF ELECTROMAGNETIC WAVE PROPAGATION IN A THREE-LAYER CYLINDRIC WAVEGUIDE WITH RIGHT- AND LEFT-HANDED MEDIA <i>V.A. Meshcheryakov</i>	36
ELECTROMAGNETIC PROPERTIES OF CARBON NANOTUBES COMPOSITES: PVA vs SAC <i>A.G. Paddubskaya, A. Plyushch, A.V. Kukhta, P.P. Kuzhir, S.A. Maksimenko, T. Ivanova, R. Merijs-Meri, J. Bitenieks, J. Zicans, V.I. Suslyaev, M.A. Pletnev</i>	40
INVESTIGATION OF Si/Ge p-i-n STRUCTURES WITH Ge QUANTUM DOTS BY ADMITTANCE SPECTROSCOPY METHODS <i>A.A. Pishchagin, K.A. Lozovoy, V.Yu. Serokhvostov, A.P. Kokhanenko, A.V. Voitsekhovskii, A.I. Nikiforov</i>	45
INVESTIGATION OF MICROWAVE ULTRAWIDEBAND CHAOTIC GENERATION IN ACTIVE DETERMINISTIC SELF-OSCILLATE SYSTEM EXCITED BY IMPATT DIODE <i>I.V. Semernik, A.V. Demyanenko</i>	49
RESEARCH OF ELECTROMAGNETIC PROPERTIES OF FERROFLUID BASED ON SEMI-SYNTHETIC OIL IN THE TERAHERTZ FREQUENCY RANGE <i>V.I. Suslyaev, A.A. Pavlova, A.V. Badin</i>	54
METEOROLOGICAL COMPLEX BASED ON LIDAR AND RADAR <i>G.G. Shchukin, A.S. Boreysho, V.Yu. Zhukov, M.Yu. Ilyin, M.A. Konjaev</i>	58

ACTUAL PROBLEMS OF RADIOPHYSICS

Proceedings of the VI International Conference "APR-2015"

FOREWORD

Radiophysics is a quite young and fast developing science. It studies the physical phenomena that are relevant to electromagnetic waves. Radiophysics is used in various fields of science and technology. This book is a collection of reports on the application of electromagnetic waves in the following fields: medicine, biology, hydrology, and etc.

Note, the study of electromagnetic wave propagation in areas with difficult terrain is a difficult task. Because, the electromagnetic waves in the forest and the city are propagated otherwise than in free space.

It is known that the properties of substances are limitless. Substances can have the properties of conductors and insulators, diamagnetic and paramagnetic. They can be homogeneous and non-homogeneous, liquid, solid and gaseous, etc.

All of these are an interesting to study by methods of radiophysics.

International Scientific and Practical Conference "Actual Problems of Radiophysics" is held annually at the Tomsk State University in 1996. On average, time in two years at the conference is considered more than 400 reports of scientists, professionals, postgraduate students and undergraduate students.

Professor S.A. Maksimenko

LOW FREQUENCY TRANSDUCER TO MEASURE CONDUCTIVITY OF AQUEOUS SOLUTIONS

R.V. Baldov, V.A. Zhuravlev, V.I. Suslyayev, A.S. Tretyakov

National Research Tomsk State University, Tomsk, Russia

Correspondence to:

R. V. Baldov
 Post Address: Tomsk State University, 36 Lenin Ave., Tomsk, Russia, 634050
 E-mail: r.baldov@mail.ru

Citation:

Baldov, R. V., Zhuravlev, V. A., Suslyayev, V. I., and Tretyakov, A. S. (2016). Low frequency transducer to measure conductivity of aqueous solutions. In *Actual problems of radiophysics. Proceedings of the VI International Conference "APR-2015"*, (pp. 6-8). London: Red Square Scientific.

Published: 14 October, 2016

This is an open access article of the Creative Commons Attribution-NonCommercial-NoDerivs License, which permits use and distribution in any medium, provided the original work is properly cited, the use is non commercial and no modifications or adaptations are made.

Abstract. The low-frequency transducers of different design for measuring the conductivity of aqueous solutions are investigated. Oscillation frequency is an output parameter of these sensors. The generator of rectangular pulses on the base of an operational amplifier is an optimal solution for measurements of conductivity in wide range. The sensor was calibrated in the conductivity range from distilled (19 mkS/cm) to sea (70 mS/cm) waters.

Keywords: conductivity measurement, conductivity sensors, electrolyte solutions, multivibrator.

Information about the presence of conductive impurities contained in the water environment required for addressing a range of important practical and fundamental problems. It is required for scientists, ecologists, specialists of Maritime transport, hydrologists, specialists of underwater communications, etc.

Currently there are many devices that measure the conductivity (and salinity) in a wide range of concentrations, but their price is quite high. Also there are problems when you turn these devices in systems of automatic monitoring of natural and artificial water sources. Therefore, the task of developing a simple and reliable conductivity sensor that operates in real time and provides information about conductivity in handy form for the digital processing, is relevant.

There are simple methods of construction of the measuring circuits operating on the AC and DC. They are based on measuring the voltage or current, which requires the using of analog-to-digital converters. This complicates the design of the sensors.

The sensor for measuring the conductivity of aqueous solutions based on the square wave generator on the logical elements was proposed in [1]. Frequency control oscillator circuit includes capacitor C and the resistor R , which is the measuring cell. It contains two platinum electrodes placed in the test solution. The frequency of the generated pulses is inversely proportional to the time constant $\tau = CR$. Consequently, the conductivity of the aqueous solution can be measured by the change in the oscillator frequency, if the sensor calibrate with solutions of known electrical conductivity.

The main advantages of this sensor are: simplicity of design of the

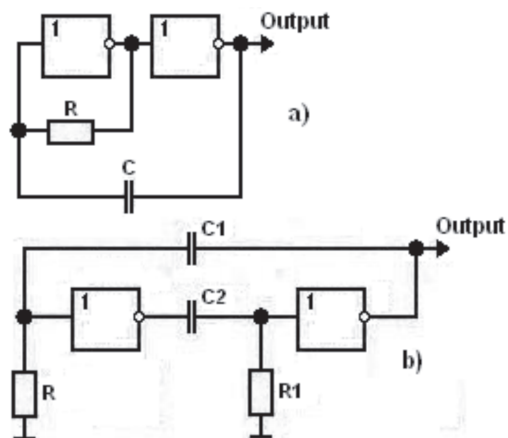


Fig. 1. – The electrical circuit of the single vibrators on logical elements.

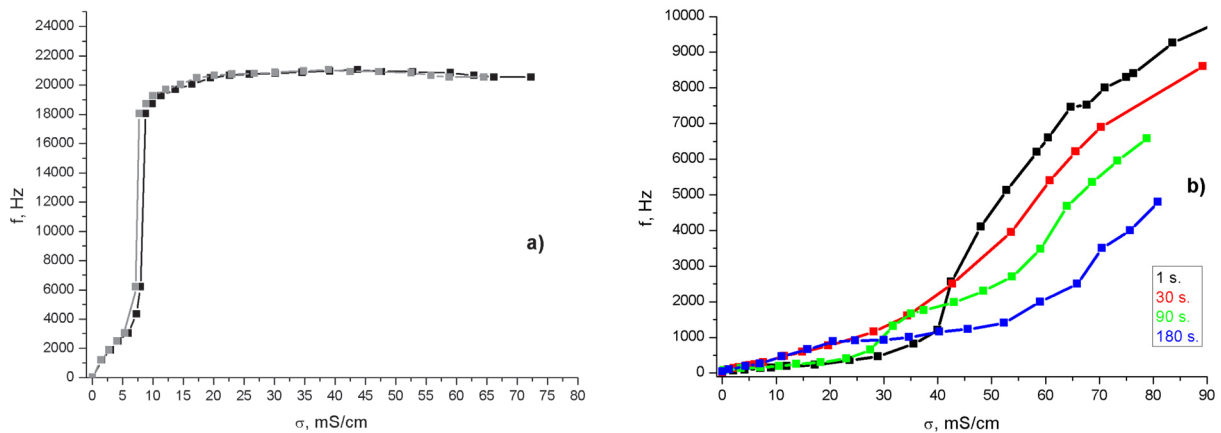


Fig. 2 – Sensor calibration with solutions of KCl:
a) – the sensor on the base of CMOS logic, b) – the sensor on the base of TTL logic.

sensor, high accuracy due to the fact that the measured parameter is the frequency and ease of processing of experimental data, since it is possible to apply the normal computer sound card.

The authors of article [1] claim that their device applicable for measuring the conductivity of aqueous solutions in a wide range, up to sea water. However, according to given in the article calibration curve, the sensor measures the conductivity of solutions only up to ~ 1 mS/cm, while the conductivity of the sea water reaches ~ 70 mS/cm.

This device has been taken as a basis for the construction of our sensor circuit. We investigated different designs of the monostable multivibrator with use of logic elements TTL and CMOS logics [2]. Their typical electrical circuits are shown in Figure 1. Resistor R in the schemes represents a measuring cell with the test solution. The cell consists of two gold-plated electrodes with a diameter of 1.5 mm and a length of 5 mm spaced 7.5 mm apart. Distinction of circuits a) and b) are in a different way of connecting the measuring cell in the circuit.

Sensors calibration was performed on standard KCl solution with a predetermined concentration. The main disadvantages of these constructions are as follows:

- The narrow range of conductivity measurement for the sensor on the base of CMOS logic. As in [1], it does not exceed values about $5 \div 8$ mS/cm. When the resistance of the measuring cell with the solution becomes noticeably less than the internal input or output impedance of chips, the generation frequency stops changing when

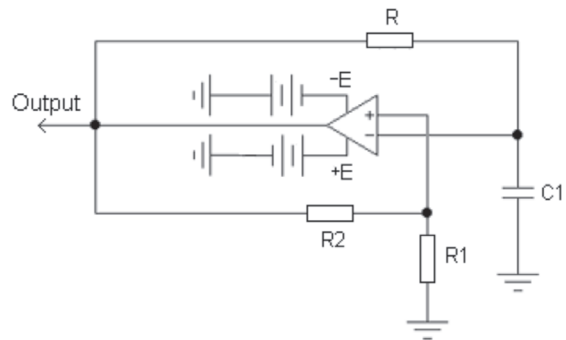


Fig. 3. – The electrical circuit of the multivibrator on the operational amplifier.

changing the conductivity of the solution (Figure 2a). Schemes based on TTL logic operable in a more wide range of conductivity (Figure 2b).

- The more important disadvantage of these schemes is as follows. Unipolar power supply of generator circuit (+5 V) leads to the appearance of DC voltage on the measuring electrodes. Sensor readings become unstable in times of measuring due to near-electrode phenomena, such as the electric double layer, electrolysis and increasing of the investigated solution temperature (Figure 2b). Referring to Figure 2b, an increase in the exposure time of the solution with a predetermined concentration of KCl while measuring from 1 to 180 seconds leads to a significant decrease in the frequency of the generated pulses.

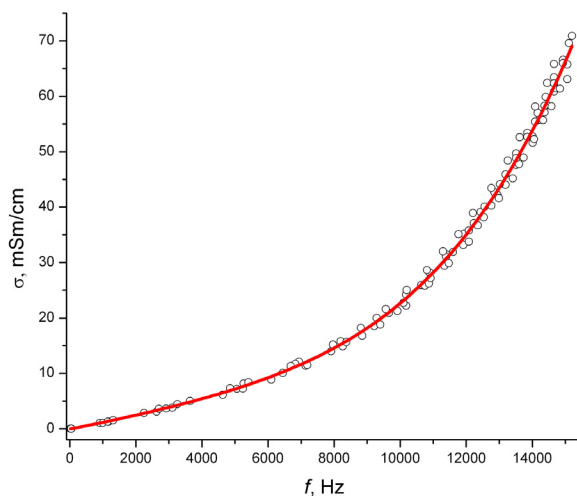


Fig. 4. — The calibration curve of the sensor at the operational amplifier. Line- is a polynomial fit of experimental data.

In order to eliminate these disadvantages, we have chosen the circuit of the multivibrator shown in Figure 3 [3]. We used the operational amplifier of LM358D type. The average value of the voltage and accordingly the current through the measuring cell are zero, since in this circuit bipolar pulses are generated.

The resistor R in the circuit is a measuring cell with solution. The values of resistors R_1 , R_2 of voltage divider are 1.2 kOhm. Experiments have shown that the specified measurement range of conductivity (up to 70 mS/cm) for our measuring cell takes place at the optimum value of the capacitance C , equal to 220 nF.

After selecting circuit elements and their denominations, your sensor was calibrated on KCl solution with a given conductivity at the temperature $\approx 20^\circ\text{C}$. The results of calibration are presented in Figure 4.

Thus, in this article, we investigated different designs of low-frequency sensors on the base of multivibrator to measure the conductivity of aqueous solutions. An output parameter sensor is the frequency of oscillation, proportional to the conductivity of the solutions. We developed a sensor for monitoring aqueous solutions with a wide-range change of the conductivity: from distilled water ($19\ \mu\text{S}/\text{cm}$) up to sea water ($70\ \text{mS}/\text{cm}$).

The work was carried out under section: "Development of methods and hardware-software means for monitoring soluble and insoluble impurities in natural water bodies" in the framework of realization of the Federal target program "Research and development on priority directions of development of scientific-technological complex of Russia for 2014–2020".

References

1. Sahoo, P., Malathi, N., Praveen, K., Ananthanarayanan, R., Arun, A. D., Murali, N., and Swaminathan, P. (2010). High performance conductivity monitoring instrument with pulsating sensor. *Review of Scientific Instruments*, 81, 1-7.
2. *Generatory na KMOP logike*. (2010). Retrieved from <http://radioman-portal.ru/pages/1602/>.
3. Vladimirov, S. N., Deykova, G. M., Zhuravlev, V. A., and Maydanovsky, A. S. (2009). *Nelinejnye i parametricheskie javlenija v radiotehnike: laboratornyj praktikum*. Tomsk, Russia: NTL. 101-102.

CALCULATION OF PARAMETERS OF DETECTORS OF TERAHERTZ RANGE BASED ON THE SYSTEM IMMERSION LENS-PLANAR ANTENNA-SEMICONDUCTOR SENSING UNIT

A.V. Barko, A.V. Voitsekhovskii, A.G. Levashkin, A.P. Kokhanenko

National Research Tomsk State University, Tomsk, Russia

Correspondence to:

A. P. Kokhanenko

Post Address: Tomsk State University, 36 Lenin Ave., Tomsk, Russia, 634050

E-mail: kokh@mail.tsu.ru

Citation:

Barko, A. V., Voitsekhovskii, A. V., Levashkin, A. G., and Kokhanenko, A. P. (2016). Calculation of parameters of detectors of terahertz range based on the system immersion lens-planar antenna-semiconductor sensing unit. In *Actual problems of radio-physics. Proceedings of the VI International Conference "APR-2015"*, (pp. 9-11). London: Red Square Scientific.

Published: 14 October, 2016

This is an open access article of the Creative Commons Attribution-NonCommercial-NoDerivs License, which permits use and distribution in any medium, provided the original work is properly cited, the use is non commercial and no modifications or adaptations are made.

Abstract. In this work results of calculation of parameters of detectors of terahertz range based on mercury-cadmium telluride (MCT) semiconductor material are given. For increasing the connection with emission of detector it is proposed to use the system immersion lens-planar antenna-semiconductor sensing unit. The dependence of sensitivity of detector on frequency for MCT samples with different types of conductivity is considered. Estimations of optimal parameters of system immersion lens-planar antenna-semiconductor sensing unit for detectors of 1 to 5 THz range are conducted.

Keywords: detectors of terahertz range, immersion lens, planar antenna, MCT.

Terahertz radiation is electromagnetic radiation in the frequency range from 0.3 to 10 THz, i.e. from $0.3 \cdot 10^{12}$ to $10 \cdot 10^{12}$ Hz (wavelengths from 1 mm to 30 mm). This frequency range covers a part of the electromagnetic spectrum between the infrared (IR) and microwave bands, so it is often also called the far infrared or the sub-millimeter range.

However, the terahertz range is still studied not enough and there are few solid-state devices that could emit and detect this radiation in a selective way. Such devices could have wide application, for example, for formation of THz images in medicine, as chemical and biological sensors, in broadband communications, radio astronomy, for diagnostics of atmosphere from satellites, etc. [1].

Photodetectors based on solid solutions of telluride-cadmium-mercury (MCT) is widely used to create infrared photodetecting systems. One of the main advantages of this material is the ability to change the band gap energy by changing the composition of MCT from HgTe toward CdTe. At the same time MCT is a perspective material for the manufacture of semiconductor hot electron bolometers (HEB) due to the narrow band gap, high electron mobility μ_n and relatively small electron relaxation time τ_{nE} and lifetime of free electrons τ .

For the characterization of direct detection receiver the noise equivalent power (NEP) is used. NEP is the radiation power, creating at the receiver input signal equal to the noise [2]:

$$NEP = \frac{U_N}{S_V(\Delta f)^{1/2}},$$

where U_N is the noise voltage, S_V is the volt-watt sensitivity of the detector, Δf is the bandwidth of measuring path near the central frequency.

The results of calculations, carried out on the basis of the model applicable to the consideration of HEB detectors based on semiconductors and shown in Figure 1, and comparison of the results with published data are given in table 1.

As shown in the table 1, the MCT detectors can compete with existing uncooled detectors due to the high frequency modulation and a wide range of operating frequencies.

In terahertz range as well as detecting element an important role plays the antenna-substrate-lens system [2, 3]. Figure 2 shows a schematic repre-

ACTUAL PROBLEMS OF RADIOPHYSICS

Proceedings of the VI International Conference "APR-2015"

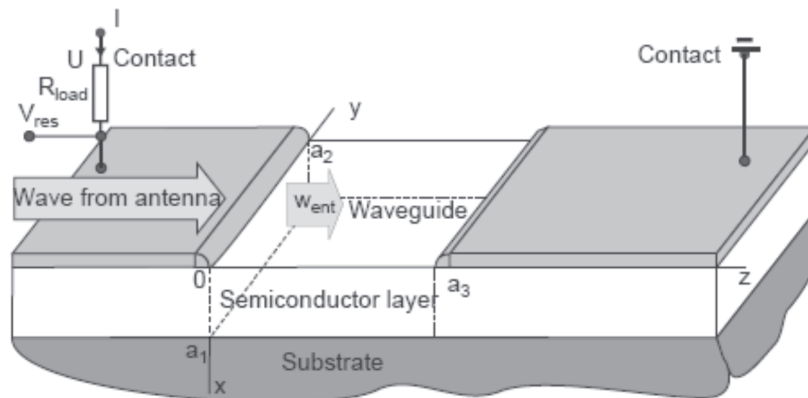


Fig. 1. – Configuration of MCT bolometer.

Table 1. Compare uncooled terahertz detectors.

Types of detectors	Characteristics		
	Modulation frequency (Hz)	Operating frequency (THz)	NEP (W/Hz ^{1/2})
Golay cell [3]	<20	<30	10 ⁻⁹ – 10 ⁻¹⁰
Schottky diodes [3]	< 10 ¹⁰	< 10	>10 ⁻¹⁰
SIS detectors [3]	3·10 ⁴	0,645	≈3·10 ⁻¹⁰
HgCdTe HEB	< 10 ⁸	≈0,5–5	≈5,58·10 ⁻¹⁰

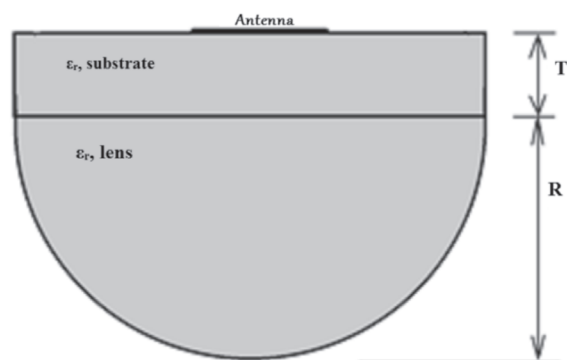


Fig. 2. The antenna-substrate-lens system.

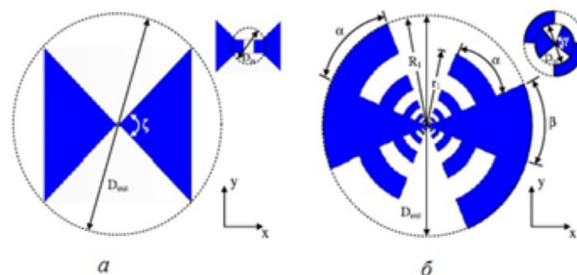


Fig. 3. – The self-complementary antennas:
a – butterfly-shaped; b – log-periodic.

sensation of the antenna on the basis of a hemispherical lens [4].

Lens geometry plays an important role in maximizing directivity, while antenna structure controls the transmission bandwidth. When modeling the projected antenna should not have excitation systems, as their main application is photoconductive anten-

na, which will be initiated by a terahertz source. In this work were carried out calculations of parameters of the butterfly-shaped and the log-periodic antennas with different parameters (Figure 3).

Calculations of the dependency of gain on the frequency for the different sizes of antennas were carried out (Figures 4, 5). Optimization of the geometry

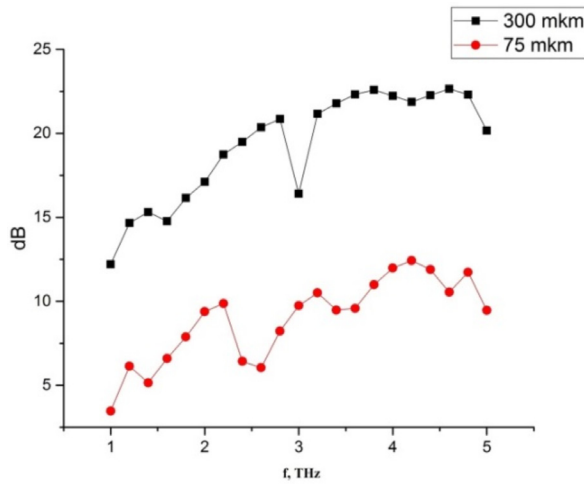


Fig. 5. – Dependence of the gain for log-periodic antenna with a radius of 300 μm and 75 μm.

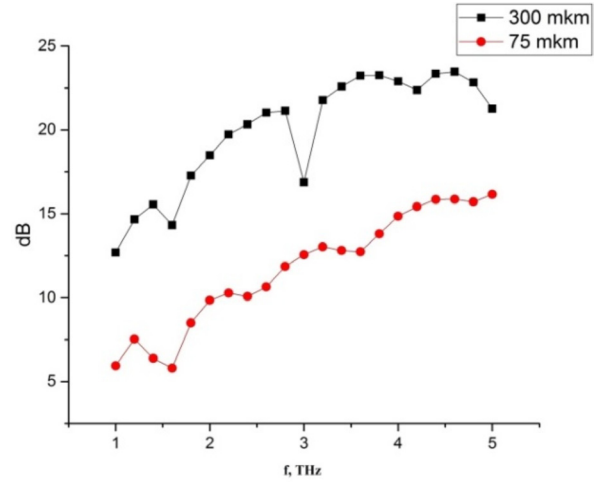


Fig. 6. – Dependence of the gain for butterfly-shaped antenna with a radius of 300 μm and 75 μm.

of a log-periodic antenna was also done. The variant of construction of teeth of log-periodic antenna was offered. Figures 4, 5 shows the results for the butterfly-shaped and log-periodic antennas with different radius ($r = 75 \mu\text{m}$ corresponds to the upper boundary wavelength for $L = \lambda/4$, $r = 300 \mu\text{m}$ corresponds to the upper boundary wavelength for $L = \lambda$). It is seen that the value of amplification depends on the sizes of the antenna and increases with increasing the frequency in the range from 1 THz to 5 THz. No significant differences in the results depending on the type of antenna were observed.

Thus, in this work the possibility of creation of a terahertz detectors based on MCT is considered. Calculations of sensitivity of HEB detectors based on MCT and analysis of immersion lens – planar antenna – semiconductor sensor system are carried out. The possibility and prospects of using such a system for creating sensitive terahertz HEB detectors based on narrow-gap MCT solid solutions is shown.

References

1. Tcarev, M. V. (2011). *Generacia i registracia terahertzovogo lazernogo izlychenia ultrakorotkimi lazernimi impulsami*. Nizhnii Novgorod, Russia: Lobachevsky State University of Nizhni Novgorod. 75 p. [In Russian].
2. Sizov, F., and Rogalski, A. (2010). THz detectors. *Progress in Quantum Electronics*, 34, 278-348.
3. Hohlfield, R. G., Cohen, N. (1999). Self-similarity and the geometric requirements for frequency independence in antenna. *Fractals*, 7, 1, 79-84.
4. Nguyen, T. K. [et al.]. (2012). Numerical study of self-complementary antenna characteristics on substrate lenses at terahertz frequency. *Journal of Infrared, Millimeter, and Terahertz Waves*, 33 (11), 1123-1137.

ANALYTICAL MODELING OF THE LASER GUIDE STAR APPLICATIONS

L.A. Bolbasova^{1,2}, V.P. Lukin²

¹ National Research Tomsk State University, Tomsk, Russia

² V.E. Zuev Institute of Atmospheric Optics of Siberian Branch of Russian Academy of Sciences, Tomsk, Russia

Correspondence to:

L. A. Bolbasova, V. P. Lukin
Post Address: Tomsk State University, 36 Lenin Ave., Tomsk, Russia, 634050
E-mail: l.bolbasova@gmail.com, lukin@iao.ru

Citation:

Bolbasova, L. A., and Lukin, V. P. (2016). Analytical modeling of the laser guide star applications. In *Actual problems of radiophysics. Proceedings of the VI International Conference "APR-2015"*, (pp. 12-15). London: Red Square Scientific.

Published: 14 October, 2016

This is an open access article of the Creative Commons Attribution-NonCommercial-NoDerivs License, which permits use and distribution in any medium, provided the original work is properly cited, the use is non-commercial and no modifications or adaptations are made.

Abstract. This report devoted some theoretical aspects of the Laser Guide Star (LGS) application in adaptive optics (AO) system. The problem of optimal altitude of LGS formation in atmosphere is considered. Analytical formula that characterizes the effect of the LGS application as results of analytical modeling of LGS is obtained. The numerical calculations for different models of the vertical profile of atmospheric turbulence are presented performed.

Keywords: adaptive optics, laser guide star, atmospheric turbulence, analytical modeling.

Introduction

Atmospheric turbulence limits the performance of ground-based astronomical observations. Fluctuations of the refractive index of atmosphere cause wavefront distortions in optical waves propagating from astronomical objects. In results optical image quality formed by ground-based telescopes are degraded. The adaptive optics (AO) corrected wavefront distortions in real time and technique allow reduce or overcome of the image degradation caused by atmospheric turbulence [1]. But AO systems require a wavefront reference source for work. Artificial reference source based on backscattering laser beam in the atmosphere called laser guide star (LGS) or beacon. LGS are formed in sodium layer and based on Rayleigh scattering [2]. Sodium LGS is more preferably because less cone effect in comparison on Rayleigh LGS. However currently there are new interests for Rayleigh Laser Guide star systems related to the progress of commercial lasers and also because the advantages of concepts called turbulence tomography, Multi-Conjugated Adaptive Optics (MCAO), Ground Layer Adaptive Optics (GLAO) have been realized [3, 4]. Equipment is not large telescopes with adaptive optics also uses Rayleigh LGS, for example project Robo-AO [5].

In the present study, the optimal height of Rayleigh LGS formation as a function of the atmospheric turbulent profile, with take account the size of the telescope aperture and wavelength beam are investigated. For it analytical modelings of LGS are performed. The simple analytical formula that characterizes the effect of the LGS application is obtained. The key parameter to the design of adaptive optics systems is vertical dependence of the refractive index structure parameter of the turbulent atmosphere in the form of analytical formula are used for final numerical results.

Methods

The assume that LGS is placed in the plane x , and the input aperture of the telescope constructing the image of the extra atmospheric source is $W(\rho) = \exp(-\rho^2 / 2R^2)$. Replace the effect of the telescope by equivalent lens introducing the phase term $\exp(-ik\rho^2 / 2f)$, where f the equivalent is focus length of the telescope optical system, and $2R$ is the diameter of the telescope input aperture.

We consider the cases of adaptive correction of distortions based on the algorithm of phase conjugation using the data of measurement of the wave

front from LGS. It is usually assumed that the visible size of LGS is so that it is not resolved by the telescope optical system, so it can be considered as a point source. The phase of the wave from such point guide source, with the wave number $k = 2\pi/\lambda$, in the plane of the input aperture of the telescope $x = 0$ can be written as [6]:

$$S_{ref}(0, \vec{\rho}) = kx + \frac{k\rho^2}{2x} + S_{sp}(0, \vec{\rho}; x, 0), \quad (1)$$

where $S_{sp}(0, \vec{\rho}; x, 0)$ is the random phase of spherical wave caused by turbulence at its propagation from the plane x to the point $\vec{\rho}$ lying in the plane of the input aperture of the telescope $x = 0$. It is assumed here that the point source is situated at the optical axis of the telescope.

The relationship for the phase in plane and spherical waves (with the center in the origin of coordinates) in geometric optics approximation [7] given by expression for spherical wave originated from the point $\vec{\rho}_0$, in the plane x :

$$S_{sp}(0, \vec{\rho}) = k \int_0^x d\xi n_1(\xi, \vec{\rho}\xi/x + \vec{\rho}_0(1 - \xi/x)). \quad (2)$$

here and below let us use spectral representation for fluctuations of the refractive index

$$n_1(\xi, \vec{R}) = \iint d^2\vec{\kappa} n(\vec{\kappa}, \xi) \exp(i\vec{\kappa}\vec{R}), \quad (3)$$

then for fluctuations in spherical waves:

$$S_{sp}(0, \vec{\rho}) = k \int_0^x d\xi \iint d^2\vec{\kappa} n(\vec{\kappa}, x - \xi) \exp[i\vec{\kappa}\vec{\rho}\xi/x + i\vec{\kappa}\vec{\rho}_0(1 - \xi/x)]. \quad (4)$$

An astronomical object observed with ground-based telescope is placed at infinity. As the wave propagates downward, we have for the plane wave:

$$S_{pl}(0, \vec{\rho}) = k \int_0^x d\xi \iint d^2\vec{\kappa} n(\vec{\kappa}, x - \xi) \exp(i\vec{\kappa}\vec{\rho} + ik\vec{\alpha}\vec{\rho}), \quad (5)$$

where $\vec{\alpha}$ is the slope angle of the wave front for the star relatively to the telescope axis. If assume the angle $\vec{\alpha} = 0$, then we deal with normally incident plane wave.

When averaging over atmospheric turbulent fluctuations, the use of the assumption that the phase

fluctuations S are Gaussian and have zero mean value, then we obtain

$$\langle \exp(-iS) \rangle = \exp\left(-\frac{\langle S^2 \rangle}{2}\right). \quad (6)$$

If consider formation of an image of natural star in the focal plane ($x = -f$) of the telescope, then we obtain field in the following form:

$$U(-f, \vec{\rho}) = \iint d^2\rho_1 \exp(-\rho_1^2/2R^2) \exp(-\rho_1^2/2R^2) \exp(-\rho_1^2/2f) G_0(0, \vec{\rho}_1; -f, \vec{\rho}) \exp[iS_{pl}(\vec{\rho}_1)], \quad (7)$$

here $G_0(0, \vec{\rho}_1; -f, \vec{\rho})$ is the Green function for free space, $S_{pl}(\vec{\rho}_1)$ are the phase fluctuations of the plane wave at the input aperture of the telescope, which are caused by atmospheric turbulence. Equation (7) has been written assuming that distribution of the field can be represented as the Kirchhoff diffraction integral on conditions that a plane wave with phase distortions $S_{pl}(\vec{\rho}_1)$ in incident on the input aperture. For the majority of astronomical applications, one can take into account only phase fluctuations in the incident wave, because amplitude fluctuations make less contribution in comparison with phase fluctuations.

The isotropic model of the spectral density of fluctuations of the refractive index taking into account the inner scale of turbulence l_0 of the form are used in modeling:

$$\Phi_n(\kappa, \xi) = 0.033 C_n^2(\xi) \kappa^{-11/3} \exp(-\kappa^2 / \kappa_m^2), \quad (8)$$

$$\kappa_m = 5.92 / l_0.$$

Following models of atmospheric turbulence profile are used for numerical results: Greenwood model, Hufnagel Valley 5/7, also modified model for Maui [8].

Results and Discussions

First of all, let us calculate the distribution of the mean intensity in the focal plane of the telescope after the use of LGS. It can be shown that, resulting from phase adaptive correction using the fluctuation part of the spherical reference wave (1) from LGS, the corrected field in the focal plane takes the form [9]:

ACTUAL PROBLEMS OF RADIOPHYSICS

Proceedings of the VI International Conference "APR-2015"

$$U(-f, \bar{\rho}) = \iint d^2 \rho_1 \exp(-\rho_1^2 / 2R^2) G_0(0, \bar{\rho}_1; -f, \bar{\rho}) \times \exp[iS_{pl}(\bar{\rho}_1) - iS_{sp}(x, 0; 0, \bar{\rho}_1) - ik\rho_1^2 / 2f]. \quad (9)$$

Let us note here that the integral in (9) is calculated within the limits of the input aperture of the telescope, i.e. over the circle of the area πR^2 .

In results from correction using LGS, we obtain the following expression for the field intensity formed by astronomical object in focal plane of telescope:

$$\begin{aligned} \langle I(-f, \bar{\rho}) \rangle = & \iint d^2 \rho_1 d^2 \rho_2 \exp(-\rho_1^2 / \\ & / 2R^2) \exp(-\rho_2^2 / 2R^2) G_0(0, \bar{\rho}_1; \\ & -f, \bar{\rho}) G_0^*(0, \bar{\rho}_2; -f, \bar{\rho}) \\ & \times \exp(-ik\rho_1^2 / 2f + ik\rho_2^2 / 2f) \langle \exp\{i[S_{pl}(\bar{\rho}_1) - \\ & - S_{pl}(\bar{\rho}_2)] - i[S_{sp}(x, 0; 0, \bar{\rho}_1) - S_{sp}(x, 0; 0, \bar{\rho}_2)]\} \rangle, \end{aligned} \quad (10)$$

where S_{pl} , S_{sp} phase fluctuation of plane and spherical wave given by (5) and (4) respectively

The term in brackets is:

$$\begin{aligned} \langle \{ \dots \} \rangle = & \exp\left\{-\frac{1}{2} D_s^{pl}(\bar{\rho}_1 - \bar{\rho}_2) - \right. \\ & - \frac{1}{2} D_s^{sp}(\bar{\rho}_1 - \bar{\rho}_2) + \langle S_{pl}(\bar{\rho}_1) S_{sp}(x, 0; 0, \bar{\rho}_1) \rangle \\ & + \langle S_{pl}(\bar{\rho}_2) S_{sp}(x, 0; 0, \bar{\rho}_2) \rangle \\ & \left. - \langle S_{pl}(\bar{\rho}_2) S_{sp}(x, 0; 0, \bar{\rho}_1) \rangle\right\}. \end{aligned} \quad (11)$$

here $D_s^{pl}(\bar{\rho}_1 - \bar{\rho}_2)$, $D_s^{sp}(\bar{\rho}_1 - \bar{\rho}_2)$ are the structural function for plane and spherical waves, respectively.

Finally we obtain the following relationship for distribution of the mean intensity in the focal plane of the telescope at traditional algorithm of correction [10]:

$$\begin{aligned} \langle I(-f, \bar{\rho}) \rangle = & \frac{4\pi^2 R^4}{f^2 [1 + 4R^2 / (\tilde{r}_0^{pl})^2]} \exp(-k^2 \rho^2 R^2 / \\ & / [f^2 (1 + 4R^2 / (\tilde{r}_0^{pl})^2)]), \end{aligned} \quad (12)$$

where the radius of coherence of the field at correc-

tion \tilde{r}_0^{pl} with reference spherical wave is introduced in the form:

$$\tilde{r}_0^{pl} = r_0^{pl} \left[\frac{\int_0^x d\xi C_n^2(\xi) (\xi/x)^2}{\int_0^\infty d\xi C_n^2(\xi)} \right]^{-1/2}. \quad (13)$$

where $C_n^2(\xi)$ is the structural parameter of the refractive index of the atmosphere and

$$r_0^{pl} = 1.707 \{k^2 \int_0^\infty d\xi C_n^2(\xi)\}^{-3/5} \quad (14)$$

is the radius of coherence of the plane wave.

If used Strehl ratio that for the telescope corrected using a focused LGS the following analytical formula are obtained:

$$SR = [1 + 4R^2 / (\tilde{r}_0^{pl})^2]^{-1}, \quad (15)$$

where R – radius of telescope aperture.

Thus finally, we obtain that adaptive correction using traditional focused LGS is practically equivalent to increase of the size of the coherent part of the telescope aperture, and this increase is numerically equal to

$$A = \left[\frac{\int_0^x d\xi C_n^2(\xi) (\xi/x)^2}{\int_0^\infty d\xi C_n^2(\xi)} \right]^{-1/2}$$

and can be calculated using the models of the height dependence of the structural parameter of the refractive index of the atmosphere $C_n^2(\xi)$. The numerical increasing of A for different wavelength and various atmospheric turbulence profiles in Table 1 are presented.

In results, values of radius at the correction in the range 2 to 5 meters (Table 1), this means that, in practice, be achieved by different levels of adaptive correction depending on the intensity and distribution of turbulent fluctuations, it does not occur directly depending on the coherence radius plane wave. The parameter A as resulting from application of LGS for Maui turbulence profile model different scale is show in Figure 1.

Table 1

Models of atmospheric turbulence profile	\tilde{r}_0^m , m, $\lambda = 0.3$	\tilde{r}_0^m , m, $\lambda = 0.5$	\tilde{r}_0^m , m, $\lambda = 0.7$
Maui model	0.5048	0.9325	1.3954
HV model 5/7	0.1894	0.3495	0.5233
Greenwood model	0.4221	0.7791	1.1665

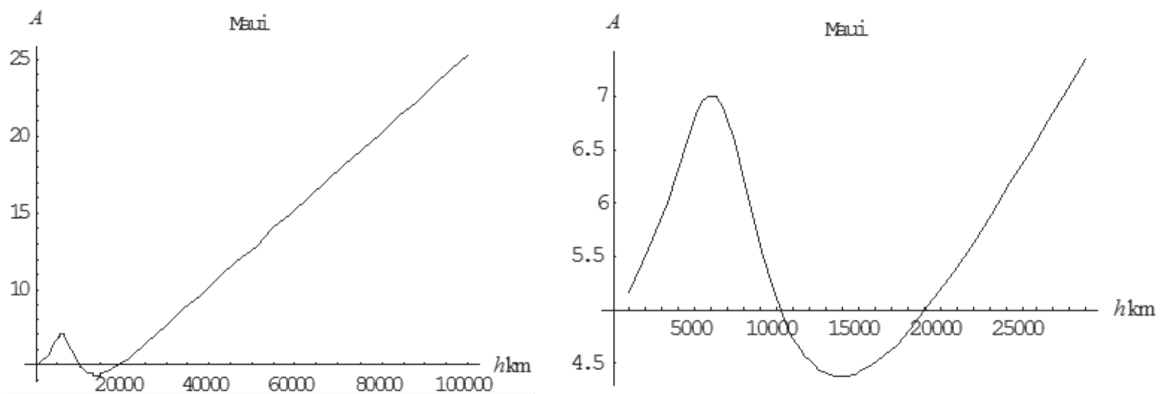


Fig. 1. – Parameter A as function of altitude of LGS formation.

As seen there are optimal heights of Rayleigh LGS formation on depends of intensity and distributions turbulence along the propagation path. For example AO correction with LGS on 10 km and 20 km has same results, but LGS on 7 km became more effectively.

Finally, we note that obtained formulas allow varying the wavelength of the radiation, the size of the aperture of the telescope, the height of the formation of the reference source for the conditions of the problem to determine the optimal parameters and potential.

Acknowledgement

This work was partially supported by the Program of increasing the international competitiveness of the Tomsk State University for 2013–2020 years.

References

- Hickson, P. (2014). Atmospheric and adaptive optics. *Astron. Astrophys. Rev.*, 22 (1).
- Davies, R., and Kasper, M. (2012). Adaptive Optics for Astronomy. *Annual Review of Astronomy and Astrophysics*, 50 (1), 305-351.
- Tatulli, E., and Ramaprakash, A. N. (2013). *Laser Tomography Adaptive Optics (LTAO): A performance study*.
- Basden, A. G., Chemla, F., Dipper, N., Gendron, E., Henry, D., Morris, T., Rousset, G., and Vidal, F. (2014). Real-time correlation reference update for astronomical adaptive optics. *Mon. Not. R. Astron. Soc.*, 439 (1), 968-976.
- Baranec C., Riddle R., Ramaprakash A., Law N., Tendulkar S., Kulkarni S., Dekany R., Bui K., Davis J., Zolkower, J., Fucik, J., Burse, M., Das, H., Chordia, P., Kasliwal, M., Ofek, E., Morton, T., and Johnson, J. (2011). Robo-AO: An Autonomous Laser Adaptive Optics and Science System. *Imaging Appl. Opt.*, AWA2.
- Lukin, V. P. (2014). Adaptive optics in the formation of optical beams and images. *Uspekhi Fiz. Nauk*.
- Lukin, V. P. (2013). Adaptive system for the formation of laser beams in the atmosphere by use of incoherent images as reference sources. *Atmos. Ocean. Opt.*, 26 (4), 345-351.
- Parenti, R. R., and Sasiela, R. J. (1994). Laser-guide-star systems for astronomical applications. *J. Opt. Soc. Am. A*, 11 (1), 288.
- Bolbasova, L. A., and Lukin, V. P. (2010). Possibilities of LGS application. In. *Remote Sensing*, 78280I–78280I–10.
- Bolbasova, L. A., and Lukin, V. P. (2010). Investigation of the efficiency of the application of laser guide stars, *Atmos. Ocean. Opt.*, 23 (1), 65-72.

EFFECT OF ULTRASONIC TREATMENT ON ELECTROPHYSICAL PROPERTIES OF CARBON NANOTUBES – LAQUER COMPOSITES AT MICROWAVE FREQUENCIES

O.A. Dotsenko, A.O. Kachusova

National Research Tomsk State University, Tomsk, Russia

Correspondence to:

O. A. Dotsenko
Post Address: Tomsk State University, 36 Lenin Ave., Tomsk, Russia, 634050
E-mail: dot_ol_09@rambler.ru

Citation:

Dotsenko, O. A., and Kachusova, A. O. (2016). Effect of ultrasonic treatment on electrophysical properties of carbon nanotubes – laquer composites at microwave frequencies In. *Actual problems of radiophysics. Proceedings of the VI International Conference "APR-2015"*, (pp. 16-19). London: Red Square Scientific.

Published: 14 October, 2016

Abstract. This paper focuses on the electrophysical properties of multiwalled carbon nanotubes (MWCNTs) – laquer composites at microwave frequencies. A microwave resonant cavity was utilized as a probe. Three groups of MWCNT-laquer composite samples with weight percentages MWCNT range of 0.25%–2% were fabricated and tested. The multiwall carbon nanotubes used in the composite were about 18.4 nm in diameter. The results show that the ultrasonic treatment modifies the dielectric properties of the composite.

Keywords: MWCNT, composites, ultrasonic treatment, permittivity.

Introduction

The unusual properties of multiwalled carbon nanotubes (MWCNTs) present new opportunities for creating new multifunctional composite materials. Less weight, excellent mechanical, thermal, and electronic properties of MWCNTs can be utilized for various applications. Carbon nanotubes draw particular interest for researchers due to the prospects of their application in various fields of engineering, microwave devices are included [1–5].

The application of nanotubes as independent materials is troublesome, because they possess volatility and low bulk density. For this reason, nanotubes are used as filler in the manufacture composite [6–8], which can be used to solve problems of electromagnetic compatibility and radio components. The permittivity depends on the nanotubes concentration in a composite, aspect ratio and the residues of catalytic metals.

Methods of changes of electrophysical properties of composite materials of external influences on their structure are investigated insufficiently. One way to change the internal structure of composite materials is ultrasonic treatment [9–10].

In this paper, microwave properties of multiwall carbon nanotubes composites are investigated. Before polymerization the composites were treatment by ultrasonic.

Main Part

The fillers of composites were multi-walled carbon nanotubes. MWCNTs were obtained by catalytic gas-phase deposition of ethylene in the presence of FeCo catalyst in Institute of Catalysis SB RAS [11]. The average nanotubes diameter is 18.4 nm, purity > 90%. Nanotubes contain remainders of catalyst about 7.0%.

Urethane alkyd lacquer was used for production of experimental samples. In the liquid state its viscosity is known to be small. This allows a filler to be moved easily. For the production of mix for experimental samples 0.25 wt.% of MWCNT was added to 99.75 wt.% of lacquer. The mixture was placed in a glass beaker. The mixture was sonicated by the ultrasonic device “Alena” (Acoustic Processes & Devices lab Biysk Technological Institute, Russia). Probe was inserted into a glass beaker with mixture. The mixture was sonicated for 1, 2, 3, 4 and 5 minutes at 28 kHz frequency at 50 VA power. Mixtures

This is an open access article of the Creative Commons Attribution-NonCommercial-NoDerivs License, which permits use and distribution in any medium, provided the original work is properly cited, the use is non commercial and no modifications or adaptations are made.

were molded into a planar plate, which size is $70 \times 20 \times 0.5$ mm. Process of polymerization was carried out for 48 hours at the room temperature. We had the same situation with another concentration of fillers.

Measuring equipment

The permittivity was measured by cavity method. Agilent's E8363B vector network analyzer was used to measure of electromagnetic response of the rectangular cavity. When the sample is advanced into the cavity, the intensity of the microwave field in the cavity, the frequency shifts, and the width of the resonance at half-power-maximum are changed according to the electrophysical properties of the sample loading into the cavity. The measuring sample was a long and thin rod with sizes $2 \times 2 \times 70$ mm. Complex permittivity were calculated using the approximation of the perturbation method. The condition the volume of the sample V_c is much smaller than the volume of cavity V_s : $V_c \ll V_s$ should implement in the use of perturbation method. The material parameters for sample should satisfy the condition

$$\frac{\omega}{c} \sqrt{|\hat{\epsilon}|} d \leq \frac{\pi}{6}, \quad (1)$$

where $\hat{\epsilon}$ – permittivity, d – diameter of sample, c – speed of light, $\omega = 2\pi f$ – circular frequency, f – frequency point of measurement. Measurements were made at temperature of 24 ± 1 °C. The real parts of complex

permittivity of experimental samples were measured at 3.6 – 13.0 GHz. They are shown on Figures 1, 2 and 3. The measurement error is about 5 percent.

Discussion

Urethane alkyd lacquer has values of the permittivity 4 rel.un. at the frequency range 3–13 GHz [12].

From Figure 1 we can see that adding nanotubes of 0.25 wt.% to the lacquer has decreased values of the permittivity from 8.5 till ~4 rel.un. Ultrasonic irradiation has changed values of permittivity. Results are shown in Table 1.

Permittivity depends on concentration of MWCNT. Decrease of permittivity, when we used ultrasonic irradiation, may be caused by breaking agglomerates and changing it from spherical inclusions into long threads. Thus, concentration of carbon nanotubes wasn't enough for equipartition.

In Figure 2 we can see that adding nanotubes of 0.5 wt.% to the lacquer has also decreased values of the permittivity and approximately equal permittivity of previous sample. Results are shown in Table 2.

But we didn't reach values of the permittivity about 4 rel.un. as alkyd lacquer. We can suppose that

Table 1. Permittivity values of experimental samples with weight percentages MWCNT 0.25%

Sonication times [min]	0	1	2	3	4	5
ϵ [rel.un]	9.2–8.3	6–4.6	4.2–3.3	6.8–5.6	5.2–3.7	6.7–4.6

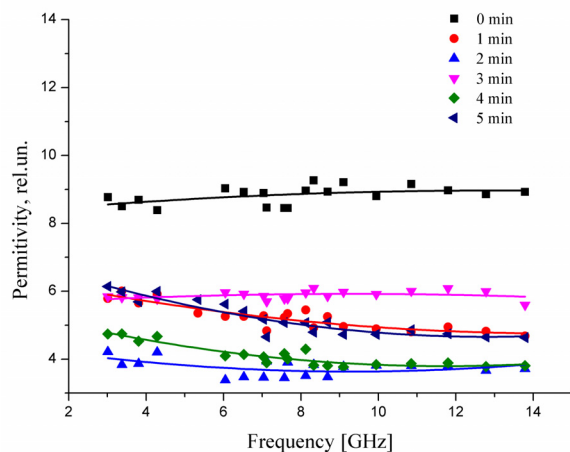


Fig. 1. – Spectra of permittivity of composites with weight percentages MWCNT 0.25%

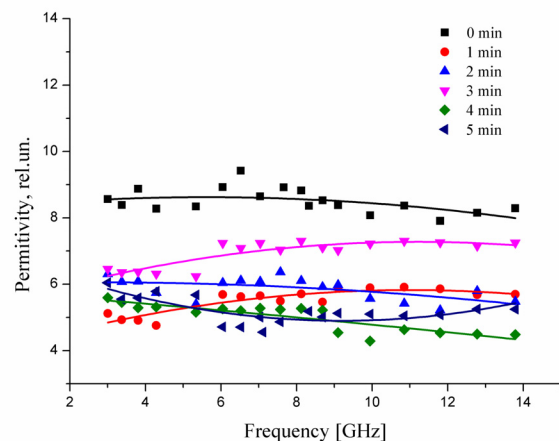


Fig. 2. – Spectra of permittivity of composites with weight percentages MWCNT 0.5%

ACTUAL PROBLEMS OF RADIOPHYSICS

Proceedings of the VI International Conference "APR-2015"

Table 2. Permittivity values of experimental samples with weight percentages MWCNT 0.5%

Sonication times [min]	0	1	2	3	4	5
ϵ [rel.un]	9.5–7.5	6.9–4.6	7.7–5.4	9–6	6–4.5	6–4.6

Table 3. Permittivity values of experimental samples with weight percentages MWCNT 2%

Sonication times [min]	0	1	2	3	4	5
ϵ [rel.un]	9.8 – 12.8	10 – 17.4	13.2 – 20	15 – 17.5	11 – 20	17.3 – 20.0

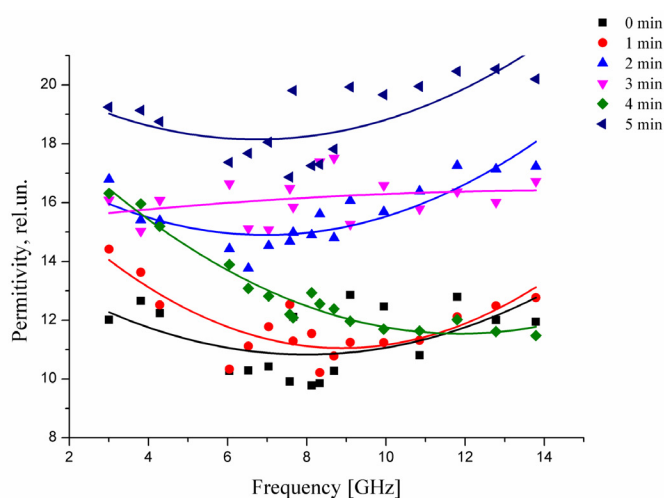


Fig. 3. — Spectra of permittivity of composites with weight percentages MWCNT 2%

this concentration exert influence on permittivity and ultrasonic irradiation broken agglomerates and uniformly distributed long threads throughout the volume of composite.

In Figure 3 we can see that adding nanotubes of 2 wt.% to the lacquer has increased values of the permittivity about 12 rel.un. Results are shown in Table 3.

In other words, increase of permittivity may be caused by high volume concentration of conductive inclusions and effect of ultrasonic irradiation. This is based on the fact that when we use ultrasonic irradiation in the presence of conductive inclusions nanotubes can adjoin with each other and our material have direct electrical admittance. As a consequence, permittivity increased from 10 rel.un. (0 minute of treatment) till 20 rel.un. (5 minute of treatment).

When concentration of nanotubes is about 2 wt%, the condition (1) don't implement, because samples became conductive. In that way, for measuring experimental samples on frequencies 6–13 GHz the

volume of resonator should be bigger than the volume of samples or we can use another method of measurement (e.g. coaxial method).

Conclusion

In this paper we investigated of MWCNT composite materials after ultrasonic treatment. It is shown that adding nanotubes increase permittivity of materials. Composite samples with weight percentages MWCNT of 0.5 % doubled permittivity and 2 wt.% increased by 3 times. To sum up, ultrasonic irradiation has changed values of the permittivity.

Acknowledgment

The authors would like to thank the Center Radiophysical measurements, diagnostics and research parameters of natural and artificial materials of Tomsk State University for the equipment provided. This Research is supported by Tomsk State University Competitiveness Improvement Program.

References

1. Muradyan, V. E., Sokolov, E. A., Babenko, S. D., and Moravsky, A. P. (2010). *Tech Phys.*, 55, 242.
2. Wang, Z., and Zhao, G.-L. (2013). *Open J. of Comp. Mat.*, 3, 17.
3. Chen, X., Akinwande, D., Lee, K.-J., Close, G. F., Yasuda, S., Paul, B. C., Fujita, S., and Kong, J. (2010). *Electr Dev.*, 57, 3137.
4. Plyushch, A., Bychanok, D., Kuzhir, P., Maksimenko, S., Lapko, K., Sokol, A., Macutkevici, J., Banys, J., Micciulla, F., Cataldo, A., and Bellucci, S. (2014). *Phys. Status Solidi A*, 211, 2580.
5. Zhang, H., Zeng, G., Ge, Y., Chen, T., Hu, L. (2009). *J. Appl. Phys.*, 105, 054314.
6. Kuleshov, G. E., Dotsenko, O. A., Ulyanova, O. A., Suslyayev, V. I. (2015). *Int. J. Nanotechnol.*, 12, 200.

ACTUAL PROBLEMS OF RADIOPHYSICS

Proceedings of the VI International Conference "APR-2015"

7. Sedelnikova, O. V., Kanygin, M. A., Korovin, E. Y., Bulusheva, L. G., Suslyayev, V. I., Okotrub, A. V. (2014). *Composites Science and Technology*, 102, 59.
8. Zhao, T., Hou, C., Zhang, H., Zhu, R., She, S., Wang, J., Li, T., Liu, Z., We, B. (2014). *Sci. Rep.*, 4, 5619.
9. Fromyr, T. R., Hansen, F. K., Olsen, T. (2012). *J. of Nanotechnol.*, 1155, 545930.
10. Caneba, G. T., Dutta, C., Agrawal, V. (2010). *J. of Minerals & Materials Characterization & Engineering*, 9, 165.
11. *Mnogoslojnye uglerodnye nanotrubki*. Retrieved from http://www.catalysis.ru/block/index.php?ID=3&SECTION_ID=1513.
12. Dotsenko, O. A., Kachusova, A. O. (2015). *25th International Crimean Conference Microwave & Telecommunication Technology Conference Proceedings*, 1, 703.

THE THEORETICAL RESEARCH OF IMPATT DIODE, WHICH IS IN THE MODE OF DETECTING SHF-AMPLITUDE-MODULATED OPTICAL OSCILLATIONS

A.V. Gevorkyan

Southern Federal University, Taganrog, Russia

Correspondence to:

A. V. Gevorkyan
 Post Address: Southern Federal University, 105 /42, Bolshaya Sadovaya Str., Rostov-on-Don, 344006, Russia
 E-mail:
 A.V.Gevorkyan@yandex.ru

Citation:

Gevorkyan, A. V. (2016). The theoretical research of IMPATT diode, which is in the mode of detecting SHF-amplitude-modulated optical oscillations In. *Actual problems of radiophysics. Proceedings of the VI International Conference "APR-2015"*, (pp. 20-24). London: Red Square Scientific.

Published: 14 October, 2016

Abstract. Investigated active and reactive resistance, which are caused by optical impacts on p-n junction of IMPATT diode and explores their dependence on the parameters of the system. Made comparisons with their own impedance of IMPATT diode and made the conclusion about the possibility of using SHF-amplitude-modulated optical oscillations for control the resultant impedance of IMPATT diode.

Keywords: SHF, IMPATT diode, impedance of IMPATT diode, detector of optical oscillations.

As is well know [1, 2] procurement of SHF-amplitude-modulated optical oscillations on the active area of IMPATT diode accompanied by detecting of these oscillations. And in the impedance of IMPATT diode occurs active and reactive resistances, which are caused by optical impacts on p-n junction of IMPATT diode:

$$\begin{aligned} R_{opt} &= \frac{K}{y^2} \frac{I_{s0}}{I_0} \cos \varphi_s - \frac{K}{y} \frac{MI_{s0}}{A} \cos \varphi, \\ X_{opt} &= -\frac{K}{y^2} \frac{I_{s0}}{I_0} \sin \varphi_s + \frac{K}{y} \frac{MI_{s0}}{A} \sin \varphi, \end{aligned} \quad (1)$$

where:

- A – the amplitude of the detected oscillations;
- I_{s0} – the constant component of the photocurrent, which is caused by optical impact;
- I_0 – supply current of the diode;
- M – the modulation factor of the optical oscillations;

$$y = 1 - \frac{\omega^2}{(2\pi\Omega_J)^2};$$

$$\varphi = \varphi_s - \varphi_1;$$

$$K = \frac{2}{\omega^2 \tau_a C_d} \left[\left(\frac{1 - \cos \theta_d}{\theta_d} \right)^2 + \left(\frac{\sin \theta_d}{\theta_d} + \frac{l_a}{W - l_a} \right)^2 \right]^{1/2};$$

$$\varphi_s = \arctg \left[\frac{\frac{1 - \cos \theta_d}{\theta_d}}{\frac{\sin \theta_d}{\theta_d} + \frac{l_a}{W - l_a}} \right],$$

This is an open access article of the Creative Commons Attribution-NonCommercial-NoDerivs License, which permits use and distribution in any medium, provided the original work is properly cited, the use is non commercial and no modifications or adaptations are made.

where:

- $\Omega_{\mathcal{A}}$ – the avalanche frequency;
- C_d – the capacity of the drift region;
- τ_a – the time-of-flight charge carrier of the equivalent layer multiplying;
- θ_a – the angle of span charge carrier of the drift region;
- l_a – the width of the equivalent layer multiplying;
- W – the width of shut-off layer;
- φ_s – the phase of the optical oscillations;
- φ_l – the phase of the SHF-oscillations;
- ω – the working frequency.

As the novelty of the research of the amplifier on the IMPATT diode as an alternative detector of the SHF-amplitude-modulated optical oscillations consists in his analysis with accounting of the optical impact, therefore it would be appropriate to conduct a research dependence R_{opt} and X_{opt} from parameters and to make the necessary conclusions. It is necessary to consider the impact of the next parameters: M , I_{s0} , I_0 и A , but since A – it is the amplitude of the detected oscillations, which depends from other system parameters, therefore necessary to find her. For this it is necessary to solve the next equation of VI degree [1]:

$$a^6 z_3 + a^4 z_2 + a^2 z_1 = 0,$$

where:

$$z_3 = 1;$$

$$z_2 = \left[2 \left(R_l + \beta_1 + \frac{K I_{s0}}{y^2 I_0} \cos \varphi_s \right) \right] \frac{1}{\left(\frac{3}{4} \beta_3 (M I_{s0})^2 \right)^2};$$

$$z_1 = \left[\left(R_l + \beta_1 + \frac{K I_{s0}}{y^2 I_0} \cos \varphi_s \right)^2 + \left(L \left(\omega - \frac{\omega_0^2}{\omega} + \omega_{oon} \right) - \frac{K I_{s0}}{y^2 I_0} \sin \varphi_s \right)^2 \right] \times \frac{1}{\left(\frac{3}{4} \beta_3 (M I_{s0})^2 \right)^2} - \frac{1}{a^2} \left(\frac{K}{y} \right)^2 \frac{1}{\left(\frac{3}{4} \beta_3 (M I_{s0})^2 \right)^2};$$

R_l – the load resistance;

$$\omega_{oon} = \frac{3}{4L} \frac{\alpha_3}{\omega^3} A^2,$$

α_3 , β_1 , β_3 – the coefficients, which depend on the choice of the working point on the volt-ampere characteristic of diode;

$$\omega_0^2 = \frac{1}{LC}, \quad a = \frac{A}{M I_{s0}}.$$

For begin make changes $\alpha^2 = x$.

Now have:

$$x^3 z_3 + x^2 z_2 + x z_1 = 0. \quad (2)$$

For solve the equation use the Cardano formula

$$y^3 + py + q = 0.$$

Any cubic equation of the general form $x^3 z_3 + x^2 z_2 + x z_1 + z_0 = 0$ can be cast to the canonical form (2) with the coefficients p and q :

$$p = -\frac{z_2^2}{3z_3^2} + \frac{z_1}{z_3};$$

$$q = -\frac{2z_2^3}{27z_3^3} - \frac{z_2 z_1}{3z_3} + \frac{z_0}{z_3},$$

with help a suitable change of variables of the form $x = y - \alpha$.

Consider that $z_3 = 1$:

$$p = -\frac{z_2^2}{3} + z_1, \quad q = 2 \left(\frac{z_2}{3} \right)^3 - \frac{z_2 z_1}{3} + z_0.$$

Substituting the last formulas into the cubic equation, we find this replacement:

$$x = y - \frac{z_2}{3}. \quad (3)$$

According to the Cardano formula the roots of cubic equation in canonical form is equal to:

$$y_1 = A + B, \quad y_{2,3} = -\frac{A+B}{2} \pm i \frac{A-B}{2} \sqrt{3},$$

where $A = \sqrt[3]{-\frac{q}{2} + \sqrt{Q}}$;

$$B = \sqrt[3]{-\frac{q}{2} - \sqrt{Q}}; \quad Q = \left(\frac{p}{2} \right)^3 + \left(\frac{q}{2} \right)^2.$$

Of the three roots of the equation a physical meaning have only the first. And it is necessary to substitute in the formula (3). Multiplying $M I_{s0}$ on the square root of the resulting expression have the volt-ampere characteristic of the diode.

Having the amplitude of the detected oscillations A can begin to identify R_{opt} and X_{opt} .

On the Figures 1 and 2 shows dependence R_{opt}

ACTUAL PROBLEMS OF RADIOPHYSICS

Proceedings of the VI International Conference "APR-2015"

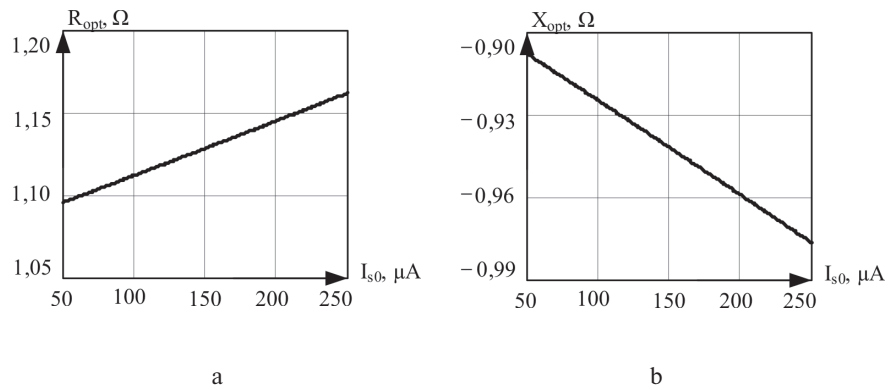


Fig. 1. – Dependence active (a) and reactive (b) resistances, which are caused optical impacts on p-n junction of IMPATT diode, from the constant component of the photocurrent I_{s0} when $R_H = 7 \Omega$.

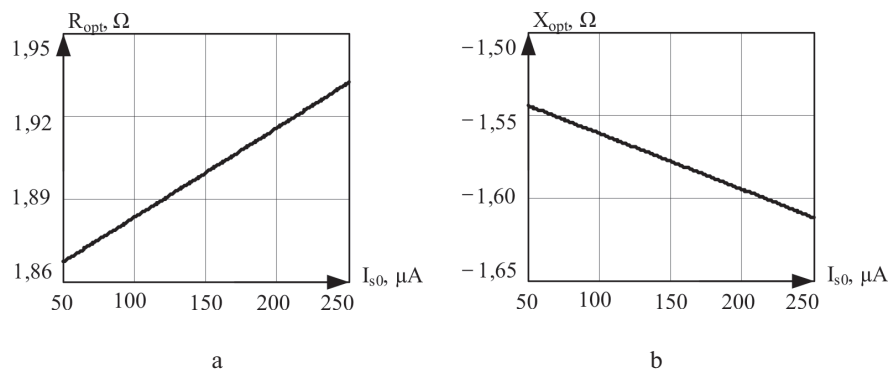


Fig. 2. – Dependence active (a) and reactive (b) resistances, which are caused optical impacts on p-n junction of IMPATT diode, from the constant component of the photocurrent I_{s0} when $R_H = 8 \Omega$.

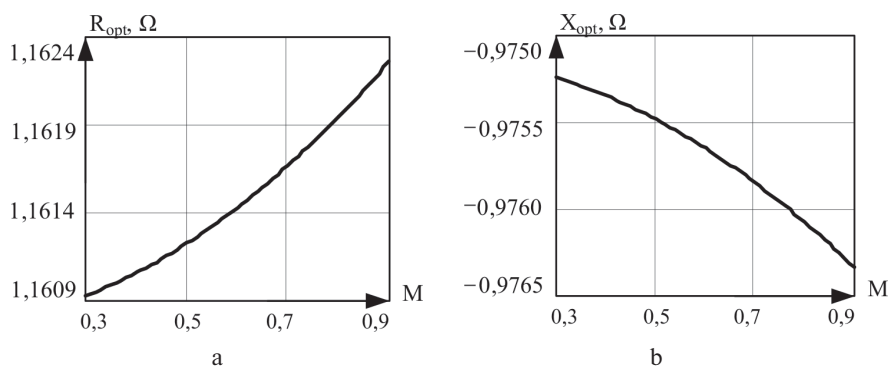


Fig. 3. – Dependence active (a) and reactive (b) resistances, which are caused optical impacts on p-n junction of IMPATT diode, from the modulation factor M .

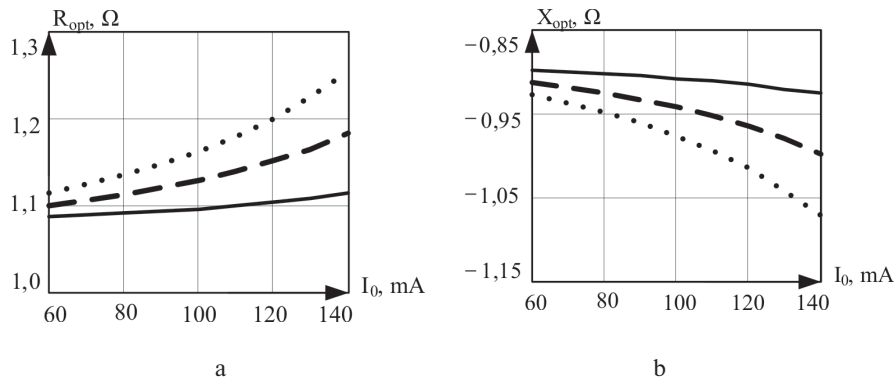


Fig. 4. – Dependence active (a) and reactive (b) resistances, which are caused optical impacts on p-n junction of IMPATT diode, from the supply current I_0 of the diode, when $I_{s0} = 50 \mu\text{A}$ (—); $150 \mu\text{A}$ (---) and $250 \mu\text{A}$ (.....).

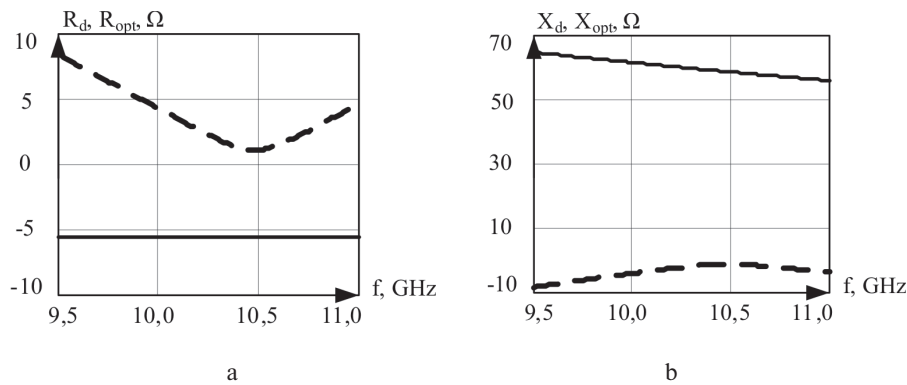


Fig. 5. – Dependence active (a) and reactive (b) resistances, which are caused optical impacts on p-n junction of IMPATT diode, from the working frequency f .

and X_{opt} from the constant component of the photocurrent I_{s0} when the load resistance is 7 and 8 Ω . When making of this graphs used the following values of system parameters: $L = 0,895 \text{ nH}$ and $I_0 = 100 \text{ mA}$. Other parameters are taken for a diode 3A707B.

As can be seen from the graphs, R_{opt} and X_{opt} have linear dependence on constant component of the photocurrent I_{s0} and grow with his increase. X_{opt} have negative values.

Comparing the graphs on Figures 1 and 2 necessary it should be noted that R_{opt} and X_{opt} depend from load resistance and grow with his increase. This is the explanation – R_{opt} and X_{opt} depend from the amplitude of the detected oscillations, which depend from R_H .

On Figures 3 shows dependence R_{opt} and X_{opt} from the modulation factor M , when load resistance $R_H = 7 \Omega$. From the graphs it is visible that they independent from him.

On Figures 4 shows dependence R_{opt} and X_{opt} from the supply current I_0 . From the graphs it is visible that with increase supply current R_{opt} and X_{opt} also increase.

In order to understand what is the contribution active and reactive resistances which are caused by optical impacts on p-n junction of IMPATT diode, need compare them with own impedance of the diode. For this we use the next formulas:

$$R_d = \beta_1 + \frac{3}{4} \beta_3 A^2 \text{ – active resistances of IMPATT diode;}$$

$$X_d = \frac{\alpha_1}{\omega} + \frac{3}{4} \frac{\alpha_3}{\omega^3} A^2 \text{ – reactive resistances of IMPATT diode.}$$

Comparison of R_d (—) and X_d (—) with R_{opt} (---) and X_{opt} (---) shows on Figures 5 ($R_H = 7 \Omega$, $L = 0.895 \text{ nH}$, $M = 0.9$, $I_{s0} = 50 \mu\text{A}$

and $I_0 = 100$ mA). As can be seen from the graphs, R_{opt} and X_{opt} making a significant contribution to the resulting impedance of IMPATT diode, which is in the mode of detecting SHF-amplitude-modulated optical oscillations. Especially in his real part.

Thus, if necessary, SHF-amplitude-modulated optical oscillations is possible not only to detect, but also be used to control of the resulting impedance of IMPATT diode, which characterizes his work.

This work is done as part of the project part of state task No. 8.2461.2014/K of the Ministry of Education and Science of the Russian Federation.

References

1. Gevorkyan, A. V., Dem'yanenko, A. V., Alekseev, Yu. I. (2013). Al'ternativnoe detektirovanie SVCh-amplitudno-modulirovannykh opticheskikh kolebaniy na osnove metodov fotoniki. *Izvestiya vuzov. Fizika*, 56(9/2), 43-45.
2. Alekseev, Yu. I., Dem'yanenko, A. V. (2008). Opredelenie vliyanija opticheskogo signala na impedansnye svoystva lavinno-proletnogo dioda. *Izvestiya vuzov. Yelektronika*, 3, 58-62.
3. Tager, A. S., Val'd-Perlov, V. M. (1968). Lavinno-proljotnye diody i ih primenenie v tehnike SVCh. — Moscow: *Sov. radio*, 480.

MODELING OF ELECTRIC FIELD OF ATMOSPHERE DURING WINTER THUNDERSTORMS

A.A. Kobranova¹, V.N. Morozov², P.M. Nagorskiy³, K.N. Pustovalov³, O.V. Kharapudchenko¹

¹ *National Research Tomsk State University, Tomsk, Russia*

² *The Voeikov Main Geophysical Observatory, Saint-Petersburg, Russia*

³ *Institute of Monitoring of Climatic and Ecological Systems SB RAS, Tomsk, Russia*

Correspondence to:

P. M. Nagorskiy
 Post Address: Tomsk State University, 36 Lenin Ave., Tomsk, Russia, 634050
 E-mail: npm_sta@mail.ru

Citation:

Kobranova, A. A., Morozov, V. N., Nagorskiy, P. M., Pustovalov, K. N., and Kharapudchenko, O. V. (2016). Modeling of electric field of atmosphere during winter thunderstorms. In *Actual problems of radiophysics. Proceedings of the VI International Conference "APR-2015"*, (pp. 25-27). London: Red Square Scientific.

Published: 14 October, 2016

Abstract. Experimental and modeling data on the electrical state of surface atmosphere during the passage of the convective clouds and the winter precipitation are shown and discussed.

Keywords: atmospheric electric field, conductivity, convective clouds.

Introduction

At present there are a lot of approaches and models [1, 3], describing the quasi stationary state of atmospheric electrode layer. However electrization processes and variations of atmospheric electrical quantities in the surface layer under the conditions of the change of a "good" weather (thunderstorms, precipitation, fogs, smokes, etc.) are less studied.

The meteorological conditions associated with significant variations of the characteristics of an electrode layer including the electric field intensity are also less studied. The previous studies of [3] showed some features of electrode layer variations during prestorm and thunderstorms situations. This paper presents the results of experimental and theoretical analysis of the state and variability of electrode layer during intensive perturbation of the electric field intensity of the atmosphere up to several units of kV/m, caused by intensive convective cloudiness.

Experimental results. The analysis of the electric field intensity E and polar conductivities λ_{\pm} data show that the matched variations of these values under significant increasing (more 100 V/m) or decreasing of electric field

intensity is a widespread phenomenon. Basic meteorological, atmospheric electrical values, UV radiation and natural radioactivity [4] have been registered with high temporal resolution in the geophysical observatory of IMCES SB RAS since 2006. The meteorological data of the Tomsk weather station were also used. Examples of such matched variations E и λ_{\pm} during a passage of deep convective clouds are represented in Figure 1.

During snowstorms, snow shower both increasing and decreasing of electric field intensity

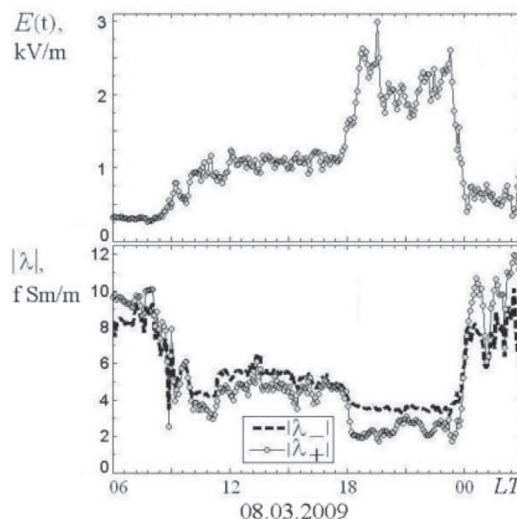


Fig. 1. — The matched oscillations of electric intensity and polar conductivities.

This is an open access article of the Creative Commons Attribution-NonCommercial-NoDerivs License, which permits use and distribution in any medium, provided the original work is properly cited, the use is non-commercial and no modifications or adaptations are made.

ACTUAL PROBLEMS OF RADIOPHYSICS

Proceedings of the VI International Conference "APR-2015"

Table 1. Statistic characteristics of the studied parameters (36 cases)

Characteristics	Mean	Median	Standard deviation
T_{gr}, min	8.1	5.0	8.6
T_{-}, min	7.8	5.0	6.7
T_{+}, min	2.7	1.9	3.1
N_{E-}	1.6	1.5	0.7
N_{E+}	1.8	2.0	0.8
N_{τ}	2.3	2.0	1.3
τ, min	34.0	30.0	17.4

are registered. During intensive convective clouds decreasing the number of light ions of both polarities is observed (Figure 1). A probable cause of λ_{\pm} decrease is the precipitation in the form of rain shower and snow.

Let's consider the temporal characteristics of the electric field variations, including the duration of the positive and negative field perturbations, their number during a lightning storm, etc. In this case the data considered were divided into two classes, the warm season (May – September), cold season (November – March).

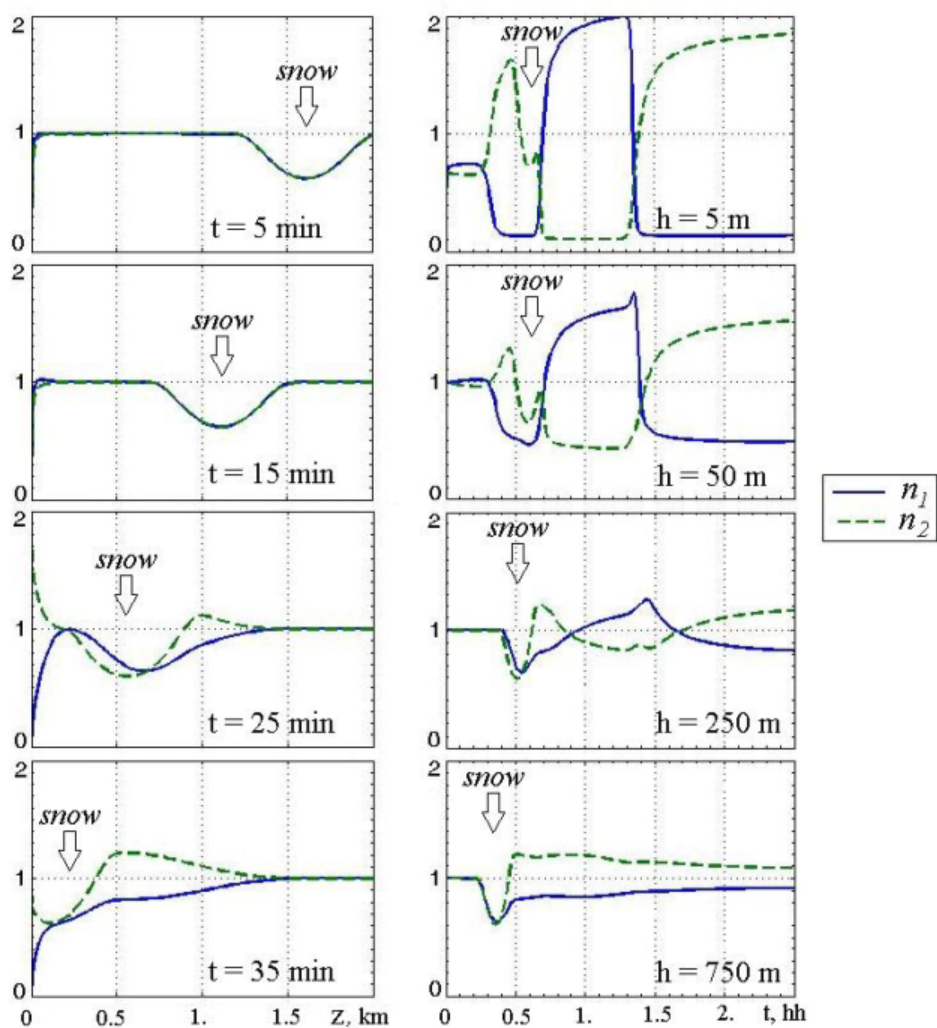


Fig. 2. – Temporal and spatial variations of normalized values of light ion concentrations during snow shower and electric-field variations:

Modeling assumptions: $q = 7 \cdot 10^6 \text{ m}^{-3} \text{c}^{-1}$; $b_1 = 1.36 \cdot 10^{-4} \text{ m}^2/\text{Vc}$, $b_2 = 1.56 \cdot 10^{-4} \text{ m}^2/\text{Vc}$; $\alpha = 1.6 \cdot 10^{-12} \text{ m}^3/\text{c}$; $\eta = 10^{-4} \text{ m}^3/\text{c}$; $D_{\tau} = (Kz + \gamma)/(z + \beta)$; $K = 5$; $\gamma = 5 \cdot 10^{-5} \text{ m}^3/\text{c}$; $\beta = 10 \text{ m}$; $N = N_c [1 - [z - (z_c - V_c t)]^2 / \Delta z^2]^2$; $N_c = 10^3 \text{ m}^{-3}$; $z_c = 1,8 \text{ km}$; $V_c = 50 \text{ m}/\text{MIN}$; $\Delta z = 0,4 \text{ km}$.

April and October were not used in the study because these months are characterized by restructuring type of weather. The main statistic characteristics of electric field variations in the cold season are represented in the Table 1. Here T_{gr} is the period of thunderstorm, T_+ is the period of positive fluctuation of electric intensity E_+ above 0,7 kV/m, T_- is the period of a negative fluctuation of electric E_- less than $-0,35$ kV/m, τ is the period of transition between E_+ and E_- , N_{E_+} и N_{E_-} are the amounts of and negative fluctuation of electric intensity E respectively, N_τ is the amount of transitions between E_+ and E_- .

Numerical modeling

An ion transfer in the atmosphere in the case unstationary electrode effect is carried out by both turbulent flows and electric forces. The basic equations described this process are [2, 3]:

$$\frac{\partial n_{1,2}}{\partial t} \pm b_{1,2} \frac{\partial}{\partial z} (E(t)n_{1,2}) - \frac{\partial}{\partial z} \left(D_T(z) \frac{\partial n_{1,2}}{\partial z} \right) =$$

$$= q(z) - \alpha n_1 n_2 - \eta n_{1,2} N_0,$$

$$\frac{\partial E}{\partial z} = 4\pi e(n_1 + N_1 - n_2 - N_2),$$

where $n_{1,2}$ is the concentration of positive and negative light ions; $b_{1,2}$ is the ion mobility, $q(z) = q_0$ is the rate of ion generation; q_0 is the rate of ion generation at the upper boundary; $a(z)$ is the recombination coefficients of light ions; z is the altitude; D_T is the turbulent diffusion coefficient, η is the coagulation coefficient defining an interaction of light ions and hydrometeors; $N = N_0 + N_{1,2}$ is the total concentration of neutral and charged hydrometeors.

Since precipitation particles are conducting particles, then electrostatic induction forces will contribute to coagulation. $\eta = \epsilon_1 \epsilon_2$ is the coagulation coefficient. It is defined by the product of the collision probability ϵ_1 and the cohesion probability ϵ_2 . A small particles and large particles often gear due to a limit of particle sizes. The value of ϵ_2 at a relative humidity close to 100 % is close to 1.

Figure 2 shows distribution of the concentrations of light ions of both polarities, normalized to the ion concentration on the upper boundary. Spatial distribution of normalized values of light ion concentrations are shown in Figure 2 on the left, temporal change of normalized values of light ion concentrations are shown in Figure 2 on the right. Both observations and the numerical experiment have shown that the electric field increasing leads to the electrical conductivity decreasing and, correspondingly, to decreasing of light ions concentration of respective sign to almost zero. Precipitation is accompanied by matched decreasing of the concentration of light ions of both polarities.

Conclusion

The intensive convective clouds during winter storms affect significantly on temporal and spatial variations of the electrode layer. The main factor of these variations is effects of the electrostatic coagulation and scavenging of light ions by the precipitation. It is confirmed by the results of the statistical analysis of obtained data and the numerical experiment using the system of equations describing a behavior of the unstationary electrode layer.

This work supported by FTP project No. 2014-14-576-0165-037.

References

1. Hoppel, W. A. (1967). *J. of Atmos. Terr. Phys.*, 29, 709-721.
2. Morozov, V. N., Kupovykh, G., and Klovo, A. (2007). In. *Proceedings, XIII Int. Conf. on Atmospheric Electricity*, 154.
3. Nagorskiy, P. M., Morozov, V. N., Smirnov, S. V. [et al.]. (2011). In. *Proceedings, XIV Int. Conf. on Atmospheric Electricity*, 262.
4. Nagorskiy, P. M., Kabanov, M. V., Ippolitov, I. I. [et al.]. (2011). Multivariate Monitoring of Atmospheric Electrical and Meteorological, Optical and Radioactive Parameters of the Atmospheric Boundary Layer. Preliminary Results. In. *Proceedings, XIV Int. Conf. on Atmospheric Electricity*, 77.

HIDING CAPACITY OF ABSORBING MEDIUM

Yu.L. Lomukhin, B.V. Basanov, E.B. Atutov

Institute of Physical Materials Science, Siberian Branch of the Russian Academy of Sciences, Ulan-Ude, Russia

Abstract. The paper presents electrodynamic model RCS of ground in which metallic disk located. The model basis on mechanism of backward-going waves in homogeneous boundary media. The dependences backscattering from the disk radius, depth and angle were performing. Comparison with experiment are given.

Keywords: backscattering, deep of penetration.

Correspondence to:

E. B. Atutov
 Post Address: Institute of Physical Material Science of the Siberian Branch of the RAS, 8, Sakhyanovoy str., Ulan-Ude, 670047, Russia
 E-mail: evgeniy_atutov@mail.ru

Citation:

Lomukhin, Yu. L., Basanov, B. V., and Atutov, E. B. (2016). Hiding capacity of absorbing medium. In *Actual problems of radiophysics. Proceedings of the VI International Conference "APR-2015"*, (pp. 28-31). London: Red Square Scientific.

Published: 14 October, 2016

Electromagnetic waves of the radio band have a remarkable property: they allow to "see" objects at the tight optical wave environments. Currently, wide application of subsurface sensing techniques [1, 2]. The importance of the development of these methods is to use of adequate physical mechanisms of interaction of matter and fields. The paper presents the electrodynamic model of backreflection bordering homogeneous medium, one of which is located the body of a complex permittivity, which differs from perceptivity of a medium. The model is constructed based on the theory of reflection and refraction, which takes into account the excitement in the media backward-going, waves [3].

Figure 1 shows the geometry of the propagating problem. Assume, there exist two media separated by a frontier, the one having $\varepsilon_1 = \varepsilon_1' - j\varepsilon_1''$, $\mu_1 = \mu_0$, and the other having $\varepsilon_2 = \varepsilon_2' - j\varepsilon_2''$, $\mu_2 = \mu_0$. The values of ε_1 and ε_1 are expected to depend on the frequency. In the first medium there is a radar having the narrow antenna directional pattern of $F(\varphi_1)$. In the second medium disk with $\varepsilon_3 = \varepsilon_3' - j\varepsilon_3''$, thickness d_0 and a radius A is situated.

Back reflected field at point P calculated using the vector Green's formula:

$$\vec{E}(P) = \int_{\Sigma} \left(\frac{\partial \vec{E}}{\partial n} G - \vec{E} \frac{\partial G}{\partial n} \right) dS + \int_{\Sigma_T} \left(\frac{\partial \vec{E}}{\partial n} G - \vec{E} \frac{\partial G}{\partial n} \right) dS. \quad (1)$$

Here Σ – the surface of the interface, Σ_T – the disk's surface. The problem is reduced to the choice of the Green's function G and the wave function of the field \vec{E} .

According to [3] back reflected field by can be written as:

$$\vec{E}^{\parallel\perp}(\varphi_1) = \vec{E}_0^{\parallel\perp} e^{-2ik_1R} W^{\parallel\perp}(\varphi_1), \quad (2)$$

$$\text{where } W^{\parallel\perp}(\varphi_1) = \left[1 + \frac{V^{\parallel\perp}(0) e^{2ik_2h_{02}}}{1 - [V^{\parallel\perp}(0)]^2} \right] \left[1 - [V^{\parallel\perp}(\varphi_1)]^2 \right] e^{-2i(\vec{k}_2\vec{h}_2)}, \quad V^{\parallel}(\varphi_1)$$

and $V^{\perp}(\varphi_1)$ are Fresnel coefficients respectively for vertical and horizontal

polarization waves, $k_{1,2} = \frac{\omega}{c} \sqrt{\varepsilon_{1,2}}$, $h_{02} = 1 / \text{Im}(k_2)$ – the depth of penetration of the field into the second medium (the thickness of the skin layer), $\vec{E}_0^{\parallel} = \vec{i} \cos \varphi + \vec{k} \sin \varphi$, $\vec{E}_0^{\perp} = \vec{j}$. \vec{i} , \vec{k} , \vec{j} are unit vectors, $(\vec{k}_2\vec{h}_2) = h_{02}k_2(\sin \varphi_2 + \cos \varphi_2)$.

We need to obtain the expression of back reflected field for a point source.

This is an open access article of the Creative Commons Attribution-NonCommercial-NoDerivs License, which permits use and distribution in any medium, provided the original work is properly cited, the use is non-commercial and no modifications or adaptations are made.

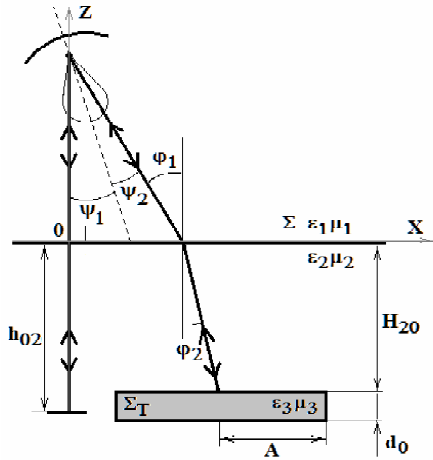


Fig. 1. – The geometry of the problem.

Get it using the expansion of a spherical wave into plane waves [4] taking into account (2).

$$\vec{E}^{\parallel\perp}(P) = -\frac{ik_1}{2} \times$$

$$\times \int_{-\frac{\pi}{2}-i\infty}^{\frac{\pi}{2}+i\infty} H_0^{(2)}(u) e^{-2ik_1 Z \cos \alpha} \vec{E}_0^{\parallel\perp} e^{-i(\vec{k}_1 \vec{R})} W^{\parallel\perp}(\alpha) \sin \alpha d\alpha, \quad (3)$$

After the necessary calculations we have

$$\vec{E}^{\parallel\perp}(P) = \vec{E}_0^{\parallel\perp} \frac{e^{-ik_1 R}}{R} e^{-ik_1 R} W^{\parallel\perp}(\varphi). \quad (4)$$

In accordance with (4) as a function \vec{E} of the first term in (1) accept the expression

$$\vec{E}^{\parallel\perp}(\Sigma) = \vec{E}_0^{\parallel\perp} \frac{e^{-2ik_1 R}}{R} W^{\parallel\perp},$$

$$W^{\parallel\perp} = \left[1 + F(0) \frac{V^{\parallel\perp}(0) e^{-2ik_2 h_{02}}}{1 - [V^{\parallel\perp}(0)]^2} \right] \times$$

$$\times \left[1 - V^{\parallel\perp}(\psi) e^{-2ik_2 h_{02} \sqrt{1 - \frac{\varepsilon_1}{\varepsilon_2} \sin^2 \psi}} \right] F(\psi).$$

The function $F(\varphi)$ takes into account the directional pattern of the radar.

Substituting $\vec{E}^{\parallel\perp}(\Sigma)$ and $G = \frac{e^{-ikR}}{R}$ in (1), we

obtain

$$\vec{E}_1^{\parallel\perp}(\varphi_1) = \vec{E}_0^{\parallel\perp} \frac{e^{-2ik_1 R}}{R^2} W_1^{\parallel\perp},$$

$$W_1^{\parallel\perp} = \left[1 + \frac{F(\varphi_1) V^{\parallel\perp}(0) e^{2ik_2 h_{02}}}{F(0) 1 - [V^{\parallel\perp}(0)]^2} \right] \times$$

$$\times \left[1 - [V^{\parallel\perp}(\varphi_1)]^2 \right] e^{-2ik_2 h_{02} \sqrt{1 - \frac{\varepsilon_1}{\varepsilon_2} \sin^2 \varphi_1}} F(0).$$

For the calculation of the second term in (1) as wave function expression we accept

$$\vec{E}^{\parallel\perp}(\Sigma) = \vec{E}_0^{\parallel\perp} \frac{e^{-ikR}}{R} W_{\Pi}^{\parallel\perp} W_T^{\parallel\perp}, \quad (5)$$

where

$$W_T^{\parallel\perp} = \left[1 + \frac{F(\varphi_1 - \varphi_3) \Phi^{\parallel\perp}(\varphi_2) e^{-2ik_2 h_{02}}}{F(0) 1 - [\Phi^{\parallel\perp}(0)]^2} \right] \times$$

$$\times \left[1 - [\Phi^{\parallel\perp}(\varphi_2)]^2 \right] e^{-2i(\vec{k}_2 \vec{h}_2)},$$

$$W_{\Pi}^{\parallel\perp} = \left[1 + \frac{F(\varphi_1) 1 - V^{\parallel\perp}(0) e^{-2ik_2 h_{02}}}{F(0) 1 - [V^{\parallel\perp}(0)]^2} \right] \times$$

$$\times \left[1 - [V^{\parallel\perp}(\varphi_1)]^2 \right] e^{-2i(\vec{k}_2 \vec{H}_{20})} F(0),$$

$$\Phi^{\parallel\perp}(\varphi_2) = \frac{V_{32}^{\parallel\perp}(\varphi_1) + V_{23}^{\parallel\perp}(\varphi_2) e^{-2ik_3 \sqrt{1 - \frac{\varepsilon_2}{\varepsilon_3} \sin^2 \varphi_2} d_0}}{1 + V_{32}^{\parallel\perp}(\varphi_2) V_{23}^{\parallel\perp}(\varphi_2) e^{-2ik_3 \sqrt{1 - \frac{\varepsilon_2}{\varepsilon_3} \sin^2 \varphi_2} d_0}},$$

$$(\vec{k}_2 \vec{H}_{20}) = H_{20} k_2 (\sin \varphi_2 + \cos \varphi_2).$$

In view of (5) and (3) has a coefficient of back-scattering

$$\sigma^{\parallel\perp}(\varphi_1) = 20 \lg \left\{ W_1^{\parallel\perp} + W_{\Pi}^{\parallel\perp} W_T^{\parallel\perp} \left(1 - e^{-i \frac{k_2 A^2}{H_{20}} \sqrt{1 - \frac{\varepsilon_1}{\varepsilon_2} \sin^2 \varphi_1}} \right) \right\}. \quad (6)$$

On Figure 2 (a, b, c) are given backscattering calculated by (6) depending on backscatter coefficients. The environment here is sand with [5]. The radiation frequency $f = 30\text{GHz}$.

From these calculations we can see that the angular dependence of the observed "splash" in the direction of locating in the disk. Figure 2b is a plot of the backscattering of the radius of the disk. We see resonant dependence, while small compared to the wavelength in the vacuum values of the radius of the disc. Interesting dependence occurs when the disk breaks up (Figure 2c). Firstly, there is the oscillation with increasing depth disk, the oscillation amplitude increases, reaching a maximum then decreases, and at certain depths disappears. Oscillation caused by a retroreflection between of the interface the media and disk. With increasing depth of field attenuates and therefore reduce back reflection from the disc. This effect indicates that the field penetrates through the boundary and extends to a predetermined depth [5].

In [3] found that the backward-going waves excited by secondary sources. Amplitudes of them radiation are proportional to the amplitude of the refracted wave. At a certain depth h_{02} energy of the exciting wave is sufficient only for transfer from the ground state to the first energy level. Oscillators, located deeper than h_{02} not excited. After transference of the excited secondary source back to the ground state energy h_{ω} is emitted. Radiated electromagnetic field acts on the charges of the oscillator, which re-emit part of the energy. The remainder of energy goes to the change in the kinetic energy of the oscillator. The energy emitted from the medium in accordance with Planck's formula can be expressed as:

$$\langle E \rangle = \frac{h\omega}{e^{kT} - 1}. \quad (7)$$

There h – Planck's constant, k – the Boltzmann constant, T – temperature. Let the interaction of the radiation and the medium is that $h\omega = \alpha kT$, $\alpha \ll 1$.

Then $\langle E \rangle = h\omega e^{-\frac{1}{\alpha}}$. Energy emitted from the medi-

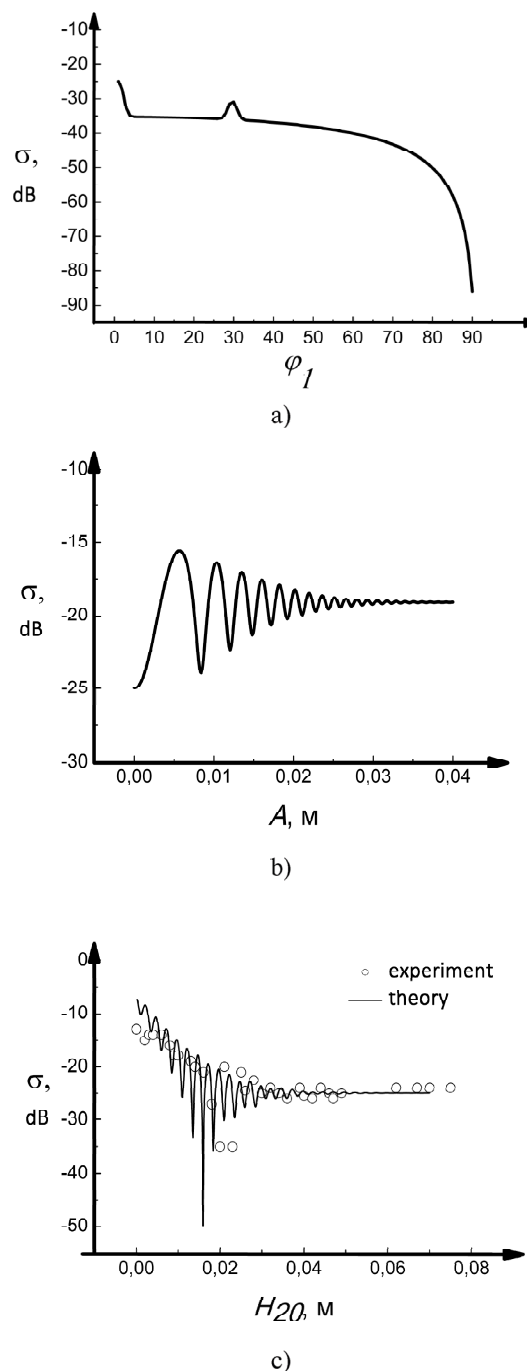


Fig. 2. – Backscattering from sand in which is located a metal disc: a) – The angular dependence of backscattering (disk at a depth of 0.015 M); b) – Dependence of backscattering from the disk's radius at normal incidence. The disk is located at a depth of 0.015M; c) – Backscattering in dependence on the depth disc at normal incidence.

um in the direction of the source can also be represented as

$$\langle E \rangle = h\alpha e^{-2\text{Im}(k_2)h_{02}}, \quad (8)$$

k_2 – wavenumber in the second medium. Equating (7) and (8), determine h_{20} :

$$h_{20} \approx \frac{1}{2\alpha} \frac{1}{\text{Im}(k_2)} \approx \frac{1}{\text{Im}(k_2)}, \quad \alpha \leq \frac{1}{2}.$$

This is the maximum depth of penetration of the field in an absorbing medium. The same parameter is the thickness of the skin layer.

Calculation formulas derived from the theory that uses a solution of the wave equation in the general form, ie, as a superposition of two opposing waves. Typically, on the basis of physical considerations of the various reasons in the decision leaves one wave. The experimental data are given in the point to the efficiency of use of all solutions of the wave equation, although from the point of view of mathematics is obvious.

The results of this paper confirm the existence of multi-mode mechanism of reflection and refraction.

This mechanism implies that physical reflection and refraction occurs in a transition layer. This transition layer is called a skin layer. In this layer, there are opposing waves that provide a reciprocal link and the interface boundary of the skin layer.

References

1. Yacubov, V. P., Philipov, S. E., Sukhanov, D. Ya., and Klokov, A. V. (2014). In. *Radiovolnovaya tomografiya: dostizhenia i perspektivi*, Tomsk, Russia : NTL.
2. Andrianov, A. V., Astanin, L. Yu., Bodrov, V. Yu. [etc.]. (2005). In. *Voprosi podpoverkhnostnoi radiolokatsii*, Moscow, Russia : Radiotekhnika.
3. Lomukhin, Yu. L. (2014). A mathematical model of multimode reflection and refraction of waves. *Vestnik BGU*, 2, 29-34.
4. Brekhovskih, L. M. (1973). *Waves in layered media*, Moscow, Russia : Nauka.
5. Kochetkova, T. D., Suslyayev, V. I., Jhuravlev, V. A., Korovin, E. Yu., and Solov'eva, T. P. (2012). *Izmerenie vlajhnosti pochv s ispolzovaniem neregulyarnogo micropoloskovogo rezonatora*, 3-2, 170-174.

INVESTIGATIONS OF SOME NEW FOCUSING PROPERTIES OF CUBOID-AIDED PHOTONIC JET

I.V. Minin¹, O.V. Minin¹, V.I. Suslyayev¹, I.O. Dorofeev¹, V.P. Yakubov¹, V. Pacheco-Pena², M. Beruete²

¹National Research Tomsk State University, Tomsk, Russia

²Antennas Group - TERALAB, Universidad Publica de Navarra, Campus de Arrosadia, 31006, Pamplona, Spain

Correspondence to:

I. V. Minin

Post Address: Tomsk State University, 36 Lenin Ave., Tomsk, Russia, 634050

E-mail: prof.minin@gmail.com

Citation:

Minin, I. V., Minin, O. V., Suslyayev, V. I., Dorofeev, I. O., Yakubov, V. P., Pacheco-Pena, V., and Beruete, M. (2016). Investigations of some new focusing properties of Cuboid-Aided Photonic Jet. In *Actual problems of radiophysics. Proceedings of the VI International Conference "APR-2015"*, (pp. 32-35). London: Red Square Scientific.

Published: 14 October, 2016

This is an open access article of the Creative Commons Attribution-NonCommercial-NoDerivs License, which permits use and distribution in any medium, provided the original work is properly cited, the use is non-commercial and no modifications or adaptations are made.

Abstract. It is shown that the effect of the photonic jet can be obtained on the photonic crystal cuboids (metacuboid). This effect can be used to increasing the resolution of micro- solid lens optical microscopy and coupling from the photonic molecule into other photonic components such as planar waveguides or coaxial cables.

Keywords: photonic jet, metacuboid, multifrequency focusing, polarization properties, cuboids.

The fundamental question in application to photonic jet is: is a hemispherical-aided shape of dielectric particle to form a photonic jet unique or the spherical shape of particle may be extended to other form?

To manage the whole set of PNJ parameters and optimize their characteristics additional free parameters are needed. In particular, PNJ parameters management by, for example, choosing the particle shape (cube, triangle, pyramid, hexagonal, etc) has been studied [1]. In work [1] it was also shown for the first time that photonic terajets (analog of optical PNJ) may be formed also in case of plane wave front interaction with mesoscale cubic dielectrical structure.

Although analytical solutions of the vector diffraction problem can be obtained for selected objects (sphere, halfplane, cylinder) [2] the boundary conditions on the electromagnetic field for other dielectric structures makes the analytic solution impossible. In order to evaluate the focusing performance of the structure, the transient solver of the commercial software CST Microwave StudioTM was used along with an extra fine hexahedral mesh with a minimum mesh size of $\lambda_0/45$.

Metacuboid-Aided Photonic jet

In this sub-chapter we suggest a metamaterial structure whose properties are determined not only by its inner geometry but also by its entire 3D shape. We evaluate the potential of this structure to control both the size and the location of the field enhancement (photonic jet). The idea of metacuboid-aided photonic jet is to take a dielectric cuboid particle [1], and then realize it using a photonic crystal operating as an effective medium, that is, in the so-called metamaterial regime. This can be done using two dimensional photonic crystal consisting of parallel rods in air host medium, or air cylindrical holes inside dielectric matrix. Both of them can be homogenized and then it is possible to realize the specified cuboid. In that case, cuboid made as a PhC would be polarization dependent, it would work only for the polarization for which effective refractive index is equal to cuboid material.

A dielectric plate with cavities of various shapes is one of man-made dielectric type in which the effective dielectric permittivity is reduced in comparison with a solid dielectric because the fraction of volume that the dielectric occupies is reduced. The perforations result in changing the effective dielectric constant of the dielectric material [3–5]. In Reference [3] the results of an experimental investigation of a perforated dielectric in the resonance

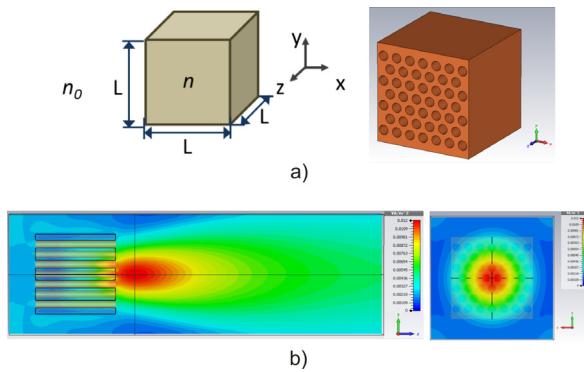


Fig. 1. a) – schematic view of dielectric metacube concept; b) – simulation of photonic jet by metacuboid.

region were discussed. In our preliminary investigations we used a triangular perforation cell [6–7]. To minimize the losses to reflection we have selected $\alpha \approx 0.4342$ which corresponds to $\epsilon_r \approx 3$. Taking into account that $\sqrt{\epsilon_{eff}} = n_{eff} = 1.46$ [7] the parameters of the triangular cell are: $\alpha \approx 0.4342$, $s \approx 0.1445 \lambda$, $d \approx 0.1 \lambda$. The 3D elementary dielectric metacube with dimension $L \times L \times L$ ($L = \lambda$) is schematically shown in Figure 1. The whole structure is illuminated by using a vertically polarized plane wave (E_y) with its propagation direction along the optical z -axis.

Simulation results are shown in the Figure 1b. The ellipticity (defined as the ratio between both transversal resolutions $FWHM_x / FWHM_y$) [7] of jet are close to 1. Therefore, a quasi-spherical spot is obtained for the metacuboid configuration. The parameters of a jet are: $FWHM_x = 0.618 \lambda$, $FWHM_y = 0.617 \lambda$, $FWHM_z = 1.89 \lambda$.

For the second variant of metacuboid we have selected the parameters as follows: $\epsilon_r \approx 2.75$, $\alpha \approx 0.3092$, $d \approx 0.1 \lambda$, $s \approx 0.17126 \lambda$. The photonic jet parameters are: $FWHM_x = 0.555 \lambda$, $FWHM_y = 0.542 \lambda$, $FWHM_z = 1.61 \lambda$.

It could be noted that the proposed metacuboid structure is *birefringent* – the focus for TM mode is near the backside of the photonic crystal, while for TE mode it is exactly on the back side. These results suggest novel directions in the study of the intriguing properties of metamaterials / photonic crystals aided photonic jets. It could be interesting for future investigations, especially since it is not easy to manufacture birefringent focusing lenses.

Thus a concept and principal possibilities of photonic jet formation based on metamaterial cuboid is shown. So the photonic crystals in general have served

to revisit old and apparently well-established concepts, shading new light on them. They have been the playground where physicists and engineers have worked together and this has produced a very fast development of new ideas and applications. We hope we are opening new research lines such as mesoscale metamaterial focusing devices for sensing applications.

Multifrequency focusing of Terajets

It was also demonstrated [8] that terajets formation on the basis of dielectrical cuboids is possible not only on fundamental harmonic, but also on other even frequency harmonics and also in case of the plane wave front oblique incidence. Dielectric cuboid here acts as a flat lens with PNJ being a focus.

One important aspect to evaluate is the frequency response of the terajet keeping the dimensions constant. Let's now consider the focusing possibilities of dielectric cuboids with fixed wavelength but different dimensions (it is equivalent to the frequency harmonic properties). The results of FDTD simulations are shown in the Figure 2. The main focusing characteristics of photonic jets are given in the Table 1.

The analysis of the results shown that the focusing properties are saved when the size of the cube increases by an even number of times, and the localization of radiation deteriorates with increasing the size of cube in an odd number of times. Also it is interesting to note that ellipticity of the photonic jet (resolution x/y) is almost constant up to multiply factor of $M = 4$.

It is also followed from the simulations that changing the dimension of the dielectric cuboid (factor M), the focus point is moved from inside to outside the cuboid and the focal length increases as dimension increases. At large dimension of M , the photonic jet is formed rather far from the shadow of the cuboid, and a decrease in dimension the coordinate

Table 1. Focusing characteristics of photonic jets

Cuboid dimensions, multiply factor M	FWHM x, λ	FWHM y, λ	FWHM z, λ
1	0.45	0.43	1.1
2	0.51	0.49	1.2
4	1	0.95	4.74
5	1.06	1.45	> 22
6	1.4	1.16	7.83
8	1.77	1.56	13

of the focal spot reaches the cube edge. The results show that the length of photonic jet is elongated greatly with high value of M . As for FWHM vs factor M these dependences may be approximated by the following linear expressions (as it follows from the Table 1):

$$X = 0.434M + 0.413, Y = 0.382M + 0.583,$$

where X, Y – the FWHM along X, Y axis in the unit of FWHM along X at $M = 1$, respectively. The approximation of $FWHM_{x, y} \approx \alpha_{x, y} M$ for $M = \text{even}$ is also valid. So the location and 3D size of the photonic jet depend on the dimension of the dielectric cuboids'. Thus the properties of photonic jet can be controlled by the variation of the dimensions of the dielectric cuboid.

The results described above showed a rich structure in the high spatial frequency components of the photonic jet. As it can see in direct space, each propagative spatial frequency corresponds to propagation at given angle with respect to the beam axis. An example of intensity map of a photonic jet is presented on a colored map in Figure 3. The angles corresponding respectively to the first few maxima and the minima of the field intensity are displayed respectively with red lines and black lines in this Figure. The maxima correspond to high intensity angles while the minima correspond to angles of low intensity regions. The maxima in the spectral distribution can therefore be associated with the presence of secondary lobes in the direct field structure. The first secondary lobes tend to confine the central lobe into a low divergent beam, while the secondary lobes with high transverse components tend to reduce the length and the waist of photonic jets.

Polarization properties of mesoscale regular hexahedron-aided terajet

Polarization of incident wavefront is an important parameter, which is helpful in the search for longitudinally and transversally subwavelength photonic jets.

Beam shaping of nanojet by polarization engineering were considered in Reference [9], where the authors used a $2\text{-}\mu\text{-diameter}$ latex sphere ($D/\lambda = 3$) with $RIC = 1.2$. It has been shown that when the microsphere is illuminated by linear and circular polarization beams, the axial field intensity profile is the same. Azimuthal polarization incident beam induces a doughnut beam along the optical axis and compared with linear and circular polarizations, both the transverse FWHM and axial half-decay length of the

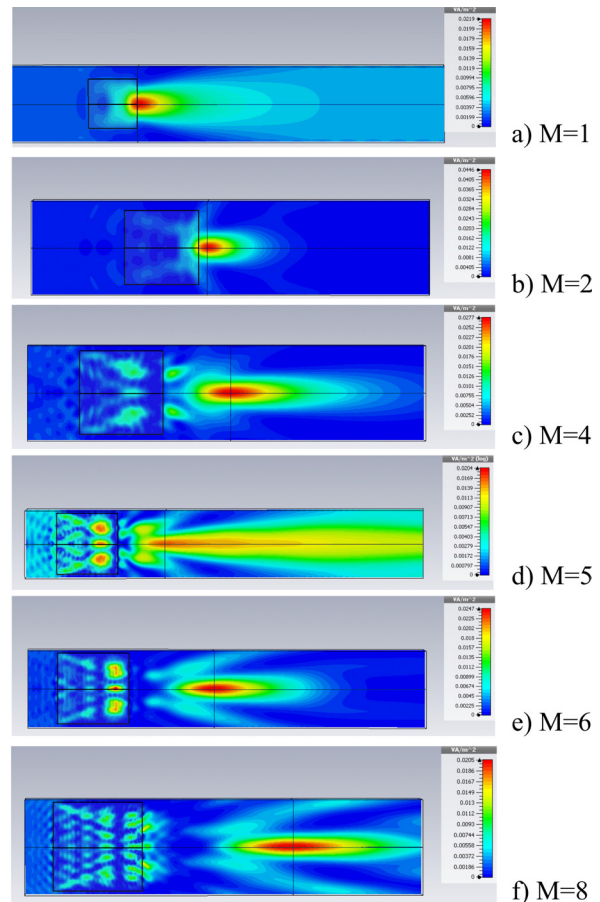


Fig. 2. – Field intensity distributions in ZX plane for dielectric cuboids with different dimensions: the initial dimension of the cuboid was $1 \times 1 \times 1$ in wavelength and the next cuboids dimensions were multiply by factor which shown near the Figure. Factor $M = 1$ corresponds to the original dimensions of the 3D cuboid. The factors $M = 2-8$ correspond to simulation results when the dimensions of the original cuboid are multiplied for this value.

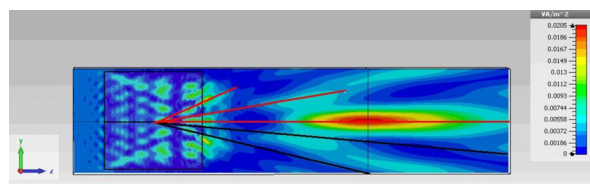


Fig. 3. – Scattered intensity of a photonic jet produced by a dielectric cuboid with factor $M = 8$. The angles corresponding to the maxima and minima in the spatial frequency are displayed in direct space, respectively, by red and black lines.

Table 2. PNJ vs polarization of illumination wavefront

Polarization/ FWHM	X, λ	Y, λ	Z, λ	Ellipticity	Q
Linear	0.46	0.43	1.08	1.07	2.51
Circular	0.51	0.52	1.08	0.98	3.83
Diagonal	0.44	0.44	1.08	1.0	4.89

photonic nanojet are clearly decreased by the radial polarization incident beam, with the maximum intensity being close to the microsphere.

The changes of the photonic jet demonstrate its maximum field intensity and quality criterion of the jet (Q). The complex characteristic of a PNJ can be given with the aid of the modified so-called "quality criterion Q" [10], which combines all relevant jet parameters. We define Q as: $Q = L_{jet} I_{max} / \min(\text{FWHM}_{x,y})$ – the PNJ beam length L_{jet} is FWHM along z-axis, I – maximal value of field intensity along the photonic jet (in Table 2 – relative to cuboid with linear polarization). Thus the photonic jet's length was calculated as the FWHM_z of intensity outside the particle (i.e., if the maximum intensity was found inside the particle, the half-maximum was counted from the surface).

Simulations showed that for circular polarization the electric field maximum is moved away from the surface of the 3D cuboid (it is a regular hexahedron of side $L = \lambda_0$, with refractive index contrast $n = 1.46$) along the optical axis (z). The parameters of PNJ for different polarization state of incident wavefront for the cuboid are shown in the Table 2.

For the circular polarization of incident wavefront the localized field intensity (photonic jet) have no the subdiffractive dimensions instead of linear polarization.

This physical phenomenon for cuboids briefly described above could be a significant implement in the fields of photonic circuit. The photonic jets, for example, permit the lightwave coupling from the photonic molecule into other photonic components such

as planar waveguides or coaxial cables. The cuboid-aided photonic jet allows also increasing the resolution of micro-solid lens in optical microscopy, etc.

This work was partially supported by the Mendeleev scientific fond of Tomsk State University No. 8.2.48.2015.

References

1. Minin, I. V., and Minin, O. V. (2014). Photonics of isolated dielectric particles of arbitrary three-dimensional shape – a new direction in optical information technology. *Vestnik NGU, Ser. "Information technology"*, 12(4), 59-70.
2. Born, M., and Wolf E. (1999). *Principles Of Optics*, 7th ed. New York : Cambridge University Press.
3. Meriakri, V. V., and Nikitin, I. P. (1989). Man-made dielectric with dispersion in the millimeter wavelength band. *Quasioptical devices in millimeter and sub-millimeter wavelength ranges*. In. *Proceedings of IRE*, Har'kov, 65-70..
4. Petosa, A., Ittipiboon, A., and Thirakoune, S. (2002). Perforated dielectric resonator antennas. *Electronics Letters*, 38(24), 1493-1495.
5. Zhang, Y., and Kishk A. A. (2007). Analysis of dielectric resonator antenna arrays with supporting perforated rods. In. *2nd European Conf. on Antennas and Propag., EuCAP 2007*, 1-5.
6. Fabre, N., Fasquel, S., Legrand, C., Melique, X., Muller, M., Francois, M., Vanbeien, O., and Lippens, D. (2006). Towards focusing using photonic crystal flat lens. *Opto-Electron. Rev.*, 14(3), 225-232.
7. Pacheco-Pena, V., Beruete, M., Minin, I. V., and Minin, O. V. (2014). Terajets produced by 3D dielectric cuboids. *Appl. Phys. Lett.* 105, 084102.
8. Pacheco-Pena, V., Beruete, M., Minin, I. V., and Minin, O. V. (2015). Multifrequency focusing and wide angular scanning of terajets. *Opt. Letters*, 40(2), 245-248.
9. Yong Liu, Baoyong Wang and Zhihua Ding. (2011). Influence of incident light polarization on photonic nanojet. *Chin. Opt. Lett.*, 9(7), 072901.
10. Kong, S.-C., Taflove, A., Backman, V. (2009). Quasi one-dimensional light beam generated by a graded-index microsphere. *Opt. Express*, 17, 3722-3725.

SPECIAL FEATURES OF ELECTROMAGNETIC WAVE PROPAGATION IN A THREE-LAYER CYLINDRIC WAVEGUIDE WITH RIGHT- AND LEFT-HANDED MEDIA

V.A. Meshcheryakov

National Research Tomsk State University, Tomsk, Russia

Correspondence to:

V. A. Meshcheryakov
Post Address: Tomsk State University, 36 Lenin Ave., Tomsk, Russia, 634050
E-mail: mva@mail.tsu.ru

Citation:

Meshcheryakov, V. A. (2016). Special features of electromagnetic wave propagation in a three-layer cylindric waveguide with Right- and Left-Handed Media. In: *Actual problems of radiophysics. Proceedings of the VI International Conference "APR-2015"*, (pp. 36-39). London: Red Square Scientific.

Published: 14 October, 2016

This is an open access article of the Creative Commons Attribution-NonCommercial-NoDerivs License, which permits use and distribution in any medium, provided the original work is properly cited, the use is non-commercial and no modifications or adaptations are made.

Abstract. Results of computer modeling of the coefficients of waveguide mode propagation in a three-layered circular screened waveguide are presented. The middle layer of the waveguide is filled with the LHM (Left-Handed-Medium) having a negative refractive index. The results presented here suggest that complex waves, waves with anomalous dispersion, and waves with significant slowdown of the phase velocity exist in such waveguides.

Keywords: electromagnetic wave, metamaterials, LHM (Left-Handed-Medium), circular waveguide, complex waves, phase velocity.

Introduction

The specificity of the physical phenomena of electromagnetic waves reflected and refracted at the interface between Right – and Left-Handed Media (RHM, LHM), predicted by V.G. Veselago [1] has stimulated the modeling of wave propagation in such media [2–16]. In [5] results of modeling of wave processes in the two-layered waveguide with central RHM and external LHM layers were presented. New properties of the waveguide with a LHM adjoining its wall were indicated. In the two-layered screened waveguide whose central layer has negative refractive index and external layer represents an air layer, both the wave process and the cutoff regime of waveguide mode propagation can be observed for definite internal layer radii. The layer of the left-handed medium leads to the occurrence of modes with large retardation coefficient. Regions of complex waves (without losses in the filling media) are observed. There are waves with anomalous behavior of the propagation parameter.

In [6] results of modeling of wave processes in the two-layered waveguide with central LHM and external RHM layers were presented. New properties of the waveguide with the LHM positioned in the center of the waveguide were specified. In the two-layered screened waveguide, both the wave process and the cutoff regime of waveguide mode propagation can be observed for definite internal layer radii. The layer of the left-handed medium leads to the occurrence of modes with large retardation coefficient. Regions of complex waves (without losses in the filling media) are observed. The presence of the central LHM layer leads to the occurrence of the frequency transparency windows. The waveguide represents a bandpass filter.

The purpose of the present work is computer modeling of wave processes in a circular waveguide with three layers material: *RHM-LHM-RHM*.

Problem formulation

Figure 1 shows the cross section of the two-layered waveguide with ideally conducting external screen and indicated initial normalized material and geometrical characteristics of the layers. The cylindrical system of coordinates γ, ϕ and z_0 is used. The layer radii and the longitudinal coordinate were normalized by the wave number in free space: $r_{1,2,3} = k_0 r_{1,2,3}$, $z = k_0 z_0$, and

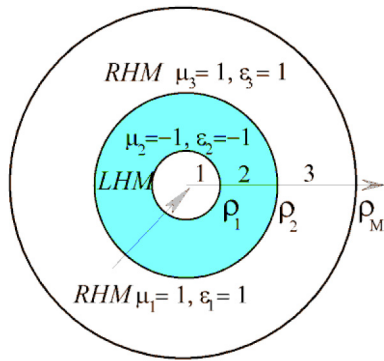


Fig. 1. – Three-layered waveguide.

$k_0 = \omega/c$, where c is the velocity of light in free space and ω – is the circular frequency of the electromagnetic process.

The waves propagate along the z coordinate perpendicular to the Figure plane. The dependence of the field components on the azimuth (ϕ) and longitudinal coordinates is chosen in the form $-\exp(in\phi + i\beta z)$, where n is the serial azimuth number, β is the complex propagation constant, and $i = \sqrt{-1}$. The dispersion equation for calculation of the propagation constants of natural waves follows from the fulfillment of the boundary conditions for the tangential field components on the interface between the layers and on the waveguide screen. The examined characteristics are the normalized propagation constants $\Gamma = \beta/k_0 = c/v$ for waveguide modes, where v is the phase velocity of the wave in the waveguide. The imaginary character of indicates the absence of wave process and the exponential decay of the field of the cutoff mode (in terms of microscopic metamaterial structure, this implies the energy accumulation in reactive elements). The complex character of modeled quantities (more exactly, the occurrence of complex-conjugated pairs) employs the propagation of complex modes.

The purpose of modeling is to elucidate the influence of the thickness of the central layer and its dielectric permittivity on the value for different waveguide modes.

Results of model experiments

Figure 2 shows plots of the dependence of the propagation constant on the radius ρ_2 for four waves with a one variation in the azimuth. The axes of the real ($\text{Re}(\Gamma)$) and imaginary ($\text{Im}(\Gamma)$) components of the propagation constant are combined in one axis in

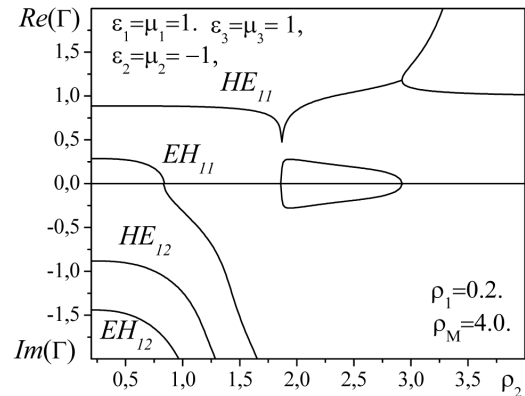


Fig. 2. Dependence of the propagation parameter Γ on the radius ρ_2 . The radius $\rho_1 = 0.2$.

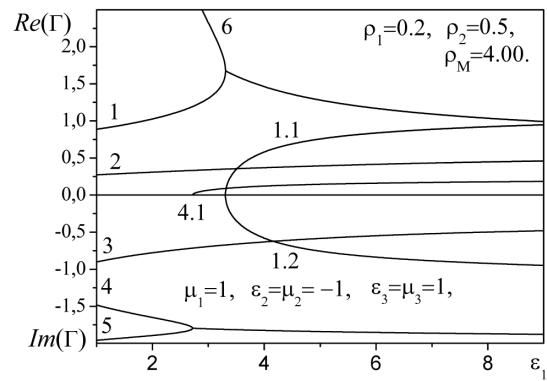


Fig. 3. Dependence of the propagation parameter Γ from the dielectric constant ϵ_1 .

Figure 2. This allows us to track the transition of modes from the cutoff to the propagation region. Parameters materials and geometrical characteristics of the waveguide are indicated in the Figure 2. If you replace the *LHM* layer on the layer *RHM* constants propagation modes are calculated by a known in the scientific literature formula. In this work not considered modes having axial symmetry (the first subscript in the name of the mode is not equal to zero). The analysis of the results for the empty waveguide ($\rho_1 = \rho_2$) give the two propagating modes ($H_{11} \rightarrow HE_{11}$, $E_{11} \rightarrow EH_{11}$) with real parameters distribution and two (or more) “cutoff region” modes ($H_{12} \rightarrow HE_{12}$, $E_{12} \rightarrow EH_{12}$) with imaginary values. An increasing radius ρ_2 leads to the “cut-off” mode EH_{11} . This result is new. It can be explained from the position of the partial waves. Into *LHM*, the direction of propagation of the beam becomes opposite. With increasing

thickness of the *LHM* paths in the forward and backward directions become equal, the constant of propagation $\Gamma_{EH_{11}}$ tend to zero. With increasing thickness of the LCM high modes goes into a deep cut-off.

There is another new phenomenon. There is a point of bifurcation, characteristic of complex waves of multilayer waveguides with *RHM* layers. Instead of two modes, with different constants propagation, there is a pair of modes with complex conjugates values.

A further increase in the thickness of the *LHM* leads to the appearance of mode with decreasing phase velocity of propagation ($\Gamma \rightarrow \infty$). The appearance of complex waves in multilayer structures with the "right" materials is a known phenomenon. The complex modes is formed from hybrid waves HE_{mn} and EH_{mn} . They have the same indexes. If there is a *LHM*, the complex pair is obtained from the main mode and "slow" modes. This is a new result.

The appearance of a mode with a high deceleration rate is accompanied by a propagating mode with anomalous behavior (increase of ρ_2 leads to a decrease of Γ). Similar to the behavior of some waves it was shown in [5–7].

The results shown in Figure 3 demonstrate the dependence of the propagation parameter Γ from the dielectric constant ϵ_1 ($\rho_1 = 0.2$, $\rho_2 = 0.5$, $\rho_M = 4.0$). The segments of the curves marked by Figure 1, 2, 3, 4 indicates the presence in the waveguide of four modes: HE_{11} , EH_{11} , HE_{12} , EH_{12} .

Computer modeling demonstrated the presence in the waveguide of the mode with a very large propagation constant (curve 6) that was not observed in the waveguide with the right-handed media. An increase in the dielectric constant of the central layer leads to significant increase Γ of the mode HE_{11} (curve 1). Summary of the segments 1, 6 demonstrates the presence of the mode with anomalous dispersion. The examined modes merge at the bifurcation point and engender two modes with complex conjugated propagation constants (curves 1.1, and 1.2). The modes merge at the bifurcation point and engender two modes with complex conjugated propagation constants (curves 1.1, and 1.2). The waves (curves 4 and 5) merge at the bifurcation point and engender two modes with complex conjugated propagation constants (curves 4.1). For the given waveguide, this result is also new.

The radius of the central layer is chosen 1 ($\rho_1 = 1.0$) for a more detailed review of the field of the existence of complex modes in the change in the dielectric constant of the inner layer. This allowed us to extend the scope and consider its boundaries. In Fig-

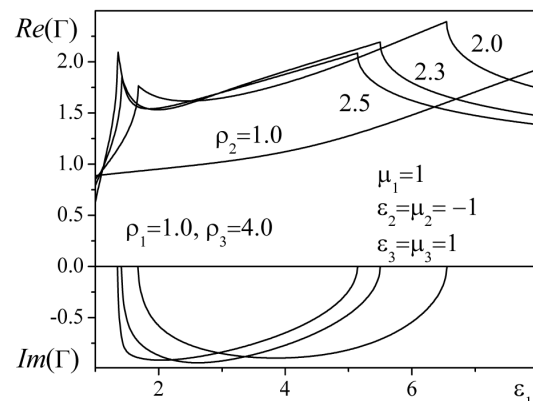


Fig. 4. – Dependence of propagation constants from the radius for the modes, which arose after passage of the bifurcation point (modes with numbers 1 and 6 in Figure 3).

ure 4 presents the plots of the dependence of propagation constants from the radius for the modes, which arose after passage of the bifurcation point (modes with numbers 1 and 6).

If the *LHM* layer is absent ($\rho_1 = \rho_2 = 1.0$), the permeability variation ϵ_1 of the complex wave does not occur. If the *LHM* layer is absent ($\rho_1 = \rho_2 = 1.0$) then the variation of permeability leads to the appearance of complex waves. If the *LHM* layer is absent ($\rho_1 = \rho_2 = 1.0$) then the variation of permeability it is not leading to the appearance of complex waves.

A monotonic increase in the propagation constant of the mode HE_{11} is observed. In Figure 4 shows curves for three values of the radius of the outer layer *LHM*: 2.0, 2.3, 2.5. The Figure shows the imaginary parts of G with a minus sign. The imaginary parts of G with a plus sign is not shown. They have a similar appearance. They differ only in sign. Analysis of the results shows that with increasing the area of the existence of complex modes is reduced. The second mode, which occurs when the output of their region of existence of complex waves with increasing permeability, not shown in the Figures. While it is safe to say that the parents of these complex waves is the basic fashion and fashion with a high deceleration rate (6). A more thorough analysis requires the simulation of electromagnetic field components and energy flow of these waves in the waveguide.

Conclusions

In the course of computer modeling, different variants of relationship between the thickness of the internal and external dielectric layers made from the

right-handed material and the layer of the left-handed material have been studied. Thus, we can indicate the following special features of electromagnetic wave propagation in the examined waveguide:

1. With increasing thickness of the *LHM* high modes goes into a deep cut-off.
2. The layer of the left-handed medium leads to the occurrence of modes with large retardation coefficient.
3. There is a point of bifurcation, characteristic of complex waves of multilayer waveguides with *RHM* layers.

The appearance of a mode with a high deceleration rate is accompanied by a propagating mode with anomalous behavior.

This Research is supported by Tomsk State University Competitiveness Improvement Program.

References

1. Veselago, V. G. (1967). *Sov. Phys. Usp.*, 10, 509-514.
2. Smith, D. R. [et al.]. (2000). *Phys. Rev. Lett.*, 84, 4184-4187.
3. Pendry, J. B. (1994). *J. Mod. Optic.*, 41 (2), 209-229.
4. Ward A. J., and Pendry J. B. (1996). *J. Mod. Optic.*, 43 (4), 773-793.
5. Dunaevskii, G. E., Meshcheryakov, V. A., Zhuravlev, V. A., Suslyaev, V. I., and Bashlykov, A. K. (2009). *Russian Physics Journal*, 52 (12), 1325-1330.
6. Dunaevskii, G. E., Zhukov, A. A., and Meshcheryakov, V. A. (2015). *Russian Physics Journal*, 57(9), 1225-1229.
7. Meshcheryakov, V. A., and Zhuravlev, V. A. (2015). In. *Progress in Electromagnetics Research Symposium, 2015, January*, 2107-2109.
8. He, J., and Sailing, He. (2006). *IEEE, Microwave and Wireless Components Letters*, 16 (2), 96-98.
9. Salehi, H., and Mansour, R. (2005). *IEEE, MTT*, 53, 3489-3497.
10. Suping, Li, Zihua, W., and Wei Wu (2010). In. *3rd IEEE International Conference: 2010, Multimedia Technology (IC-BNMT)*, 1145-1149 .
11. Mousa, H. M., and Shabat, M. M. (2013). *Antenna Technology (iWAT)*, 286-289.
12. Paul, O. [et al.]. (2008). *Opt. Express*, 16, 6736-6744.
13. Nashed, A. I., Chaudhuri, S. K., and Safavi-Naeini, S. A. (2010). *Antennas and Propagation Society International Symposium (APSURSI)*, 1-4.
14. Barroso, J. J., Castro, P. J., and Neto, J. P. L. (2009). *Microwave and Optoelectronics Conference (IMOC)*, 778-782.
15. Meshcheryakov, V. A. (2014). 24th International Crimean Conference Microwave and Telecommunication Technology (CriMiCo 2014). *Conference Proceedings*, 6959531, 570-571.
16. Meshcheryakov, V. A. (2014). 24th International Crimean Conference Microwave and Telecommunication Technology (CriMiCo 2014). *Conference Proceedings*, 6959524, 553-554.

ELECTROMAGNETIC PROPERTIES OF CARBON NANOTUBES COMPOSITES: PVA VS SAC

A.G. Paddubskaya¹, A. Plyushch², A.V. Kukhta^{3,5}, P.P. Kuzhir³,
S.A. Maksimenko³, T. Ivanova⁴, R. Merijs-Meri⁴, J. Bitenieks⁴, J. Zicans⁴,
V.I. Suslyayev⁵, M.A. Pletnev⁶¹Center for Physical Sciences and Technology, Vilnius, Lithuania²Vilnius University, Vilnius, Lithuania³Research Institute for Nuclear Problems of Belarusian State University, Minsk, Belarus⁴Rigas Techniques University, Faculty of Material Science and Applied Chemistry, Riga, Latvia⁵Tomsk State University, Tomsk, Russia⁶Kalashnikov Izhevsk State Technical University, Izhevsk, Russia

Correspondence to:

A. Plyushch
Post Address: Vilnius University,
9, Sauletekio aleja, LT-00122
Vilnius, Lithuania.E-mail:
artyom.plyushch@gmail.com

Citation:

Paddubskaya, A. G., Plyushch, A., Kukhta, A. V., Kuzhir, P. P., Maksimenko, S. A., Ivanova, T., Merijs-Meri, R., Bitenieks, J., Zicans, J., Suslyayev, V. I., and Pletnev, M. A. (2016). Electromagnetic properties of carbon nanotubes composites: PVA vs SAC. In *Actual problems of radiophysics. Proceedings of the VI International Conference "APR-2015"*, (pp. 40-44). London: Red Square Scientific.

Published: 14 October, 2016

This is an open access article of the Creative Commons Attribution-NonCommercial-NoDerivs License, which permits use and distribution in any medium, provided the original work is properly cited, the use is non-commercial and no modifications or adaptations are made.

Abstract. Results of comparative electromagnetic analysis of polymer composites comprising multiwall carbon nanotubes (MWCNT) and a polymer, i.e. styrol acrilate copolymer (SAC) or polyvinyl acetate (PVA), as a matrix in radiofrequency (20 Hz–1 MHz) and microwave (26–37 GHz) frequency ranges are presented. It has been found that the SAC is preferable for usage in low frequency range due to significantly smaller (below 0.5 wt. %) percolation threshold of dispersed nanotubes in comparison with that of PVA based composites (above 2 wt. %). However, due to electromagnetic coupling one does not feel this significant difference between two polymers under investigation at microwave frequencies, and both PVA and SAC composites filled with 0.5–2 wt. /% of MWCNTs demonstrate high attenuation of electromagnetic power at the level of 40–80% by 0.4 mm thick polymer coating.

Keywords: carbon nanotubes, composite materials, PVA, SAC, electromagnetic shielding.

Introduction

Due to attractive consumer properties such as mechanical, chemical and temperature stability, light weight, etc. polymer composites get much attention in research work forming a basis for the design of a variety of perspective multifunctional materials. In particular, a widely-studied field of material science is the development of novel conductive substances based on insulating polymer matrix and small amount of conductive inclusions aimed at the effective electromagnetic interference shielding [1–11].

Normally, metallic particles are used as a functional filler to impart conductivity to composites. However, recently carbon micro- and nano-sized inclusions have been proposed as prospective cheap alternative to metallic particles. Among them are carbon nanotubes [3, 4], fullerenes and onion-like carbon [1, 5], graphene nanoplatelets [2] and other graphite-like structures [9]. It should be mentioned that due to high aspect ratio carbon nanotubes demonstrate the best shielding abilities. Previous works [6, 7, 8] demonstrate that 1 mm thick CNT/polymer composite film with 2 wt. % of nanotubes provides high level of electromagnetic shielding whereas mechanical properties of the film remain unchanged due to such small amount of inclusions. It worth mentioning that the values mentioned are strongly influenced not only geometrical properties of CNTs but also additional factors such as time of sonication and CNTs surface functionalization [8] (they both prevent agglomeration of CNTs in composite).

Selection of polymer matrix is also of importance in the composites design, because polymer viscosity is critical for obtaining homogeneous distribution of nano-sized inclusions during preparation process and after, when reagglomeration of inclusions takes place during curing process. As a result,

composites with same nanotubes at same amounts embedded into different polymer matrices may demonstrate significantly different conductivity and shielding ability. Usually epoxy resin, polystyrol, polyurethane, polymethyl methacrylate are utilized as matrices. In the present work we compare composite materials with styrol acrilate copolymer (SAC) and polyvinyl acetate (PVA) as host media. Despite wide utilization of SAC and PVA as water resistant and protective coating materials, there is only few attempts for designing EMI shielding composites with such polymers as matrices [6].

Samples preparation and experimental details

In our work we used commercially available Bayer (Baytubes®C 150P, Bayer MaterialScienceAG, Germany) CVD multi-walled carbon nanotubes (MWCNT). Accordingly to the producer's datasheet MWCNTs parameters are as follows: bulk density 130–150 kg/m³, length >1 μm, inner diameter 4±2 nm, outer diameter 11±3 nm, purity 95%, initial agglomerates size 0.1–1 mm [12].

PVA (FINNDISP HW 1) and SAC (FINNDISP A 10) were used as matrices for the fabrication of composite samples, their main physical and chemical properties are presented in Table 1. The composites synthesis method has been described in details elsewhere [10, 11]. Briefly, MWCNTs were sonicated during 30 min in 1% solution of sodium dodecyl sulfate (SDS). After sonication, suspension of MWCNT was mixed with appropriate quantity of polymer emulsion in water. Utilization of a surfactant prevent agglomeration and release nanotubes in a stable suspension [13, 14]. As prepared suspension poured in Petri dish and left for a couple of days for curing. In order to improve properties of matrices and homogeneity of nanotubes' distribution, samples were thermally treated. The homogeneity was controlled via

scanning electron microscopy. Composite materials with 0.05, 0.1, 0.5, 1 and 2 wt. % of nanotubes well-dispersed in SAC and PVA matrices have been prepared (further in the text they are referred to as SAC/MWCNT and PVA/MWCNT, respectively).

The complex dielectric permittivity ϵ^* was measured with a LCR HP4284A meter. The equivalent electrical circuit was selected as capacitance and loss tangent. From these quantities, the complex dielectric permittivity was calculated using the planar capacitor formula. Square-like samples with the thickness about 0.4 mm and area of 5 mm² were investigated. Silver paste was used for contacting. The electrical conductivity σ was calculated according to $\sigma = i\omega\epsilon_0\epsilon''$, where ϵ_0 is the permittivity of vacuum, $\omega = 2\pi\nu$ is the angular frequency and ν is the measurement frequency.

The microwave measurements in the 26–37 GHz frequency range (Ka-band) were carried out with a scalar network analyzer R2-408R (ELMIKA, Vilnius, Lithuania). Parallelepiped samples of the thicknesses 0.4 mm were precisely cut to the waveguide cross section (7.2 × 3.4 mm). The EM responses of composites were measured as the ratios of transmitted/input (S_{21}) and reflected/input (S_{11}) signals. The dielectric permittivity was recalculated from the S parameters via methods described in [15].

Results and Discussion

Frequency dependencies of dielectric permittivity and conductivity of composite materials with different concentration of embedded MWCNTs at radiofrequency range are presented on Figure 1.

As we can see from Figure 1 both PVA and SAC matrices demonstrate insulating behavior and have similar dielectric permittivity (close to 10). Increasing of filler concentration leads to rise of both permittivity and conductivity. However, addition of small amount of nanotubes (lower than 0.5 wt. % for SAC/

Table 1. Main physical and chemical properties of PVA and SAC polymers.

Properties	PVA <i>FINNDISP HW 1</i>	SAC <i>FINNDISP A 10</i>
Viscosity at + 23 °C, mPa • s	12000–20000	200–1000
pH	4–5	7.5–8.5
Minimal film forming temperature, °C	7	17–19
Average particle size, μm	3–4	0.1
Glass transition temperature, °C	30 (22.7)	19 (15.4)
Density at + 23 °C, g/cm ³	1.07 (1.2)	1.04 (1.08)
Average water absorption of the film, %	31	14

ACTUAL PROBLEMS OF RADIOPHYSICS

Proceedings of the VI International Conference "APR-2015"

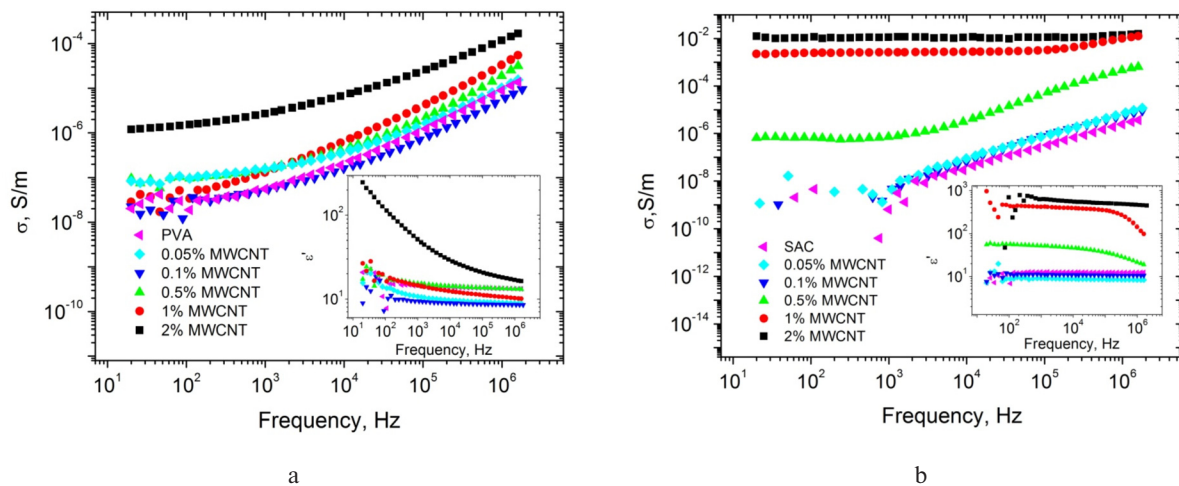


Fig. 1. – Conductivity and dielectric permittivity (on inserts) of composite materials with PVA (a) and SAC (b) as a matrices with different concentration of MWCNTs.

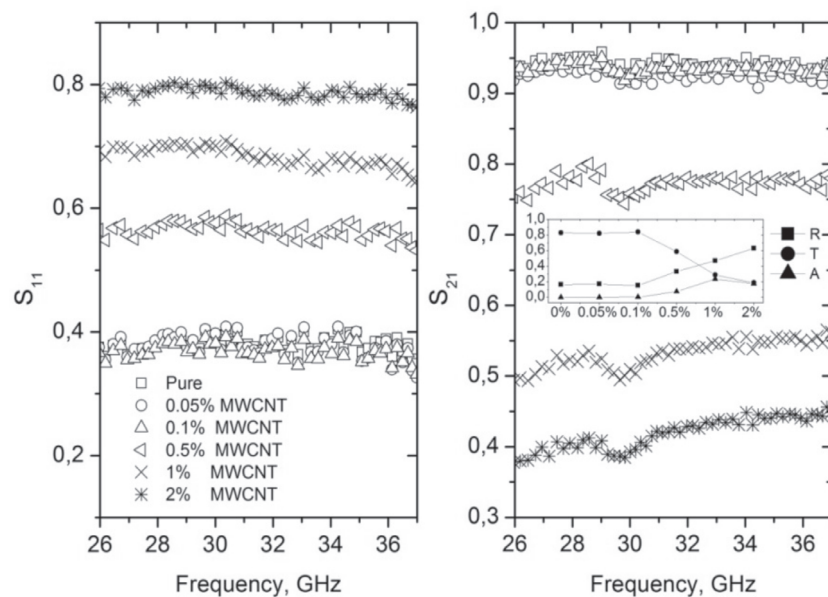


Fig. 2. – Frequency dependences of S-parameters of (a) PVA/MWCNT and (b) SAC/MWCNT composites. Inserts: concentration dependence of transmittance ($T = S_{21}^2$), reflectance ($R = S_{11}^2$) and absorbance ($A = 1-T-R.$) at 30 GHz. Sample thicknesses are in range 0.4–0.5 mm.

MWCNT composites and up to 2 wt. % for PVA/MWCNT composites) does not changes dielectric and conductive properties significantly, and frequency behavior of samples with low concentrations are mainly determined by properties of matrices. At higher concentrations, conductivity of SAC based composites demonstrate frequency-independent plateau at concentration of 0.5 wt. % and higher. According to universal power law, conductivity can be analyzed as a sum of two components: dc conductivity and ac conductivity [16]:

$$\sigma(\omega) = \sigma_{DC} + A\omega^s, \quad (1)$$

where σ_{DC} is the dc conductivity and $A\omega^s$ is the ac conductivity. Such behavior is caused by formation of a conductive network in the composite known as a percolation network. It is clearly seen from Figure 1, that percolation in SAC/MWCNT composites occurs between 0.1 and 0.5 wt. %, while PVA/MWCNT composites does not demonstrate percolation even for 2 wt. % of filler. Such difference can be explained with better distribution of nanotubes in SAC matrices. Fig-

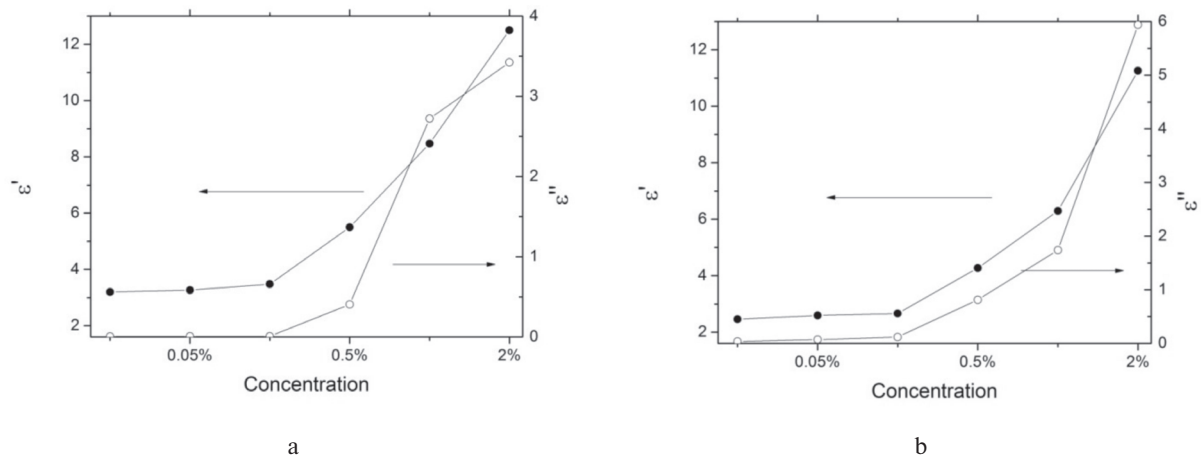


Fig. 3. — Concentration dependence of real and imaginary part of dielectric permittivity of (a) PVA/MWCNT (b) SAC/MWCNT composites.

ure 2 presents frequency dependences of S-parameters of composites at microwave frequencies.

Since in MW range we do not observe frequency dependencies of S parameters it is reasonable to continue analysis at a fixed frequency (in particular case 30 GHz). Both types of composites demonstrate improving of shielding properties with increasing of MWCNT concentration (see insert to Figure 2). It worth mentioning, that significant changes in reflection (R), transmission (T) and absorption (A) occurs for PVA composites not only when percolation concentration is achieved (between 0.1 and 0.5 wt.% of MWCNT inclusions). This is because MWCNTs at high frequencies are coupled electromagnetically, and the influence of better dispersion of carbon nanoparticles in SAC host is not so significant in GHz range [8]. Electromagnetic response of composites with 0.1 wt. % of MWCNT is the same as response of a pure polymer matrices, but further increasing of nanotubes amount leads to linear variation of studied values of T/R/A up to 19%, 63% and 18% for 2 wt. % of MWCNT for PVA/MWCNT composites and 17%, 55% and 28% for SAC/MWCNT. Dielectric permittivity of composites in microwave frequency range is presented at Figure 3.

Conclusions

We report comparative analysis of dielectric and electromagnetic properties of composite materials based on two types of polymer matrices, SAC and PVA, with addition of small (up to 2 wt. %) amount of carbon nanotubes. It is observed experimentally, that composites based on SAC matrix demonstrates

lower percolation threshold (below 0.5 wt. %) in comparison with PVA composites (above 2 wt. %). Absolute values of dc conductivity of SAC-based composites are in four orders of magnitude higher than that of PVA-based composites (10^{-2} S/m vs 10^{-6} S/m for composites with 2 wt. % of MWCNT). However, in microwave frequency range both SAC- and PVA-based composites demonstrate significant electromagnetic interference shielding efficiency as MWCNTs are coupled electromagnetically. We can conclude that if SAC matrix is favorable for further usages at low frequencies as anti-static coatings, both PVA and SAC polymers could be interesting for EMI-shielding composites designing and production.

Acknowledgements

This work was funded by Ministry of Education and Science of Russian Federation, grant ID RFMEFI57714X0141, and was partly supported by Tomsk State University through the Competitiveness Improvement Program.

References

1. Gavrilov, N. N., Okotrub, A. V., Bulusheva, L. G. [et al.]. (2009). *Technical Physics Letters*, 35 (1), 85-88.
2. Yousefi, N., Sun, X., Lin, X. [et al.]. (2014). *Adv. Mater.*, 26, 5480-5487.
3. Verma, P., Saini, P., and Choudhary, V. (2015). *Materials and Design*, 88, 269-277.
4. Dragoman, M., Grenier, K., Dubuc, D. [et al.]. (2006). *Appl. Phys. Lett.*, 88, 153108.
5. Macutkevic, J., Banys, J., Kuznetsov, V. [et al.]. (2013). *Phys. Status Sol. A.*, 210, 2683-2688.

ACTUAL PROBLEMS OF RADIOPHYSICS

Proceedings of the VI International Conference "APR-2015"

6. Qin, F., and Brosseau, C. (2012). *J. Appl. Phys.*, *111*, 061301.
7. Kuzhir, P., Paddubskaya, A., Plyushch, A. [et al.]. (2013). *J. Appl. Phys.*, *114*, 164304.
8. Kotsilkova, R., Ivanov, E., Bychanok, D. [et al.]. (2014). *Composites Science and Technology*, *106*, 85-92.
9. Kranauskaite, J., Macutkevicius, P., Kuzhir A. [et al.]. (2014). *Phys. Status Solidi A*, *211*(7), 1623-1633.
10. Maksimov, R. D., Bitenieks, J., Plume, E. [et al.]. (2010). *Mechanics of composite materials*, *46*, 345.
11. Merijs-Meri, R., Zicans, J., Ivanova, T. [et al.]. (2015). *Polymer composite*, *36* (11), 1048-1054.
12. Tessonier, J.-P., Rosenthal, D., Hansen, T. W. [et al.]. (2009). *Carbon*, *47*(7), 1779-1798.
13. Ham, H. T., Choi, Y. S., Jeong, N. [et al.]. (2005). *Polymer*, *46*(17), 6308-6315.
14. Strano, M. S., Dyke, C. A., Usrey, M. L. [et al.]. (2003). *Science*, *301*(5639).
15. Chen, L. F., Ong, C. K., Neo, C. P., Varadan, V. V., and Varadan, V. K. (2004). *Microwave Electronics: Measurement and material at microwave frequencies*, UK: John Wiley & Sons.
16. Almond, D., Duncan, G., and West, A. (1983). *Solid State Ionics*, *8*(2), 159-164.

INVESTIGATION OF Si/Ge p-i-n STRUCTURES WITH Ge QUANTUM DOTS BY ADMITTANCE SPECTROSCOPY METHODS

**A.A. Pishchagin¹, K.A. Lozovoy¹, V.Yu. Serokhvostov¹, A.P. Kokhanenko¹,
A.V. Voitsekhovskii¹, A.I. Nikiforov²**

¹*National Research Tomsk State University, Tomsk, Russia*

²*Rzanov Institute of Semiconductor Physics SB RAS, Novosibirsk, Russia*

Correspondence to:

A. A. Pishchagin
Post Address: Tomsk State University, 36 Lenin Ave., Tomsk, Russia, 634050
E-mail: apisch@gmail.com

Citation:

Pishchagin, A. A., Lozovoy, K. A., Serokhvostov, V. Yu., Kokhanenko, A. P., Voitsekhovskii, A. V., and Nikiforov, A. I. (2016). Investigation of Si/Ge p-i-n structures with Ge quantum dots by admittance spectroscopy methods. In *Actual problems of radiophysics. Proceedings of the VI International Conference "APR-2015"*, (pp. 45-48). London: Red Square Scientific.

Published: 14 October, 2016

Abstract. The experimental results on synthesis of Si/Ge p-i-n structures with Ge quantum dots in the *i*-region and their investigation by the method of admittance spectroscopy are presented. The activation energies of the emission process from localized states are calculated for two types of structures. Current-voltage characteristics without illumination and under illumination are measured.

Keywords: quantum dots, silicon, germanium, p-i-n structure, admittance spectroscopy.

Currently optoelectronics is experiencing rapid development, and the main objects of research are complex heterostructures with nanoscale inclusions. Creating semiconductor structures with new physical properties is the primary goal of nanotechnology, which has the aim of expanding the limits of applicability of semiconductor materials. In recent years the interest in photoelectric properties of Ge/Si heterostructures (primarily in the spectral range of 1.3–1.55 μm) has increased. New types of photodetectors based on silicon-germanium low-dimensional heterostructures using intrasubband and inter-subband transitions are intensively being developed. Such devices may be used in optoelectronic communication systems and remote monitoring [1, 2].

In this paper we present the experimental results on synthesis of Si/Ge

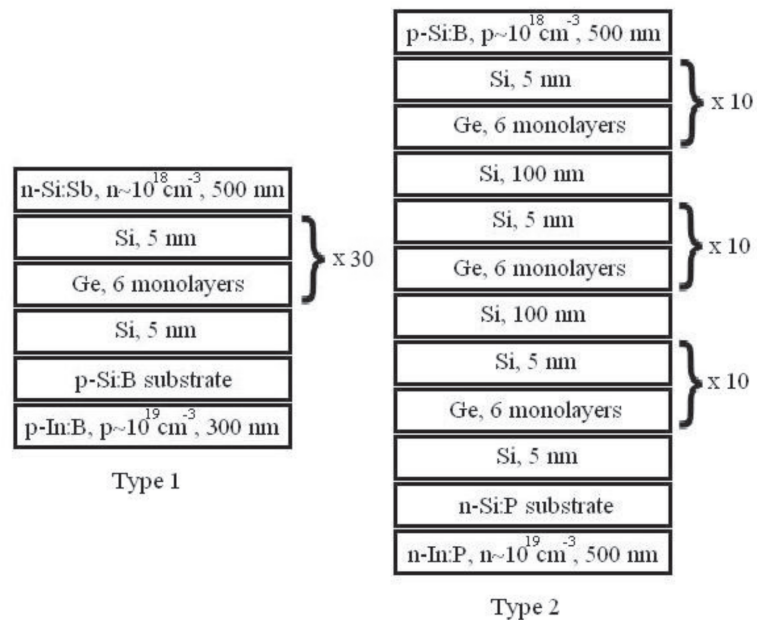


Fig 1. – Schematic representation of the structures studied.

This is an open access article of the Creative Commons Attribution-NonCommercial-NoDerivs License, which permits use and distribution in any medium, provided the original work is properly cited, the use is non commercial and no modifications or adaptations are made.

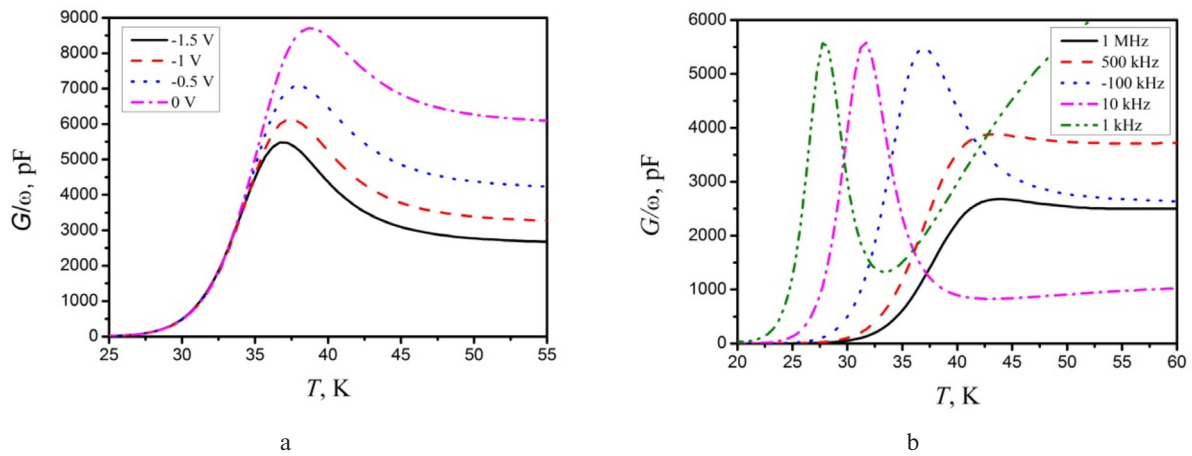


Fig. 2. – Temperature dependence of conductance for type 1 sample measured at various bias voltages at the test signal frequency of 100 kHz (a) and at various frequencies of the test signal and the applied bias voltage of -1.5 V (b).

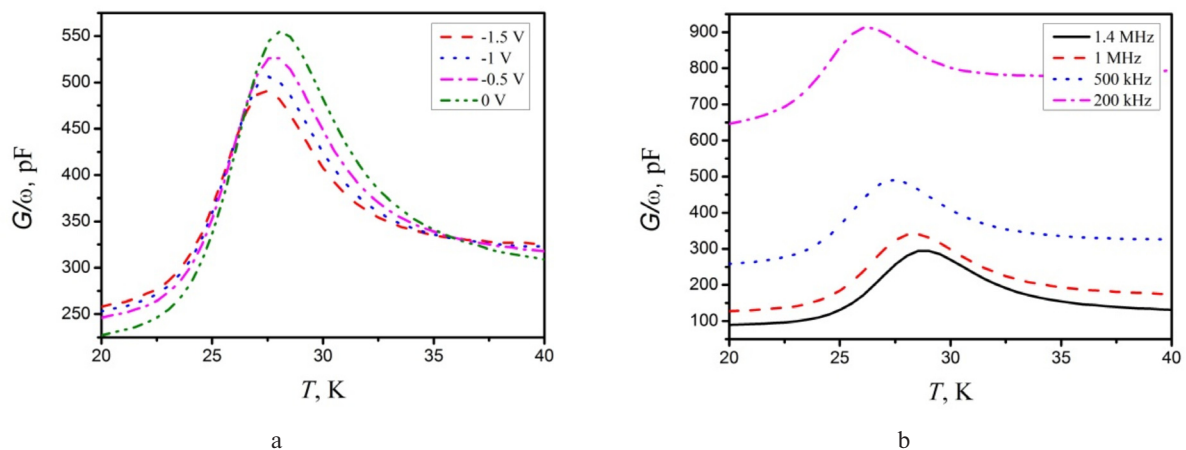


Fig. 3. – Temperature dependence of conductance for type 2 sample measured at various bias voltages at the test signal frequency of 100 kHz (a) and at various frequencies of the test signal and the applied bias voltage of -1.5 V (b).

p-i-n structures with Ge quantum dots in the *i*-region and their investigation by the method of admittance spectroscopy.

The samples were fabricated by molecular beam epitaxy in an ultra-high vacuum installation “Katun-C”. Evaporation of silicon and germanium was carried out by electron beam evaporators, the dopants (Sb and B) were evaporated from effusion cells. The analytical part of the epitaxy chamber consists of a quadrupole mass spectrometer, a quartz thickness meter, and reflection high energy electron diffractometer (RHEED). The growth of Ge quantum dots was carried out on Si(100) substrates with

misorientation less than 0.5° . Array of Ge hut-clusters with height 1.5–3 nm, lateral size 10–40 nm, and surface density $\sim 10^{11} \text{ cm}^{-2}$ was formed on Si surface.

The samples with quantum dots, studied in this paper, were fabricated in Institute of Semiconductor Physics. Multiple layers with Ge quantum dots separated by thin 5 nm silicon layers are included in the intrinsic region of the samples. The *i*-region of type 1 samples contained 30 layers of 6 monolayer Ge quantum dots separated by 5 nm silicon layers. The *i*-region of type 2 samples contained 30 layers of 6 monolayer Ge quantum dots separated by 5 nm silicon layers, and every 10 layers of Ge quantum dots were ad-

ditionally separated by 100 nm of Si (Figure 1).

Measurements were performed on an automated admittance spectroscopy installation [3]. The principle of admittance spectroscopy of structures with quantum dots is based on measuring the complex conductivity of the system that occurs when discrete energy levels recharge due to emission of charge carriers and their capture by localized states.

The temperature spectra of conductance (G - T) at different frequencies of the test signal and various bias voltages were measured for examined structures (Figures 2, 3). In the temperature dependence of conductance of type 1 samples a maximum was observed at low temperatures of 25–40 K. The observed maximum of conductance corresponds to a discrete energy level. The position of this peak is shifted on the temperature scale as the frequency of the applied signal changes (Figure 2, *b*). With fixed bias voltage V_b recharging of the level occurs. The charge carrier emission rate from this level decreases at lower temperatures, so with a decrease in the frequency of the test signal the condition of maximum conductance is achieved at lower temperatures. Conductance peak position for the sample remains constant with changes in the applied bias voltage (Figure 2, *a*).

Similar results were obtained in studies of type 2 sample. Figure 3 shows the temperature conductance spectra measured at different voltages and at different frequencies.

Processing temperature spectra leads to a typical family of Arrhenius plots for finding activation energies of the emission process. The GT/ω value has a maximum at $\omega = e_p$, where ω is the angular frequency of the test signal, e_p is the charge carrier emission rate from a discrete level. By plotting maxima T_{\max} in coordinates $\omega = f(1/T)$ the activation energy characterizing the position of the energy levels is determined. For each frequency a point with coordinates $\ln(e_p/T^2)$, $1/T_{\max}$ is plotted and the approximating straight line is built. From the slope of this line the activation energy is calculated. The observed maximum of conductance corresponds to a discrete energy level.

In a further study of type 2 sample a conductance peak at low positive bias was also detected (peak 2 in Figure 4). This maximum is observed only at positive bias at higher temperatures and is most pronounced at low frequencies, while the first maximum is also observed at negative bias.

For both samples activation energies were calculated. For the first peak of conductance calculated activation energies of type 1 and type 2 samples do not depend on the applied bias voltage and are equal to 38 ± 5 meV and 46 ± 4 meV respectively. For the sec-

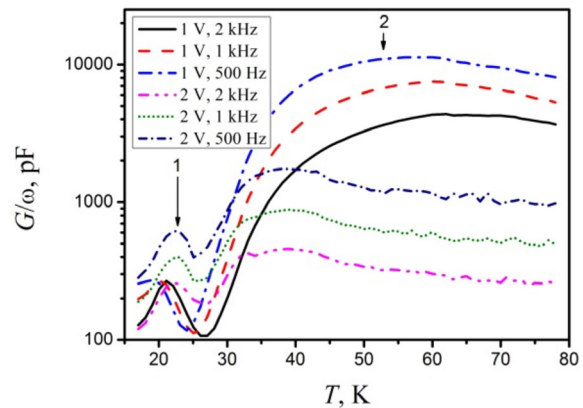


Fig. 4. – Temperature spectra of conductance of type 2 sample, measured at the voltages of +1 V and +2 V at different frequencies.

ond peak the calculated activation energy at a bias voltage of 1 V is 65 ± 10 meV, at a bias voltage of 2 V it is 165 ± 30 meV. This peak is broadened and probably corresponds not to a single discrete level but to a system of closely lying levels, due to the inhomogeneity of such parameters of quantum dots as their lateral size, height, shape and density in the array.

The first peak on the temperature dependence of conductance may be associated with the impurity level in Si. The second peak is explained by the presence of spatial quantization levels in the system associated with Ge quantum dots. Appearance and modification of peaks can be explained by the fact that with a change in the applied voltage the electrochemical potential occasionally crosses the discrete energy levels, producing oscillations in the charge density distribution. The reason for this is the thermionic emission of charge carriers from a discrete level. Discrete level gives partial charge density increment. This increment of charge leads to an increase in the external circuit current measured as a change in conductance of a sample.

Also, current-voltage characteristics without illumination and under illumination by incandescent lamp and halogen lamp were measured in the temperature range 10–300 K. Processing current-voltage characteristics revealed that energy conversion efficiency and fill-factor of structures increase with decreasing temperature and reach their maximum in the temperature range of 20–30 K. Maximum of short-circuit current is observed in the same temperature range and match the maximum of temperature spectra of conductance at low frequency.

ACTUAL PROBLEMS OF RADIOPHYSICS

Proceedings of the VI International Conference "APR-2015"

References

1. Shklyaev, A. A., and Ichikawa, M. (2008). Extremely dense arrays of germanium and silicon nanostructures. *Phys. Usp.*, 178 (2), 139-169, (In Rus.).
2. Yakimov, A. I. (2013). Ge/Si Heterostructures with Ge Quantum Dots for Mid-Infrared Photodetectors. *Optoelectron., Instrum. and Data Process.*, 49 (5), 467-475.
3. Zubkov, V. I. (2007). *Diagnostics of semiconductor nanoheterostructures by admittance spectroscopy methods*, Saint-Petersburg, Russia: Elmor, (In Rus.).

INVESTIGATION OF MICROWAVE ULTRAWIDEBAND CHAOTIC GENERATION IN ACTIVE DETERMINISTIC SELF-OSCILLATE SYSTEM EXCITED BY IMPATT DIODE

I.V. Semernik, A.V. Demyanenko

Southern Federal University, Taganrog, Russia

Correspondence to:

I. V. Semernik
Post Address: Southern Federal
University, 44, Nekrasovskiy
lane, Taganrog, Rostov region,
347922, Russia
E-mail: ivsemernik@sfnedu.ru

Citation:

Semernik, I. V., Demyanenko, A. V. (2016). Investigation of microwave ultrawideband chaotic generation in active deterministic self-oscillate system excited by IMPATT diode. In *Actual problems of radiophysics. Proceedings of the VI International Conference "APR-2015"*, (pp. 49-53). London: Red Square Scientific.

Published: 14 October, 2016

This is an open access article of the Creative Commons Attribution-NonCommercial-NoDerivs License, which permits use and distribution in any medium, provided the original work is properly cited, the use is non-commercial and no modifications or adaptations are made.

Abstract. In this article we investigate the possibility of ultrawideband chaotic generation in the active deterministic self-oscillate system that excited by IMPATT diode. Transition of the oscillator into the chaotic mode implemented by introducing of discontinuity into the oscillator's transmission line. It is showed that discontinuity introduced into the oscillator's transmission line creates the conditions to effective ultrawideband chaotic generation into the two frequency bands: 6.5–8 GHz and 12–14 GHz. Ways to control of main engineering characteristics of microwave chaos generator are also discussed.
Keywords: Microwave oscillator, IMPATT diode, chaotic oscillations, dynamical chaos.

Introduction

RF and microwave chaotic oscillations currently provoke high interest in various areas of science and technology. Some of the promising areas of microwave chaotic source application are communication systems with chaotic carrier, radar and positioning systems with increased range resolution.

In order to achieve high efficiency and performance of such systems high requirements to chaos generator are imposed. First of all, developers are interested in spectral and correlation properties of chaotic oscillations. In the frequency band below a few gigahertz a problems with such generator designing does not arise. There are many schemes with chaotic dynamics based on bipolar transistors and MOSFETs. Methods of control chaotic oscillation bandwidth and output power level of chaos generators are also presented. But at the higher frequencies obtaining of effective chaotic generation in circuits based on the transistors currently are not available. So investigations of chaotic generation in microwave systems based on the different active elements and methods of control microwave chaos generator properties are important.

Purpose of this article is experimental research of chaotic generation in X-band self-oscillate system based on IMPATT diode and designing of methods to control microwave chaotic oscillation properties.

Obtained results

As an experimental model is used microwave oscillator with well-known design. For transition of microwave oscillator into chaotic mode discontinuity (shorted stub) is introduced into output transmission line of oscillator. Shorted stub is realized on the basis of 23×10 mm rectangular waveguide and introduced into oscillator's output transmission line via symmetrical waveguide T-bend in H plane. For the analysis of generated signal power spectrum Agilent E4407B is used with 100 kHz intermediate-frequency pass band. To observe waveforms and histograms of chaotic oscillations is used high-resolution real-time oscilloscope MSOS804A. To eliminate the measuring equipment's influence to investigated oscillator's dynamics ferrite rectifier is introduced into output transmission line. To changing delay of signal reflected from discontinuity a phase shifter is introduced between the oscillator and shorted stub. Construction of the researching oscillator is presented on Figure 1, where

ACTUAL PROBLEMS OF RADIOPHYSICS

Proceedings of the VI International Conference "APR-2015"

the following designations are used: 1 – oscillator IMPATT diode, 2 – variable-capacitance diode (do not used in this work), 3 – pin for adjusting load matching, 4 – pin for adjusting of resonators coupling, 5–8 – pins for adjusting of IMPATT diode's

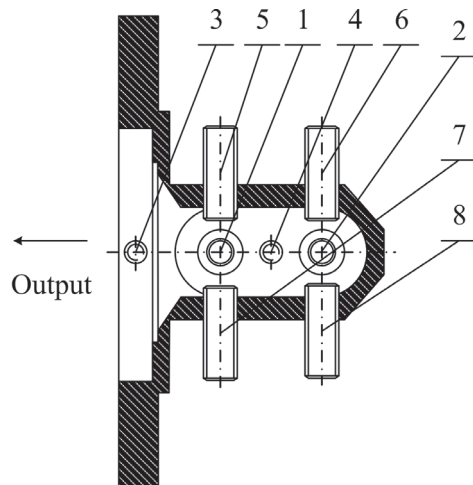


Fig. 1. – Construction of IMPATT oscillator.

and varactor's resonators. In this research 1A704B IMPATT diode is used that designed for using in 8.3–10 GHz frequency band, but also allowed the application in 6–8.3 GHz frequency band. Diode's operating current is below 50 mA and operating reverse voltage is below 60 V.

Oscillation occurs at a diode's supply current more 21 mA (Figure 2). At that generated signal is a harmonic oscillation with a frequency of 6.5 GHz and -57.6 dBm power. Growth of the diode's supply current results in oscillation's power spectrum enriching. When diode's supply current is equal 26 mA output signal of oscillator is a multi-frequency oscillation power spectrum of which contains a several individual harmonic components. Observations of generated signal's waveform shows that it has clear periodicity despite the oscillation has a complex form.

Increasing of the supply current up to 34 mA results in period doubling and growth of the noise "pedestal" near of each spectral component. A further increase of I_0 up to 35 mA leads to expansion of noise "pedestals" and merging them into unified noise spectrum located in the frequency range 6.5–7.5 GHz. It should be mentioned that at diode's supply current more than 34 mA the effect of intermittence of regular multi frequency oscillations and chaotic bursts is observed. This phenomenon is clear exhibited in spectral composition.

The phenomenon of intermittency is clearly observed by real-time oscilloscope with automatic sweep at a specified level of the leading front of the signal: at the increasing of supply current regular multi frequency oscillations is began to interrupt by the chaotic bursts and growth of I_0 leads to increasing of frequency and duration of these bursts.

Further increase of IMPATT diode's supply current leads to a transition of the system into chaotic mode. The investigated oscillator passes into chaotic mode abruptly that agrees with the numerical research

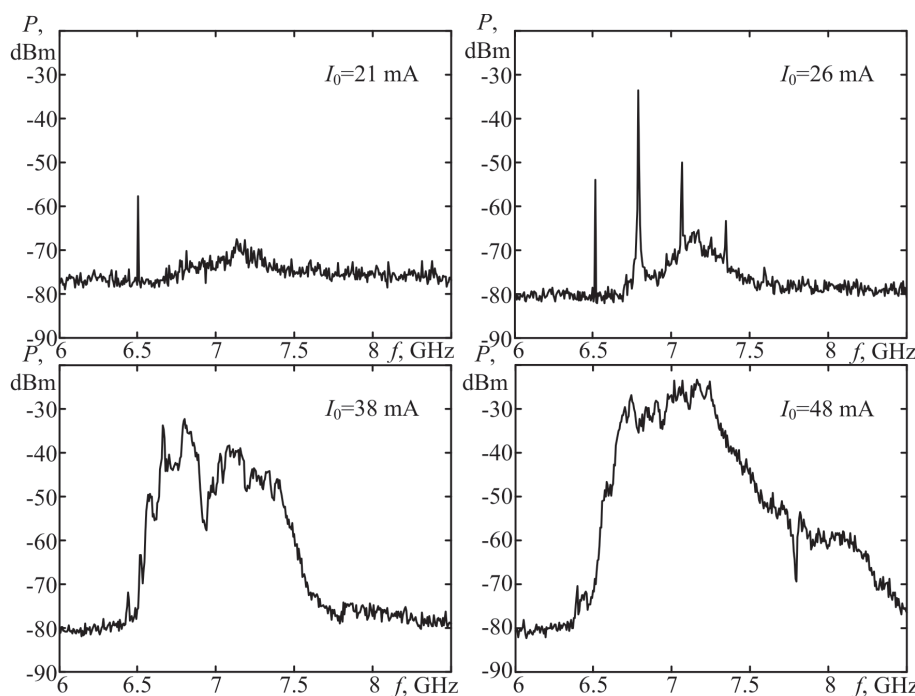


Fig. 2. – Spectral composition of generated signal at a several supply currents.

results. The oscillator transition into chaotic mode is clearly observed by spectral composition and the autocorrelation function of generated signal changing. Correlation window of the generated chaotic signal is about 8 ns.

Growth of the IMPATT diode supply current up to values closed to the maximum allowable operating current results in spectral component's amplitude increasing, reduction of the unevenness of the noise spectrum and chaotic signal bandwidth expansion. So at the IMPATT diode supply current $I_0 = 38$ mA chaotic signal bandwidth reaches the 950 MHz at the level of -60 dBm and 1210 MHz at the supply current of 46 mA.

The chaotic spectrum unevenness reduction results, as you would expect, in autocorrelation function side lobe level reduction and decreasing of the

generated chaotic signal correlation window. At the IMPATT diode supply current $I_0 = 46$ mA the correlation window is equal 7 ns.

The unevenness of the power spectrum that showed on the Figure 2 is sufficiently high but it is possible to achieve smoother chaotic spectrum envelope by changing the parameters of discontinuity in the oscillator's output transmission line (length of shorted stub L_{stub} and additional delay of reflected signal that introduced by the phase shifter).

So it is possible to tune chaotic signal bandwidth over a wide range by the shorted stub length changing (Figure 3). The chaotic signal bandwidth tuning range is less than 1 GHz up to 1.65 GHz. At the same time there is an optimal value of L_{stub} at which there is a smallest chaotic spectrum unevenness. It is possible to the oscillator's dynamical modes control by the reflected signal additional delay tuning by the phase shifter: stimulate the transition of generator into chaotic, multi frequency and oscillatory mode. Furthermore by tuning of phase shifter the generator can be

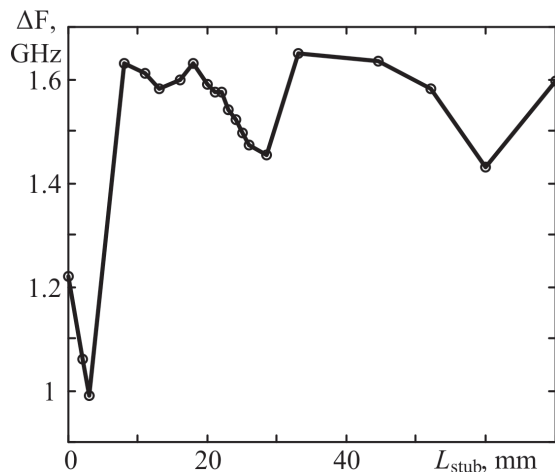


Fig. 3. – Dependence of the chaotic signal bandwidth on the shorted stub length.

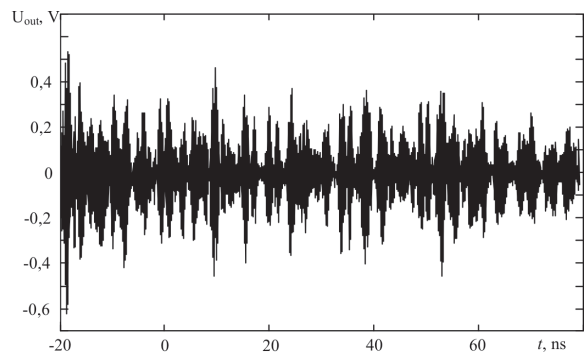


Fig. 5. – Oscillogram of the generated chaotic signal at the IMPATT diode supply current $I_0 = 46$ mA.

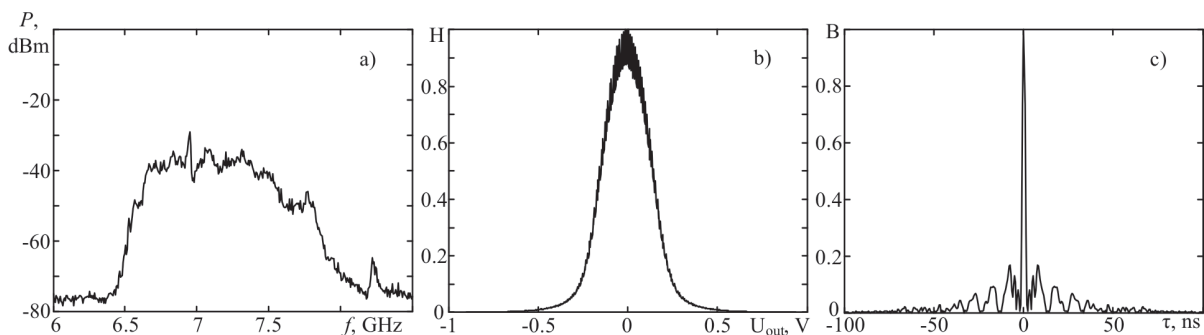


Fig. 4. – Power spectrum (a), histogram (b) and autocorrelation function (c) of the generated chaotic signal at the IMPATT diode supply current $I_0 = 46$ mA.

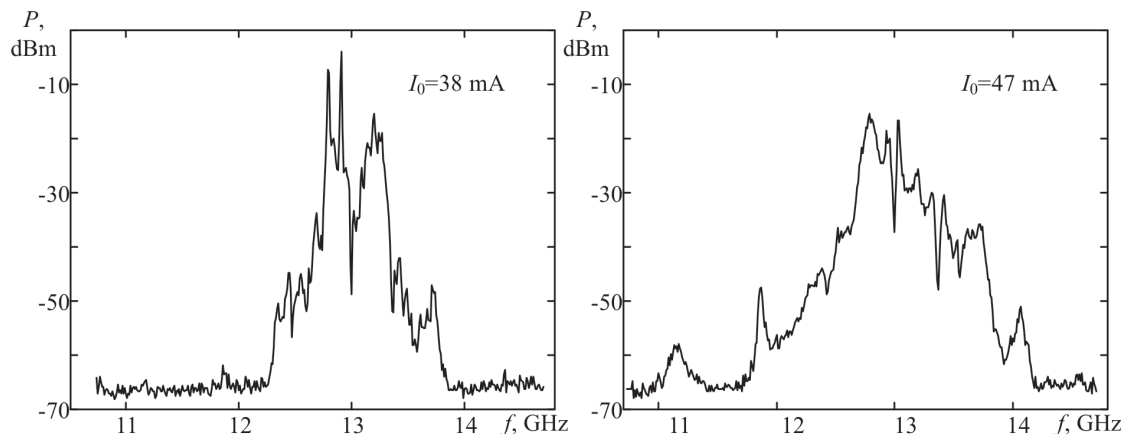


Fig. 6. – Spectral composition of generated signal near the second harmonic.

adjusted to the most efficient chaotic mode that characterized by the smoothest chaotic spectrum envelope (Figure 4a), the statistical properties of the signal closed to quasi-white noise (Figure 4b) and small correlation window equal to 1.2 ns (Figure 4c). The oscillogram of this signal showed on the Figure 5.

It should be mentioned that chaotic dynamics is also observed in the vicinity of second harmonic in the frequency range 12–14 GHz. The chaotic signal power spectrum in this frequency range showed on the Figure 6. But it has a much more unevenness and does not lend itself such flexible adjustment as a chaotic spectrum in the vicinity of the fundamental harmonic. It should be assumed that it is due to large unevenness of frequency dependence of the reflection coefficient from the shorted stub at a high frequencies. Furthermore through adjustment of generator coupling with a load it is possible to configure the microwave generator to the mode that is characterized by a chaotic generation only in the frequency range near a fundamental harmonic whereas the generation is completely absent at a higher frequencies. At the same time the effect of redistribution of generated power is observed: generation is completely suppressed in the frequency range 12–14 GHz but in the vicinity of main harmonic (6.5–8 GHz) amplitudes of the spectral components are sufficiently increased.

Conclusion

So it is showed that discontinuity introduced into the microwave IMPATT oscillator's transmission line creates the conditions to effective ultrawideband chaotic generation into the two frequency ranges: 6.5–8

GHz and 12–14 GHz. It is possible to redistribute of generated power between the frequency bands by tuning of the generator coupling with load: partially or completely reduce the chaotic spectrum components amplitude into a high frequency range and increase the chaotic signal power into the 6.5–8 GHz frequency range. Chaotic signal bandwidth it is possible to control by tuning the IMPATT diode supply current or shorted stub length. The second way is more acceptable because the change of supply current has a strong influence on the chaotic power spectrum envelope.

Acknowledgment

This work was performed as a project part of the state task No. 8.2461.2014/K of the Ministry of Education of Russia.

References

1. Dmitriev, A. (2012). *Chaotic generation*. Moscow, Russia: Technosfera.
2. Semernik, I. V., Alekseev, Yu. I., and Demyanenko, A. V. (2013). A research of a possibility of chaotic oscillation driving in an IMPATT diode oscillator by means of introduces a discontinuity to output transmission line. *Izv. visshih uchebnykh zavedenii. Fizika*, 56 (8/2), 337-339.
3. Alekseev, Yu. I., Demyanenko, A. V., Orda-Zhigulina, M. V., and Semernik, I. V. (2014). An experimental study of the development Dynamics of the chaotic oscillation mode in a deterministic self-oscillatory microwave system. *Instruments and experimental techniques*, 57(3), 307-310.
4. Alekseev, Yu. I., Demyanenko, A. V., and Semernik I. V. (2013). A study of the Gunn oscillator in determin-

- istic and chaotic modes. *Instruments and experimental techniques*, 56(6), 648-650.
5. Demyanenko, A. V., Alekseev, Yu. I., and Semernik, I. V. (2014). Effective Noise Generator Based on a Charge Accumulation Diode. *Russian Physics Journal*, 57(4), 554-557.
 6. Demyanenko, A. V., Semernik, I. V., and Orda-Zhigulina, M. V. (2015). Numerical study of dynamics of avalanche transit time microwave oscillator. In. *2015 International Siberian Conference on Control and Communications (SIBCON) Proceedings. Omsk State Technical University. Russia, Omsk, May, 21-23, 2015*, 1-6.
 7. Orda-Zhigulina, M. V., Demyanenko, A. V., Semernik, I. V., and Yukhanov, Yu. V. (2015). Investigation of chaotic mode of active determinate oscillating system which is excited by negative resistance of non-linear element. In. *2015 16th International Radar Symposium (IRS) Proceedings. Dresden, Germany. June, 24-26, 2015*, 789-793.

RESEARCH OF ELECTROMAGNETIC PROPERTIES OF FERROFLUID BASED ON SEMI-SYNTHETIC OIL IN THE TERAHERTZ FREQUENCY RANGE

V.I. Suslyayev, A.A. Pavlova, A.V. Badin

National Research Tomsk State University, Tomsk, Russia

Abstract. Today ferrofluids are applied in different devices: seals, dumpers, loudspeakers, stepper motors, etc. Magneto-optic phenomena in ferrofluids allow to use ferrofluids as polarizer. However, properties of ferrofluids depend on composition and frequency area. A technique for measuring the transmission coefficient and phase shift of the electromagnetic wave for ferrofluid in the terahertz range is presented.

Keywords: ferrofluids, terahertz, microwaves, semi-synthetic oil, electromagnetic properties.

Correspondence to:

A. A. Pavlova
Post Address: Tomsk State University, 36 Lenin Ave., Tomsk, Russia, 634050
E-mail:
sandy.surname@gmail.com

Citation:

Suslyayev, V. I., Pavlova, A. A., and Badin, A. V. (2016). Research of electromagnetic properties of ferrofluid based on semi-synthetic oil in the terahertz frequency range. In *Actual problems of radiophysics. Proceedings of the VI International Conference "APR-2015"*, (pp. 54-57). London: Red Square Scientific.

Published: 14 October, 2016

Introduction

Ferrofluid is a stable colloid suspension of magnetic nanoparticles (e.g. magnetite) in a liquid carrier, such as organic solvent or distilled water [1–3]. Their properties depend on characteristics components and presence of external magnetic field. Ferrofluid nanoparticles have superparamagnetic properties. In the absence of external magnetic field particles possess a random orientation and ferrofluid is anisotropic. But in the presence of external magnetic field particles align in its direction. After removing magnetic field the particles lose their magnetization and turn into initial state. The particles are placed one after another to form thin linear chains, distributed throughout the sample and oriented in the direction of the applied magnetic field.

Ferrofluids are found applications at different areas: brakes, buckles, hermetic seals, heat transfer systems, drug delivery systems, adaptive optics systems etc. [4–5]. Today new application of ferrofluids – elements of terahertz frequency range, e.g. tunable polarizers and attenuators – is developing active.

In this paper we explore electromagnetic properties of ferrofluids in the presence of external magnetic field in the frequency range 120–260 GHz. Two types of ferrofluids were investigated: with and without multiwalled carbon nanotubes.

Materials and methods

Ferrofluids were made based on semi-synthetic oil, magnetite particles and nanotubes. Parameters of magnetite particles are given in Table 1. Nanotubes with $d \approx 9.4$ nm were obtained by chemical vapor deposition in the presence of $\text{FeCo}/\text{Al}_2\text{O}_3$ catalyst.

Because particles of magnetite in our experiments were covered by amorphous carbon, we did not use any surfactant to prepare ferrofluid. Amorphous carbon prevents clumping of magnetite particles. Mixing of initial components was made by ultrasonic treatment that provides high isotropy of mixture.

Table 1. Properties of Fe_2O_4 nanoparticles

Size of particles, nm	90
Saturation magnetization, $\text{Gs}\cdot\text{sm}^3/\text{g}$	42,45
Residual magnetization, $\text{Gs}\cdot\text{sm}^3/\text{g}$	2,08

This is an open access article of the Creative Commons Attribution-NonCommercial-NoDerivs License, which permits use and distribution in any medium, provided the original work is properly cited, the use is non-commercial and no modifications or adaptations are made.

One of demands to carrier liquids for measurement of ferrofluid in THz range is low permittivity. So semi-synthetic oil with $\epsilon = 2.2$ relative units is appropriate liquid.

There were two types of samples: semi-synthetic oil + nanoparticles of Fe_3O_4 (ratio 70 : 30) and semi-synthetic oil + nanoparticles of Fe_3O_4 + multiwalled carbon nanotubes (ratio 70 : 29.5 : 0.5).

Quasi-optical spectrometer STD-21 was used for research electrophysical properties of ferrofluid in the terahertz frequency range. It allows measuring the complex dielectric constant of the liquid in the fre-

quency range from 40 GHz to 1.4 THz. Measurement setup is a Mach-Zehnder interferometer adapted to study the spectrum of the complex permittivity of liquids (Figure 1).

Interferometer consists of two arms – working (arm I) and reference (arm II). Radiation comes out of the backward wave oscillator (BWO) in the form of a divergent beam and is collimated into a plane-parallel beam with a dielectric lens. Beam splitter (grid 1) produces two beams going into arm I and arm II and then interfere. Resultant intensity is focused onto the detector with the second lens. The polarization

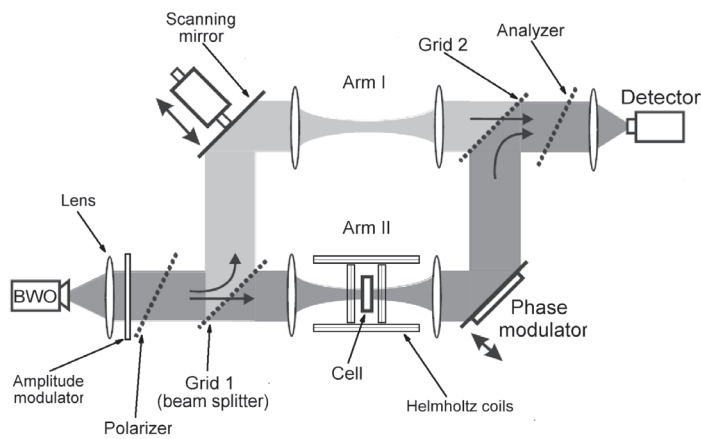


Fig. 1. – Scheme of terahertz spectrometer to research the influence of external magnetic fields on electrophysical properties of ferromagnetic fluids.



Fig. 2. – Measurement cell for research of ferromagnetic fluids in quasi-optical beams.

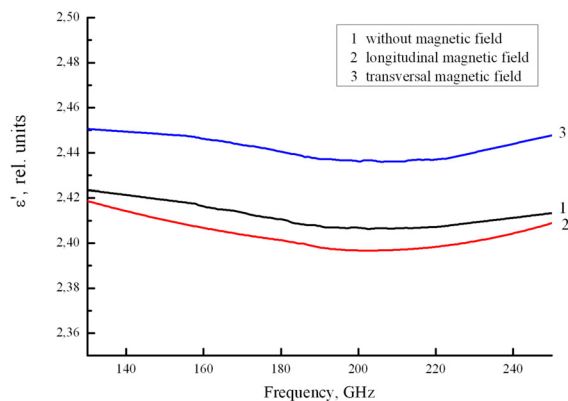


Fig. 3. – Influence of magnetic field on real part of ferrofluid permittivity spectrum.

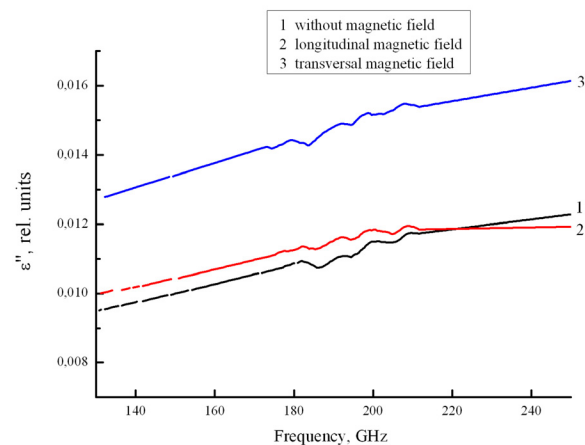


Fig. 4. – Influence of magnetic field on ferrofluid permittivity spectra.

of the beam incident on the cell is horizontal. Two lenses in the arm I are used to focus radiation on the cell. Two similar lenses in the reference arm II are compensating corresponding change in optical path. Scanning mirror (with an electronically driven stepper motor) is changing optical path in arm II. Phase modulator is involved in electronic tracing system. Absolute value of phase shift is calculated on basis of two positions of scanning mirror (one with and another – without cell in the measurement channel). This is done automatically (software-controlled) at every fixed frequency during spectra recording. Exposure to external magnetic fields (longitudinal and transverse) on cell with ferrofluid is carried by Helmholtz coils. At first electromagnetic response is measured without an external magnetic field. Then, changing current in the Helmholtz coils, applied longitudinal or transverse external field and measured electromagnetic response.

Shown in Figure 2 appearance of measurement cell for research of ferromagnetic fluids in quasioptical beams. Thickness of test liquid in cell is 9.92 mm. Windows in a cell are made from fluoroplastic (thickness of 50 microns). Using a fluoroplastic is caused by its resistance to external chemical exposure. The temperature of research ferrofluid was controlled by thermometer with thermocouple.

From equations (1) and (2) for transmission coefficient and phase-shift value of complex permittivity is calculated by software

$$T = E \frac{(1-r)^2 + 4r \sin^2 \beta}{(1-rE^2 + 4rE \sin^2(N+\beta))}. \quad (1)$$

$$\varphi = N + \operatorname{arctg} \frac{Er \sin(2(N+\beta))}{1 - Er \cos(2(N+\beta))} + \operatorname{arctg} \frac{b}{a^2 + b^2 + a} - \operatorname{arctg} \frac{b}{a+1}, \quad (2)$$

where: $E = e^{-\frac{4\pi kfd}{c}}$, $r = ((a-1)^2 + b^2) / ((a+1)^2 + b^2)$, $N = \frac{2\pi ndf}{c}$, $\beta = \operatorname{arctg} \left(\frac{2b}{a+b^2-1} \right)$,

$n + ik = \sqrt{\varepsilon' + i\varepsilon''}$; $a + ib = \sqrt{\mu^* / \varepsilon^*}$, c is the light velocity; d is the sample thickness; $\varepsilon^* = \varepsilon' + i\varepsilon''$ is the complex dielectric constant; $\mu^* = \mu' + i\mu''$ is the complex magnetic permeability.

Magnetic particles are line up in the chain. These particles oriented along polarization vector (trans-

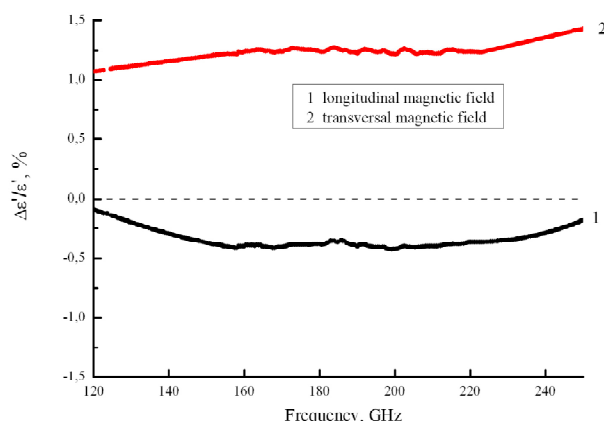


Fig. 5. – Relative change of real part of ferrofluid permittivity under magnetic field effect.

verse magnetic field) or along direction of wave propagation (longitudinal magnetic field). Obviously, in case of transverse magnetic field electromagnetic radiation more interacts with sample.

Experimental research of dependencies of transmission coefficient on magnetic field demonstrate that intensive changes are under increasing of magnetic field intensive from 0 to 30 Oe. Under magnetic field intensive about 100 Oe effect becomes stable. So, further investigation of permittivity carried out at 100 Oe. Experimental results of real and imaging parts of permittivity investigation are presented in Figures 3 and 4.

Obviously, orientation along polarization vector of electromagnetic wave leads to increase of real and imaging part of permittivity. Influence of magnetic field oriented along direction of electromagnetic wave propagation is much weaker. Relative change of real part of permittivity under magnetic field effect is presented in Figure 5.

Conclusion

In this paper we present the results of investigation of ferrofluid electromagnetic properties in terahertz frequency range. Transversal magnetic field provokes permittivity changing about 1.5 %. The most interesting issue for future work probably will be changing of ferrofluid composition, construction of measurement cell.

Acknowledgment

This Research is supported by Tomsk State University Competitiveness Improvement Program.

The authors would like to thank associate pro-

fessor Olga Alexandrovna Dotsenko who provided insight for result of our work. Also we would also like to show our gratitude to the associate professor Victor Alekseevich Zhuravlev for discussion conceiving of this work and for his tireless effort.

References

1. Fachini, F. F., and Bakuzis, A. F. (2010). Decreasing nanofluid droplet heating time with alternating magnetic fields. *Journal of Applied Physics*, 108, 084309-1-5.
2. Kefayati, G. H. R. (2014). Natural convection of ferrofluid in a linearly heated cavity utilizing LBM. *Journal of Molecular Liquids*, 191, 1-9.
3. Akbara, N. S., Razab, M., and Ellahi, R. (2015). Peristaltic flow with thermal conductivity of $H_2O + Cu$ nanofluid and entropy generation. *Results of Physics*, 5, 115-124.
4. Scherer, C., Scherer, C., Figueiredo Neto A. M. (2005). Ferrofluids: Properties and Applications. *Brazilian Journal of Physics*, 35 (3A), 718-727.
5. The ferrofluids story. (1993). Retrieved from: <http://ntrs.nasa.gov/search.jsp?R=20020080967>.
6. Bozhko, A. A., and Putin, G. F. (2004). Magnetic action on convection and heat transfer systems in ferrofluid. *Indian Journal of Engineering and Materials Sciences*, 11, 309-314.

METEOROLOGICAL COMPLEX BASED ON LIDAR AND RADAR

G.G. Shchukin, A.S. Boreysho, V.Yu. Zhukov, M.Yu. Ilyin, M.A. Konjaev

"Laser systems", Ltd, Saint-Petersburg, Russia

Abstract. Discuss question about design complex based on lidar and radar technology for detecting wake vortex and wind shear and also monitoring hazardous weather conditions. Evaluated the level of all-weather and technical capabilities of this complex.

Keywords: lidar, radar, wake vortex, wind shear, hazardous weather, all-weather complex.

Correspondence to:

M. Yu. Ilyin

Post Address: Laser Systems,
Ltd., 34A, Svyazi str., Strelna,
Saint-Petersburg 198515,
Russia.

E-mail: Ilyin_m@lsystems.ru

Citation:

Shchukin, G. G., Boreysho, A. S., Zhukov, V. Yu., Ilyin, M. Yu., and Konjaev, M. A. (2016). Meteorological complex based on lidar and radar. In *Actual problems of radiophysics. Proceedings of the VI International Conference "APR-2015"*, (pp. 58-61). London: Red Square Scientific.

Published: 14 October, 2016

One of the important goal of meteorological support the safety of aircraft is the detection of the vertical wind profile in the boundary layer of the atmosphere. Therefore, designing technical devices able to carry out similar measurements, paid much attention. Currently, created many such devices whose operation is based on different physical principles. By the way they may be divided into contact and remote principles measurement.

The first include the mast with gauges and radiosondes. And both of them have significant drawbacks and they are not good enough to be used their at airports for flight operational services. Masts have a height not taller than 150 meters, while the aviation needed data on the boundary layer to the height of 500 m. The weak point of radiosondes – low frequency update (2 times a day). Given that the wind field can change in a few minutes radically, such a low efficiency of obtaining wind data are not satisfied the service of airports and other potential users of such systems.

Therefore, leadership in this area belongs to the remote methods. These include: optical (lidar), radar and acoustic (sodar) system. The specifics of the airport is a big noise that making use of sodar is complicated. Moreover, sound waves intensively absorbed in the atmosphere, that influences on wind detection distance. As a result, remain lidar and radar.

Today we have a large number of such products. However, all of them have one drawback – the dependence efficiency on meteorological conditions. Lidar systems are used reflection from airborne particulate (molecules and the smallest aerosol) and are experiencing difficulties with the appearance of the smallest hydrometeor because of sharply increasing the attenuation of optical waves. Extreme value meteorological optical range (MOR) for these systems is considered to be the value of 3 km.

In radar systems, by contrast, the efficiency falls without hydrometeors because they are able to reflect enough power to be received by the radar. Thus, it becomes clear idea about complementarity of these two systems. Many airports have already implemented this idea – they set two systems, and switch one of them, depending on the existing weather conditions.

The transmit frequency can be different and are selected on the basis of specific goal. In particular, we are considering the case of detection of the wind profile in the atmospheric boundary layer thickness of 500 m and higher (up to 10 km). We adopt optimal wavelength of 8 mm [3]. Radio waves Ka-band is able to "see" the thin and middle optical thickness such as haze and fog. Figure 1 shows the dependence of the maximum detection distance of the optical (line 1) and radar (line 2 – the Ka-band, line 3 – X-band) systems depending on the radar reflectivity at the same power of the emitted pulse these systems. From this it follows that the lidar and Ka-band radar would be complementary.

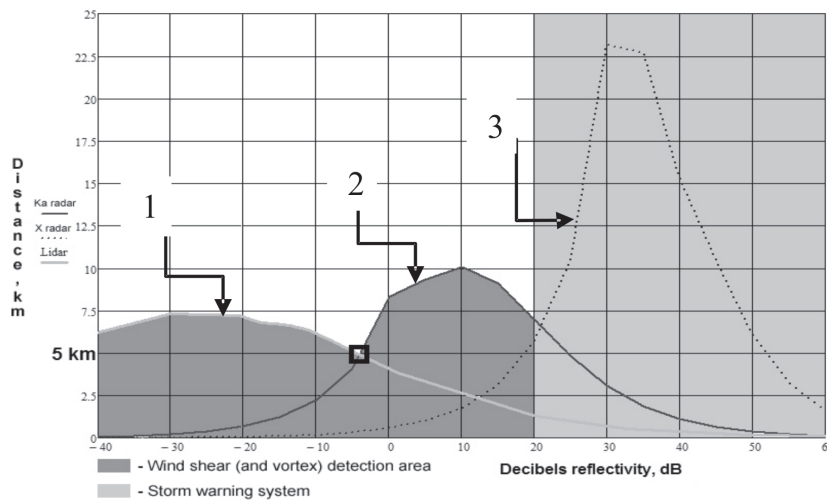


Fig. 1. – The dependence maximum detecting distance from the reflectivity values of argets for lidar (1) and Ka-band radar (2) and X-band (3).

Table 1. Specifications of the Doppler lidar WINDEX-5000

Characteristics	Value
Laser type	Fiber laser
Peak power, kW	0.5
Telescope diameter, mm	150
Zenith scan angle, °	0–180
Azimuth scan angle, °	0–360
Wavelength, nm	1560
Pulse width, μs	0.2–0.4
Min. measuring range, m	200
Max. measuring range, m	5000
Range resolution, m	75
Wind speed range measurement, m/s	1–55
Velocity resolution, m/s	0.5
Scan type	VAD, DBS, RHI, PPI, LOS
Power consumption, W	500
Weight, kg	150
Dimensions, mm*mm*mm	885*1005*1745

Table 2. Specifications of the Doppler radar 1B67-1

Characteristics	Value
Transmitter type	Klystron
Peak power, kW	5
Antenna type	Offset
Antenna diameter, mm	500*500
Zenith scan angle, °	45
Azimuth scan angle, °	0–360
Transmit frequency, GHz	35
Pulse width, μs	0.4
Min. measuring range, m	100
Max. measuring range, m	4000
Range resolution, m	30–70
Wind speed range measurement, m/s	0,3–50
Velocity resolution, m/s	0,5
Sensitivity, dBZ	–90
Power consumption, W	800
Weight, kg	14
Dimensions, mm*mm*mm	600*760*560

The next step in the development of wind profiler should be the design of all-weather complex by combining lidar and radar systems in a single device. In addition to the economic benefits due to their location on a single rotary support, achieved the unity of obtaining and processing data from both devices.

Wind profilers with a discussion of the wavelengths are sold on global market that confirms the

possibility of combining them into a single device. In Russia, the basis for the creation of new complex could be lidar WINDEX-5000 (“Laser systems”, Ltd., St. Petersburg) [4]. Main characteristics presented in Table 1.

The prototype of the radar system can be 1B67-1 Meteo complex, produced by Central Design Bureau Of Apparatus Engineering (“CDBAE” Tula) [5]. Characteristics are shown in Table 2.

ACTUAL PROBLEMS OF RADIOPHYSICS

Proceedings of the VI International Conference "APR-2015"

The direct use device 1B67 become impossible due to the values of some characteristics (weight, dimensions and diameter of the antenna), but it can be used as a prototype.

We define the parameters of the radar a block is able to provide the same characteristics as lidar in conditions of deterioration visibility.

The measuring distance will be determined based on the following considerations:

- it must be more than the “dead zone” of the antenna, which depends on the duration of the transmit pulse, recovery time, receiver sensitivity and Fresnel zone, in which the antenna pattern is formed. Experience shows that in the millimeter wave band can be met all these conditions at a distance of 1 km from the radar;
- vertical size of the permitted amount of this range should not exceed 30 meters – the distance at which the measured value of wind shear.

Accordingly at a distance of 1 km width of the antenna pattern must be 2 degrees.

The second condition must be carried out to the heights of 500m. Hence we determine the maximum duration of the impulse. At the maximum elevation angle of the antenna 30 degrees the condition must satisfy the inequality

$$\frac{c\tau}{4} \leq 30 \text{ m or } \tau \leq 0.4 \text{ s.}$$

Assuming beamwidth 2 degrees obtain the smallest possible diameter of the antenna

$$D = \frac{\lambda}{\theta} = 0,24m . \quad (1)$$

The minimum value of radar reflectivity, can be estimated by the value of this parameter at the meteorological complex 1B67, who has parameter equal – 90dBZ. The formula for calculating it is given

$$Z_{\min} = \frac{R_{\min}^2}{\Pi} \cdot \frac{P_r}{P_n}, \quad (2)$$

where is R_{\min} – the minimum range of the radar; Π – meteorological potential; $\frac{P_r}{P_n}$ – the minimum signal to noise ratio. Meteorological potential calculated by the formula [6]

$$\Pi = \frac{\pi^3 c \eta}{4^5 \lambda^2 \ln 2} \cdot \frac{P_t G^2 \theta^2 \tau}{P_n}, \quad (3)$$

where is P_t – peak power, G – antenna gain, θ –

beamwidth antenna, τ – pulse width, c – light speed, η – SWR radar.

All parameters design block and complex 1B67 are identical except the width of the antenna pattern (2 degrees instead of 1). As a result, we get the overall reduction in meteorological potential 6 dB.

Next, you need consider the extinction radio-wave on propagation path. At a distance of 1 km most of the factors that cause attenuation can be neglected. An exception is the rain that can make attenuation of 20 dB per km [6]. Consequently, the required minimum value of radar reflectivity will be – 44 dB.

Also radar should be able to perform the tasks overview surrounding area with the aim of short-range of weather forecast. It must be remembered that radar should has two modes – “reflectivity” and “speed”.

In the first aim of the radar – identify the hazards associated with clouds and precipitation. Consequently, there is no need to watch more “serious” target than nimbostratus cloud, for which. $Z_{\min} = 0$ dB. In the absence of interfering factors is the minimum viewing distance

$$R_{\min} = \sqrt{\frac{\Pi Z_{\min}}{(P_c/P_{III})_{\min}}} = 20\text{km} . \quad (4)$$

At this distance, we cannot neglect the extinction introduced by [6]:

- oxygen – 0.1 dB/km;
- water vapor – 0.01 dB/km;
- clouds. With an average water content of 1.75 and a temperature of 0° (maximum attenuation) is 1.75 dB / km;
- precipitation. Depending on intensity rain. The most interesting for us drizzling rain (0.22 dB/km) and rain (up to 20 dB/km).

If you limit the total attenuation of 20 dB we get a reduction of distance up to 2 km. To increase the capacity of the radar possible at the expense increasing the pulse width. An acceptable value for this parameter is 4 μ s, in which the minimum distance will be 10 km.

In the “speed” appears more difficult aim – detect hazards associated with the peculiarities of the spatial distribution of the wind. Therefore, in this case it is necessary to select extinction into layered cloud. Substituting into formula (2), this value and a pulse width of 4 microseconds we have $R_{\min} = 10$ km.

Thus, at the current stage there is a real possibility of design all-weather wind profiler for providing aviation safety on the basis of complexing lidar and radar.

References

1. Savin, A., Koniaev, M. (2008). *Meteospectum*, 1, 147-152.
2. Mazin, I., Shmeter, S. (1983). *Clouds: structure and physics of formation*, Leningrad: Gidrometeoizdat.
3. Kolomiets S., Gorelic, A., Shukin, G. (2012). *Proc. II All-Russian Armand Readings*, 30-36.
4. Arsenal. *Military-industrial Review* (2010). 5(23), 124-126.
5. Sterliadkin, V. [et. all.]. (2013). In. *Proc. III All-Russian Armand Readings*, 158-163.
6. *Guidelines for observation and usage of data delivered from non-automatic radars: MRL-1, MRL-2, MRL-5, RD 52.04.320-91. Guideline paper.* (1993). Saint-Petersburg: Gidrometeoizdat.

